

AD-775 915

BQM-34A POLARIZATION CHARACTERISTICS-  
RADAR CROSS SECTION AND GLINT

Robert W. Clay, et al

General Dynamics

Prepared for:

Army Missile Command

February 1974

DISTRIBUTED BY:

**NTIS**

**National Technical Information Service  
U. S. DEPARTMENT OF COMMERCE  
5285 Port Royal Road, Springfield Va. 22151**

Unclassified

Security Classification

AD 775915

DOCUMENT CONTROL DATA - R & D

(Security classification of title, body of abstract and indexing annotation must be entered when the overall report is classified)

1. ORIGINATING ACTIVITY (Corporate author) GENERAL DYNAMICS Convair Aerospace Division Fort Worth, Texas		2a. REPORT SECURITY CLASSIFICATION Unclassified	
		2b. GROUP	
3. REPORT TITLE BQM-34A Polarization Characteristics - Radar Cross Section and Glint			
4. DESCRIPTIVE NOTES (Type of report and inclusive dates) Final Report - 26 June 1973 to 31 January 1974			
5. AUTHOR(S) (First name, middle initial, last name) Robert W. Clay J. Kenneth Johnston			
6. REPORT DATE February 1974	7a. TOTAL NO. OF PAGES 120 136	7b. NO. OF REFS 12	
8a. CONTRACT OR GRANT NO. DAAH01-73-C-1102	9a. ORIGINATOR'S REPORT NUMBER(S) General Dynamics Report No. FZE-1312		
b. PROJECT NO.	9b. OTHER REPORT NO(S) (Any other numbers that may be assigned this report)		
c.			
d.			
10. DISTRIBUTION STATEMENT Reproduced by NATIONAL TECHNICAL INFORMATION SERVICE U S Department of Commerce Springfield VA 22151			
11. SUPPLEMENTARY NOTES		12. SPONSORING MILITARY ACTIVITY U.S. Army Missile Command Redstone Arsenal, Alabama 35809	

13. ABSTRACT

This program consisted of an investigation of the radar cross section and glint signature data of a BQM-34A target drone. The CP loss as measured by the difference in the median or mean RCS value obtained within a given angular sector was found to be highly variable for the case of small angular sectors and to be approximately 2 dB for the case of a large angular sector of 120 degrees centered about the nose of the vehicle.

Glint data were obtained by utilizing the discrete scatterer model developed by processing coherent short-pulse measurements data of the signature of a scale model BQM-34A. Additional glint data were obtained through use of the scattering matrix and RCS and phase measurements of an actual BQM-34A drone vehicle. Based upon the glint data, which were processed and analyzed, it was concluded that the statistics of the magnitude and frequency of the glint spikes are not significantly different for the case of linear and circular polarizations.

14

KEY WORDS

Radar Cross Section  
 Glint  
 BQM-34A Target Drone  
 CP Loss  
 Discrete Scatterer Model  
 Scattering Matrix

LINK A

LINK B

LINK C

ROLE

WT

ROLE

WT

ROLE

WT

General Dynamics Report No. FZE-1312  
BQM-34A Polarization Characteristics -  
Radar Cross Section and Glint

by

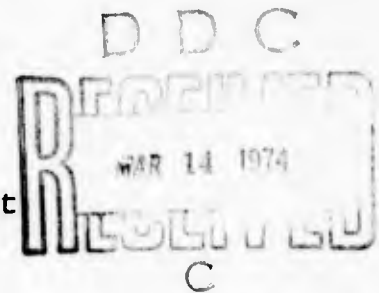
R. W. Clay  
J. K. Johnston

GENERAL DYNAMICS  
Convair Aerospace Division  
Fort Worth, Texas

Contract No. DAAH01-73-C-1102

Final Report  
26 June 1973 - 31 January 1974  
February 1974

Contract Monitor: Dr. James Wright



Prepared for  
U. S. Army Missile Command  
Redstone Arsenal, Alabama 35809

ic

## F O R E W O R D

This report is a documentation of an investigation of the polarization characteristics of a BQM-34A drone. Specific characteristics investigated included the mean and/or median radar cross section obtained within both small and large angular regions and the statistics of the magnitude and frequency of the linear glint spikes as characterized by the standard deviation of the glint obtained within small angular sectors. The primary intent of this program was to provide additional information concerning the polarization characteristics of complex radar targets for use in the selection and evaluation of an all-weather capability of an operational radar system.

This work was sponsored by the U. S. Army Missile Command, Redstone Arsenal, Alabama, under the direction of Dr. James W. Wright. The investigation was conducted by the Fort Worth Operation of the Convair Aerospace Division of General Dynamics Corporation under Contract Number DAAH01-73-C-1102.

The authors acknowledge with pleasure several suggestions of Mr. W. A. Pierson which were extremely helpful in conducting portions of the program. They also acknowledge Dr. James W. Wright for his assistance in meeting the objectives of this investigation.

# T A B L E O F C O N T E N T S

<u>SECTION</u>	<u>TITLE</u>	<u>PAGE</u>
1	INTRODUCTION	1
2	SUMMARY	3
3	COMPARISON OF SCALE MODEL MEASUREMENTS DATA	5
	3.1 Long-Pulse Measurements	5
	3.1.1 Measured RCS	7
	3.1.2 Median Values (Small Angular Sectors)	12
	3.1.3 Median Values (Large Angular Sectors)	12
	3.2 Discrete Scatterer Model	24
	3.2.1 Development of the Discrete Scatterer Model	25
	3.2.1.1 Short-Pulse Measurements	26
	3.2.1.2 Determination of Model Coefficients	29
	3.2.1.3 Computation of RCS and Glint	39
	3.2.2 Verification of the Discrete Scatterer Model	41
	3.2.3 Comparison of RCS and Glint	43
4	PROCESSING AND COMPARISON OF ACTUAL VEHICLE MEASUREMENTS DATA	53
	4.1 Computation of Circular Polarization Results	53
	4.2 Calculation of Glint from Measured Phase Data	55
	4.2.1 Direct Computation	55
	4.2.2 Data Processing (Filtering)	56
	4.2.3 Comparison with Measured Glint Data	61

T A B L E O F C O N T E N T S  
( C O N T I N U E D )

<u>SECTION</u>	<u>TITLE</u>	<u>PAGE</u>
4.3	Comparison of Linear and Circular Polarization Results	70
5	CONCLUSIONS AND RECOMMENDATIONS	79
6	REFERENCES	81
APPENDIX A	SCALE MODEL MEASUREMENTS DATA	83
	A.1 Measurements System Description	83
	A.2 Measurement Techniques	84
	A.3 Measurements Data	84

## LIST OF FIGURES

<u>FIGURE NO.</u>	<u>TITLE</u>	<u>PAGE</u>
3-1	Scale Model of the BQM-34A Drone	6
3.1-1	Target Orientation Conventions	8
3.1-2	RCS of Scale Model BQM-34A (V/V Polarization, 0° Pitch, 0° Roll)	9
3.1-3	RCS of Scale Model BQM-34A (R/L Polarization, 0° Pitch, 0° Roll)	10
3.1-4	RCS of Scale Model BQM-34A (L/L Polarization, 0° Pitch, 0° Roll)	11
3.1-5	Median RCS of Scale Model BQM-34A (R/L and V/V Polarizations, 0° Pitch, 0° Roll)	13
3.1-6	Median RCS of Scale Model BQM-34A (L/L and V/V Polarizations, 0° Pitch, 0° Roll)	14
3.1-7	Median RCS of Scale Model BQM-34A (R/L and V/V Polarizations, 0° Pitch, 20° Roll)	15
3.1-8	Median RCS of Scale Model BQM-34A (L/L and V/V Polarizations, 0° Pitch, 20° Roll)	16
3.1-9	Median RCS of Scale Model BQM-34A (R/L and V/V Polarizations, 0° Pitch, 45° Roll)	17
3.1-10	Median RCS of Scale Model BQM-34A (L/L and V/V Polarizations, 0° Pitch, 45° Roll)	18
3.1-11	Median RCS of Scale Model BQM-34A (R/L and V/V Polarizations, 20° Pitch, 0° Roll)	19

LIST OF FIGURES (Cont'd.)

<u>FIGURE NO.</u>	<u>TITLE</u>	<u>PAGE</u>
3.1-12	Median RCS of Scale Model BQM-34A (L/L and V/V Polarizations, 20° Pitch , 0° Roll)	20
3.1-13	Median RCS of Scale Model BQM-34A (R/L and V/V Polarizations, 45° Pitch, 0° Roll)	21
3.1-14	Median RCS of Scale Model BQM-34A (L/L and V/V Polarizations, 45° Pitch, 0° Roll)	22
3.2-1	Short-Pulse Radar System Block Diagram	28
3.2-2	Short-Pulse Measurement Geometry	30
3.2-3	Short-Pulse RCS of Scale Model BQM-34A (V/V Polarization, -30° Pitch, -90° Roll)	31
3.2-4	Short-Pulse RCS of Scale Model BQM-34A (H/H Polarization, -30° Pitch, -90° Roll)	32
3.2-5	Discrete Scatterer Target Geometry	34
3.2-6	Short-Pulse Response of Five-Sphere Target	36
3.2-7	Resolved Amplitude Function and Cross Range Response (Spheres 1 and 2)	37
3.2-8	Resolved Amplitude Function and Cross Range Response (Spheres 3, 4, and 5)	38
3.2-9	Target Response Computed from Measured Short-Pulse Data	42
3.2-10	Discrete Scatterer Model Verification (V/V Polarization, 0° Pitch, 0° Roll, -15° to 0°)	44

LIST OF FIGURES (Cont'd.)

<u>FIGURE NO.</u>	<u>TITLE</u>	<u>PAGE</u>
3.2-11	Discrete Scatterer Model Verification (V/V Polarization, 0° Pitch, -90° Roll, -10° to 10°)	45
3.2-12	Discrete Scatterer Model Verification (V/V Polarization, 20° Pitch, 0° Roll, -15° to 0°)	46
3.2-13	Discrete Scatterer Model Verification (V/V Polarization, 0° Pitch, -90° Roll, -30° to -10°)	47
3.2-14	RCS Computed from Discrete Scatterer Model (0° Pitch, 0° Roll, -15° to 0°)	48
3.2-15	Glint Computed from Discrete Scatterer Model (0° Pitch, 0° Roll, -15° to 0°)	49
3.2-16	RCS Computed from Discrete Scatterer Model (0° Pitch, 0° Roll, -75° to -45°)	50
3.2-17	Glint Computed from Discrete Scatterer Model (0° Pitch, 0° Roll, -75° to -45°)	51
4.2-1	Glint Determined From Phase Data (60° to 55°)	57
4.2-2	Glint Determined from Phase Data (55° to 50°)	58
4.2-3	Glint Determined from Phase Data (45° to 40°)	59
4.2-4	Glint Computed from Filtered Phase (60° to 55°)	62
4.2-5	Glint Computed from Filtered Phase (55° to 50°)	63

LIST OF FIGURES (Cont'd.)

<u>FIGURE NO.</u>	<u>TITLE</u>	<u>PAGE</u>
4.2-6	Glint Computed from Filtered Phase (45° to 40°)	64
4.2-7	Measured Glint (60° to 55°)	66
4.2-8	Measured Glint (55° to 50°)	67
4.2-9	Measured Glint (45° to 40°)	68
4.3-1	RCS of BQM-34A Drone (55 to 50 Degrees)	71
4.3-2	Glint of BQM-34A Drone (55 to 50 Degrees)	72
4.3-3	Cumulative Distribution of BQM-34A RCS and Glint (55 to 50 Degrees)	73
4.3-4	RCS of BQM-34A Drone (35 to 30 Degrees)	74
4.3-5	Glint of BQM-34A Drone (35 to 30 Degrees)	75
A-1	Target Orientation Conventions	86
A-2	X-Band RCS of BQM-34A Drone Model (V/V Polarization, 0° Pitch, 0° Roll)	87
A-3	X-Band RCS of BQM-34A Drone Model (L/L Polarization, 0° Pitch, 0° Roll)	88
A-4	X-Band RCS of BQM-34A Drone Model (R/L Polarization, 0° Pitch, 0° Roll)	89
A-5	X-Band RCS of BQM-34A Drone Model (V/V Polarization, 0° Pitch, 0° Roll)	90
A-6	X-Band RCS of BQM-34A Drone Model (L/L Polarization, 0° Pitch, 20° Roll)	91
A-7	X-Band RCS of BQM-34A Drone Model (R/L Polarization, 0° Pitch, 20° Roll)	92

LIST OF FIGURES (Cont'd.)

<u>FIGURE NO.</u>	<u>TITLE</u>	<u>PAGE</u>
A-8	X-Band RCS of BQM-34A Drone Model (V/V Polarization, 0° Pitch, 45° Roll)	93
A-9	X-Band RCS of BQM-34A Drone Model (L/L Polarization, 0° Pitch, 45° Roll)	94
A-10	X-Band RCS of BQM-34A Drone Model (R/L Polarization, 0° Pitch, 45° Roll)	95
A-11	X-Band RCS of BQM-34A Drone Model (V/V Polarization, 0° Pitch, 90° Roll)	96
A-12	X-Band RCS of BQM-34A Drone Model (L/L Polarization, 0° Pitch, 90° Roll)	97
A-13	X-Band RCS of BQM-34A Drone Model (R/L Polarization, 0° Pitch, 90° Roll)	98
A-14	X-Band RCS of BQM-34A Drone Model (V/V Polarization, 20° Pitch, 0° Roll)	99
A-15	X-Band RCS of BQM-34A Drone Model (L/L Polarization, 20° Pitch, 0° Roll)	100
A-16	X-Band RCS of BQM-34A Drone Model (R/L Polarization, 20° Pitch, 0° Roll)	101
A-17	X-Band RCS of BQM-34A Drone Model (V/V Polarization, 20° Pitch, 0° Roll)	102
A-18	X-Band RCS of BQM-34A Drone Model (L/L Polarization, -20° Pitch, 0° Roll)	103
A-19	X-Band RCS of BQM-34A Drone Model (R/L Polarization, -20° Pitch, 0° Roll)	104
A-20	X-Band RCS of BQM-34A Drone Model (V/V Polarization, 45° Pitch, 0° Roll)	105
A-21	X-Band RCS of BQM-34A Drone Model (L/L Polarization, 45° Pitch, 0° Roll)	106

LIST OF FIGURES (Cont'd.)

<u>FIGURE NO.</u>	<u>TITLE</u>	<u>PAGE</u>
A-22	X-Band RCS of BQM-34A Drone Model (R/L Polarization, $45^{\circ}$ Pitch, $0^{\circ}$ Roll)	107
A-23	X-Band RCS of BQM-34A Drone Model (V/V Polarization, $-45^{\circ}$ Pitch, $0^{\circ}$ Roll)	108
A-24	X-Band RCS of BQM-34A Drone Model (L/L Polarization, $-45^{\circ}$ Pitch, $0^{\circ}$ Roll)	109
A-25	X-Band RCS of BQM-34A Drone Model (R/L Polarization, $-45^{\circ}$ Pitch, $0^{\circ}$ Roll)	110
A-26	X-Band RCS of BQM-34A Drone Model (V/V Polarization, $-15^{\circ}$ Pitch, $-90^{\circ}$ Roll)	111
A-27	X-Band RCS of BQM-34A Drone Model (L/L Polarization, $-15^{\circ}$ Pitch, $-90^{\circ}$ Roll)	112
A-28	X-Band RCS of BQM-34A Drone Model (R/L Polarization, $-15^{\circ}$ Pitch, $-90^{\circ}$ Roll)	113
A-29	X-Band RCS of BQM-34A Drone Model (V/V Polarization, $-30^{\circ}$ Pitch, $-90^{\circ}$ Roll)	114
A-30	X-Band RCS of BQM-34A Drone Model (L/L Polarization, $-30^{\circ}$ Pitch, $-90^{\circ}$ Roll)	115
A-31	X-Band RCS of BQM-34A Drone Model (R/L Polarization, $-30^{\circ}$ Pitch, $-90^{\circ}$ Roll)	116
A-32	X-Band RCS of BQM-34A Drone Model (V/V Polarization, $-45^{\circ}$ Pitch, $-90^{\circ}$ Roll)	117
A-33	X-Band RCS of BQM-34A Drone Model (L/L Polarization, $-45^{\circ}$ Pitch, $-90^{\circ}$ Roll)	118

LIST OF FIGURES (Cont'd.)

<u>FIGURE NO.</u>	<u>TITLE</u>	<u>PAGE</u>
A-34	X-Band RCS of BQM-34A Drone Model (R/L Polarization, -45° Pitch, -90° Roll)	119

## LIST OF TABLES

<u>TABLE NO.</u>	<u>TITLE</u>	<u>PAGE</u>
3.1-1	Median Values of Scale Model RCS	23
4.2-1	Comparison of Moments of Measured and Computed Glint Data	69
4.3-1	Mean Value of Selected Cross Section Data	77
4.3-2	Standard Deviation of Selected Glint Data	78
A-1	Long Pulse Measurement Matrix (V/V, L/L, R/L Polarizations)	85

## S E C T I O N 1

### I N T R O D U C T I O N

This report contains a documentation of a study and investigation which was directed toward an analysis of radar signature measurements data in order to determine the polarization dependence of radar scattering characteristics of a complex aircraft target. These scattering characteristics include the median value of the radar cross section, a parameter utilized in estimating the detection range of a search radar, and linear glint, a parameter utilized in estimating the performance of a tracking radar. Specific attention was devoted to a comparison of these parameters for the case of circular polarizations in order to determine the decrease in detection range and significant reduction in target glint, if any, obtained with the use of circular polarization.

The use of circularly polarized radiation provides a means of reducing the competing clutter associated with rain. However, this technique of providing an all weather capability is often rejected on the basis of the reduction in target echo strength that is associated with the use of circular polarization. Recent studies performed by Convair Aerospace have shown that the effective reduction in the aspect regions of interest is much smaller than the values normally utilized. One objective of this investigation was to analyze radar cross section measurements data of a BQM-34A target drone in order to determine the reduction in target echo strength due to the use of circular polarization.

For the case of a tracking radar system in which the range from the radar to the target is small, the most significant source of error is the linear glint. Among the several techniques which have been utilized in order to significantly reduce the effects of target induced tracking errors on a radar system are methods involving frequency or polarization diversity or averaging. Since a circular polarized target signature can be described as an average of the three principle linear polarizations, another objective of this investigation included a comparison of the circular polarization glint with the linear polarization glint.

Measurements data of a scale model BQM-34A were obtained at Convair Aerospace under a Discrete Scatterer Target Modeling Contract with the Raytheon Company, and measurements data

of an actual drone were provided by the project monitor. Long-pulse measurements data of the scale model were reduced to determine the circular polarization loss in radar cross section. Short-pulse measurements data were also processed to obtain a Discrete Scatterer Model of the target signature. This model was then utilized to compute the linear glint. The measurements data of the full-scale vehicle were utilized to compute the circular polarization signatures; the cross section and glint of these data were then compared to the linear polarization data.

## S E C T I O N 2

### S U M M A R Y

This document contains a description of the results obtained during an investigation of the polarization characteristics of a BQM-34A drone. The primary objectives of this study were to determine the radar cross section (RCS) and linear glint for the case of two circular polarizations and compare these to the values obtained for the case of linear polarizations. These data could then be utilized in an analysis of the effects of modifying an existing radar system to transmit and receive circular polarization in order to provide an all weather capability.

An extensive set of scale-model radar cross section measurements data of the BQM-34A is shown in Appendix A. Median RCS data plots obtained within 5-degree angular sectors are presented in Section 3 for selected measurements data. Such characteristics as the median RCS obtained within a 120-degree sector about nose-on incidence are obtained and utilized as a measure of the circular polarization (CP) loss for the case of a typical angular sector viewed by a search radar. The CP loss obtained for the BQM-34A varies with respect to the target orientation, but a typical CP loss of 2 dB is a more accurate estimate than the often quoted figure of 6 to 8 dB.

Fluctuations in the apparent angular position of a target (glint) can produce a significant degradation in the tracking ability of a precision angle tracking radar. These glint errors are a result of changes which occur in the phase front curvature of the target echo when individual sources of scattering interfere coherently. Target glint can be determined from a coherent (amplitude and phase) target signature by differentiating the phase with respect to aspect angle in order to obtain the slope of the phase front. Since long-pulse phase measurements were not obtained for the case of the scale model BQM-34A and both the amplitude and phase can be obtained from the Discrete Scatterer Model, this model was utilized in computing the glint from the scale model vehicle.

The Discrete Scatterer Model is based upon the theory that the scattering from a complex target is basically due to currents which have local maximums at discontinuities in

the target surface. These localized currents appear at surfaces such as the inlet lips, turbine vanes and blades, and exterior edges. The amplitude and phase variation with respect to aspect angle of these discontinuities have been accurately predicted analytically and verified experimentally for the case of simple target configurations; however, for the case of complex targets, the analytical determination of the behavior of these discrete scatterers is an extremely complex problem which has not been solved. Convair Aerospace has developed an experimental technique to isolate these localized sources of scattering (discrete scatterers) and to determine their amplitude and phase behavior as a function of azimuth angle. This technique, which involves the processing of coherent short-pulse measurements data, was utilized to obtain a scattering model of the BQM-34A. A brief description of the processing technique, form of the model, and model verification is presented in Section 3.2.

The measurements data of the actual BQM-34A were obtained for the three principal polarizations. Circular polarizations signatures were computed from the measured scattering matrix data and the linear glint was determined from the resulting signatures by differentiating the phase data. Due to the extremely small angular increment of the measurements data, a filtering technique was utilized to reduce the high frequency noise components in the phase data before the glint was determined from the difference between two adjacent phase samples. This technique was verified experimentally by comparing the glint obtained from the filtered phase data with the measured glint. Selected comparisons of the RCS and glint of the full-scale target are presented in Section 4.

SECTION 3  
COMPARISON OF SCALE  
MODEL MEASUREMENTS  
DATA

Both long pulse and short-pulse radar measurements were made under a contract to the Raytheon Company to provide and verify a Discrete Scatterer Model of the target scattering characteristics of a BQM-34A drone. A 0.55 scale model of a BQM-34A drone was constructed and an extensive set of linear polarization measurements data were obtained in order to develop and verify the Discrete Scatterer Model. Additional circular polarization measurements were made in order to provide information concerning the circular polarization loss.

The scaled-model BQM-34A was constructed of fiberglass and conductive surfaces were flame sprayed or painted with a conductive aluminum coating. Specific emphasis was placed upon an accurate and yet reasonable modeling of the engine structure, the engine inlet and exhaust areas, the area immediately following the nose radome, and all external structures such as the riser cover and launch attachment.

The cowl was made conductive in order to reduce multiple scattering effects although a conductive cowl is an optional feature of the actual drone vehicle. The engine inlet duct was modeled back to the engine, and the engine modeling included the three support struts and the compressor blades. A photograph of the scale model is shown in Figure 3-1.

The radar cross section of this model was subsequently measured using both a coherent short-pulse system and a long pulse measurement system. The long pulse RCS data were processed to determine median values using both small and large angular sectors. The short pulse data were utilized in developing a discrete scatterer model of the target scattering for use in the computation of the linear glint.

### 3.1 LONG PULSE MEASUREMENTS

The long pulse measurements data were obtained in the form of great circle cuts over the full 360-degree rotation about the vehicle. The long-pulse measurement system is a

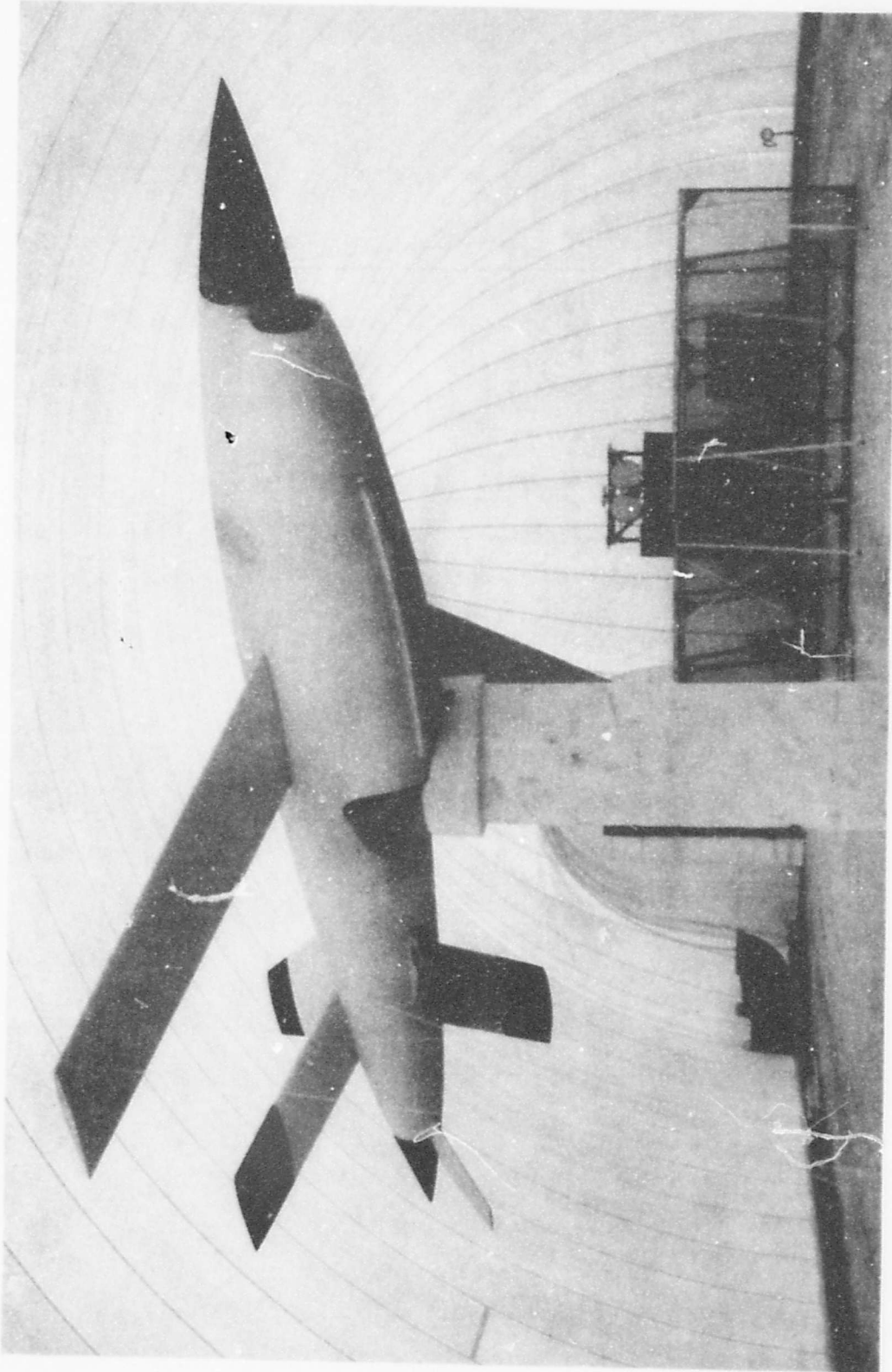


Fig. 3-1 SCALE MODEL OF THE BQM-34A DRONE

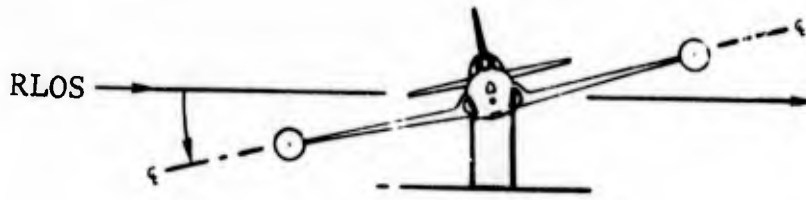
pulsed system which is range-gated at the range of interest. The target orientation conventions are shown in Figure 3.1-1. The measurements data are obtained in the form of analog plots and digital data which is recorded on paper tape and subsequently transferred to magnetic tape. The angular increment between data points is 0.1 degrees and the linear dynamic range is 50 dB.

### 3.1.1 Measured RCS

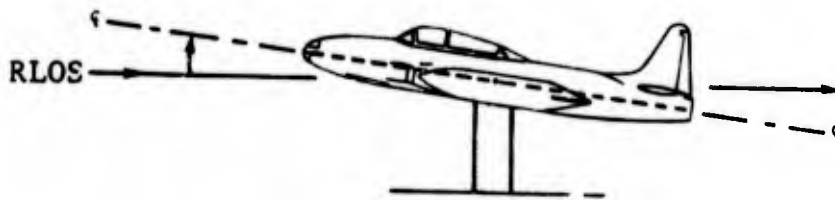
Selected plots of the analog data are presented in Figures 3.1-2 through 3.1-4. A large difference exists in the magnitude of the RCS at aspects near broadside ( $90^\circ$  and  $270^\circ$ ) for the case of the cross circular polarization (L/L) and similar sense circular (R/L) or vertical polarizations. At these aspects, the circular polarization (CP) loss, determined from the difference between the RCS in V/V polarization and L/L polarization, is 7 to 17 dB. However, it should be observed that the magnitude of the return in L/L polarization is large and exceeds the levels required for normal operation of a radar system. For the case of the wing speculars ( $+45^\circ$  azimuth), the CP loss relative to the vertical polarization return is approximately 2 dB.

At angles about nose-on incidence (0 degrees), the RCS in L/L polarization is larger than that in V/V polarization. This effect is probably due to multiple scattering phenomena in which energy is reflected from one surface or edge to another and then back to the radar. For the case of several types of scatterers including spheres, the phase difference between the vertically and horizontally polarized returns will be approximately 180 degrees. Thus, the L/L polarization return, which can be expressed in a form which includes terms, involving the difference between the vertical and horizontal polarization responses, is increased; while the R/L polarization return, involving the sum of these returns, is decreased.

A comparison of the three signatures presented in the Figures 3.1-2 through 3.1-4 indicates that the ratio of the magnitudes of the RCS is highly dependent upon the azimuth angle. In fact, at some azimuth angles, the CP loss computed as the ratio of the L/L RCS to the V/V RCS is actually a gain because the circular polarization RCS is larger than the V/V return.



POSITIVE ROLL ANGLE



POSITIVE PITCH ANGLE



POSITIVE ROTATION ANGLE

Fig. 3.1-1 TARGET ORIENTATION CONVENTIONS

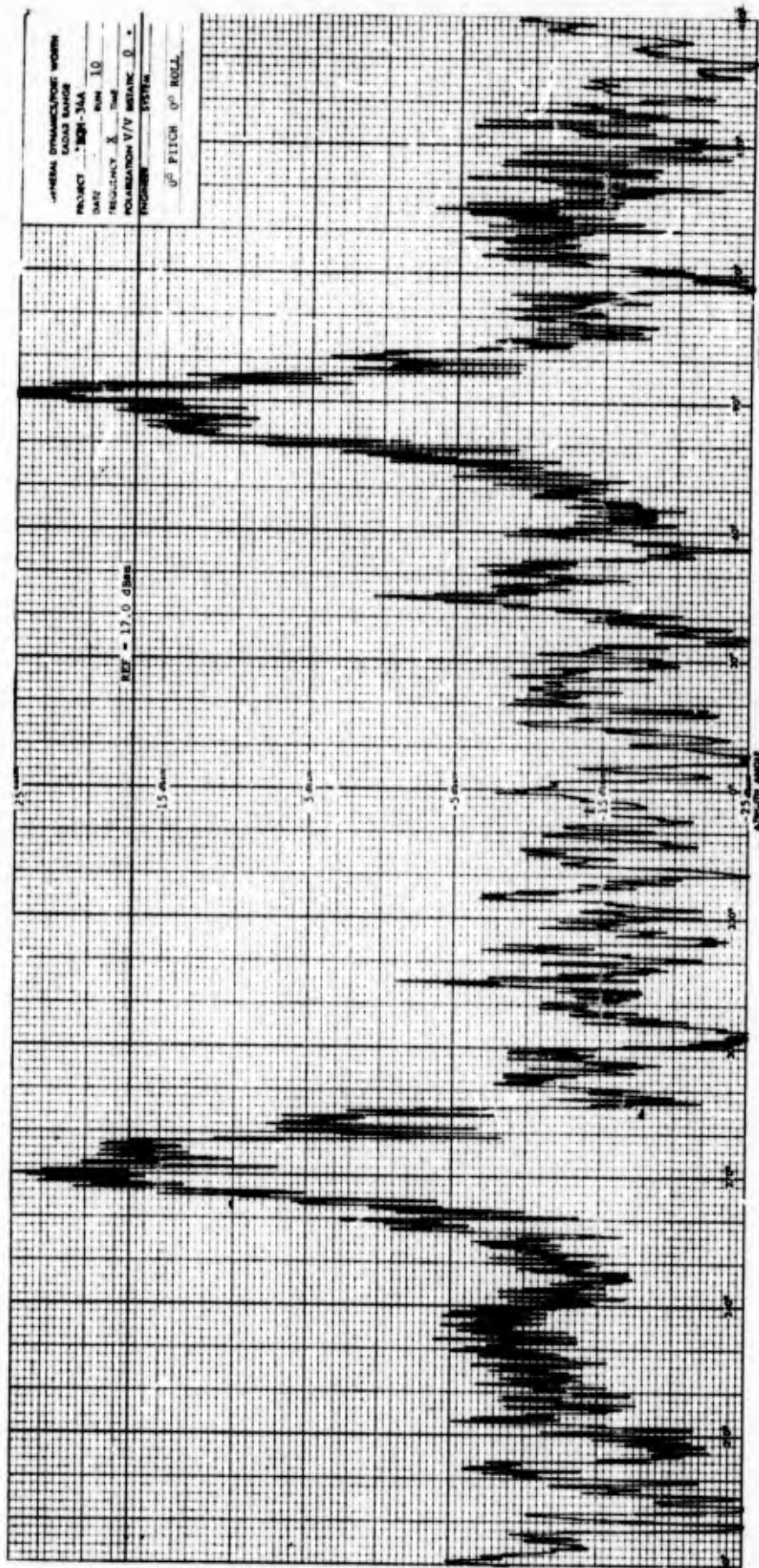


Fig. 3.1-2 RCS OF SCALE MODEL BQM-34A  
(V/V POLARIZATION, 0° PITCH, 0° ROLL)

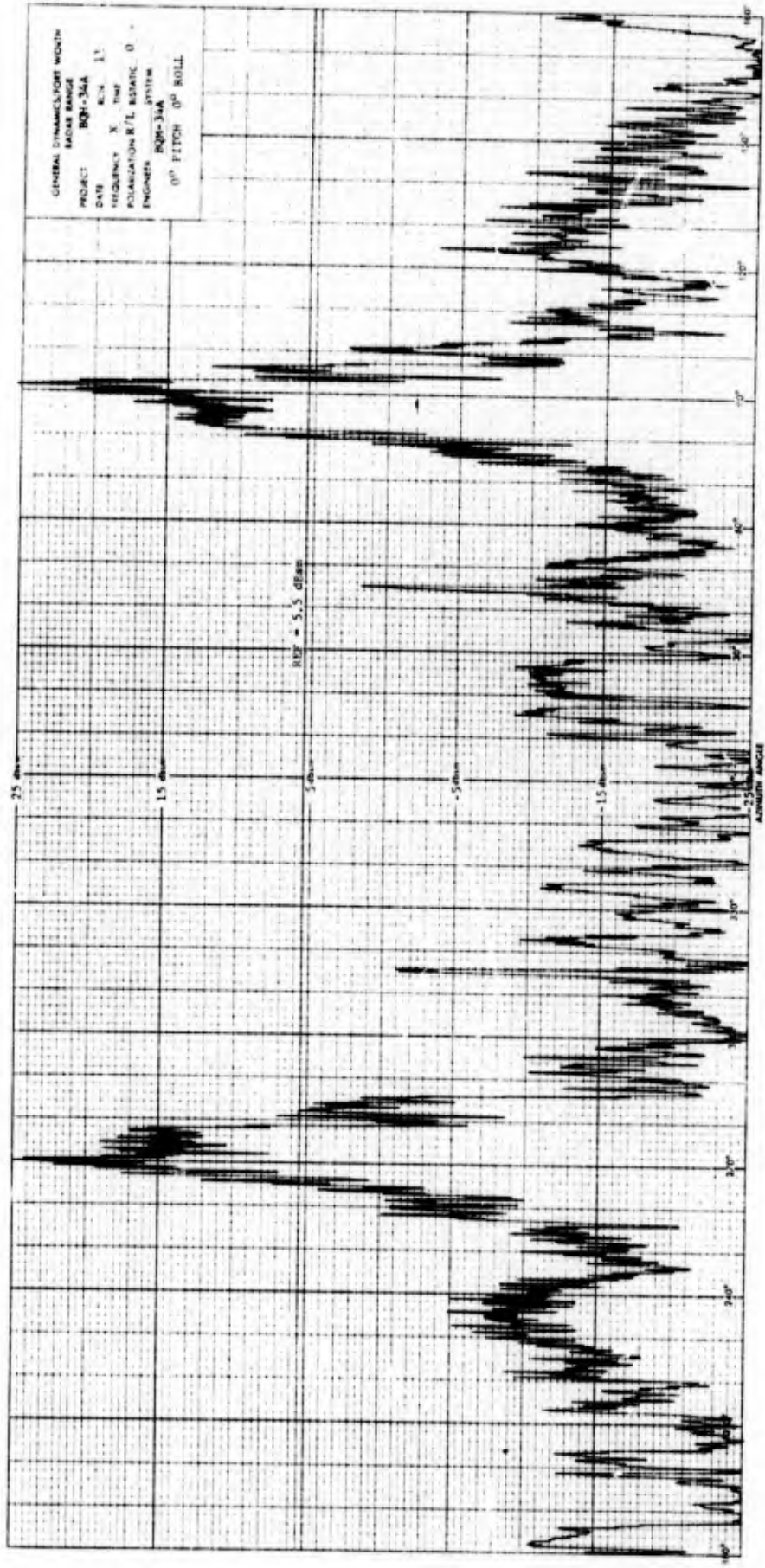


Fig. 3.1-3 RCS OF SCALE MODEL BQM-34A  
 (R/L POLARIZATION. 0° PITCH, 0° ROLL)

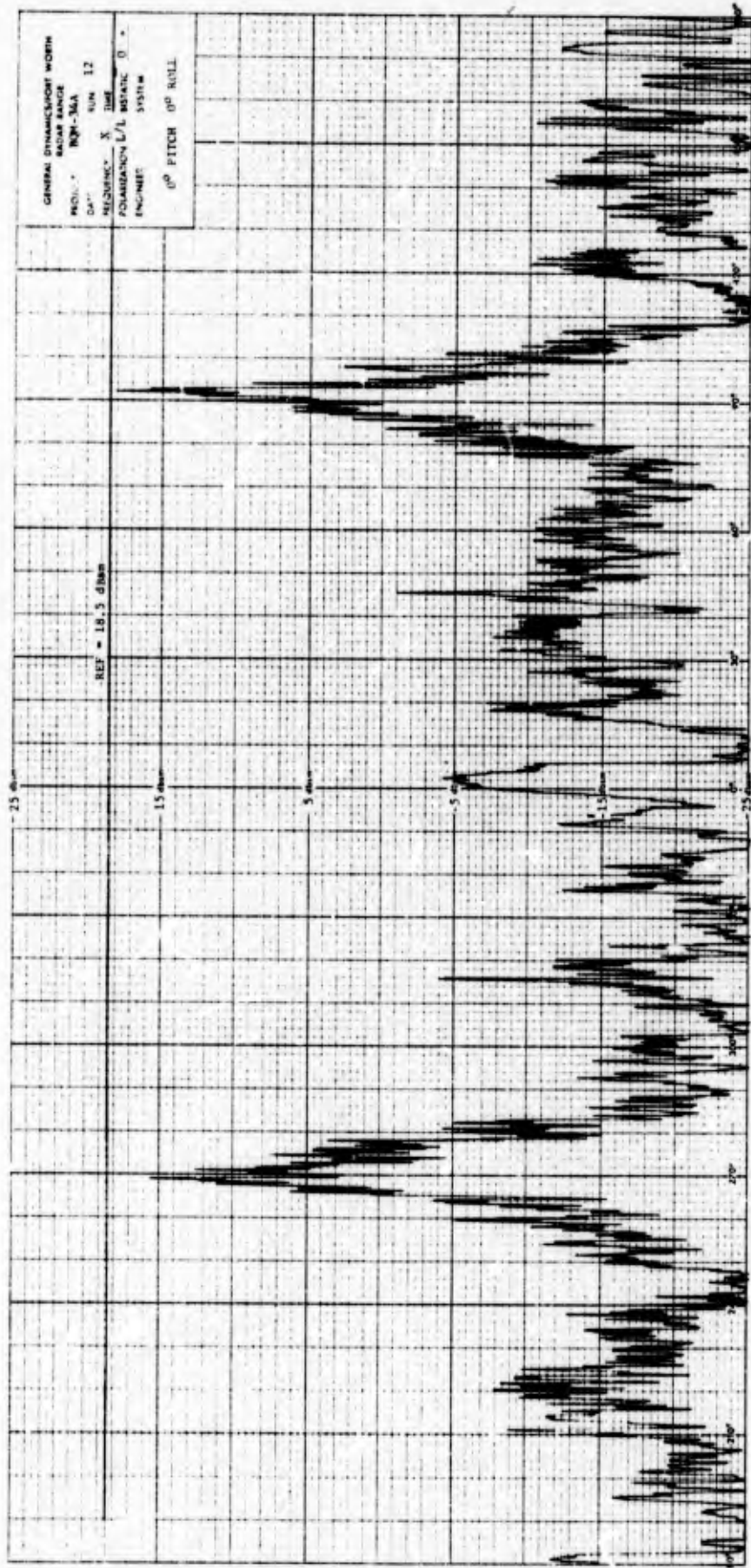


Fig. 3.1-4 RCS OF SCALE MODEL BQM-34A  
(L/L POLARIZATION, 0° PITCH, 0° ROLL)

### 3.1.2 Median Values (Small Angular Sectors)

The comparison of the linear and circular polarization signatures can be facilitated by comparing median values obtained over small angular sectors rather than by comparing the RCS data sampled at 0.1-degree increments. Median cross section values within 5-degree angular sectors were obtained at intervals of 2.5 degrees and were plotted through use of a CAL COMP plotter. The medians obtained within these small sectors retain the basic structure of the measurements data, but can be used to obtain a more overall comparison of the data than is possible using a direct point-to-point comparison of the measurements data. Selected median results are shown in Figures 3.1-5 through 3.1-14.

The median RCS is generally higher for the case of V/V polarization than L/L polarization. However, for most measurement configurations, there are isolated angular sectors in which the L/L polarization median is larger than the linear polarization median.

For the case of the measurement configuration of 0-degree pitch, 0-degree roll, the L/L median is larger than the V/V median at an azimuth of zero degrees and in the region from 30 to 40 degrees. The largest difference in the median values occurs at the broadside aspects where the V/V median is approximately 12 dB larger than the L/L median.

### 3.1.3 Median Values (Large Angular Sectors)

In order to obtain an overall comparison of the relative RCS for the case of circular and linear polarization, the digital long pulse measurements data were processed to obtain wide angle medians corresponding to azimuthal sectors of 120 degrees centered at 0 degrees (nose-on incidence). These data include the five pitch and four roll configurations and are presented in Table 3.1-1.

A comparison of the RCS data obtained for the case of the five pitch configurations indicates that the L/L polarization RCS is generally 2 dB lower than the V/V polarization RCS. This value of CP loss is significantly lower than the published values of 6 to 8 dB.

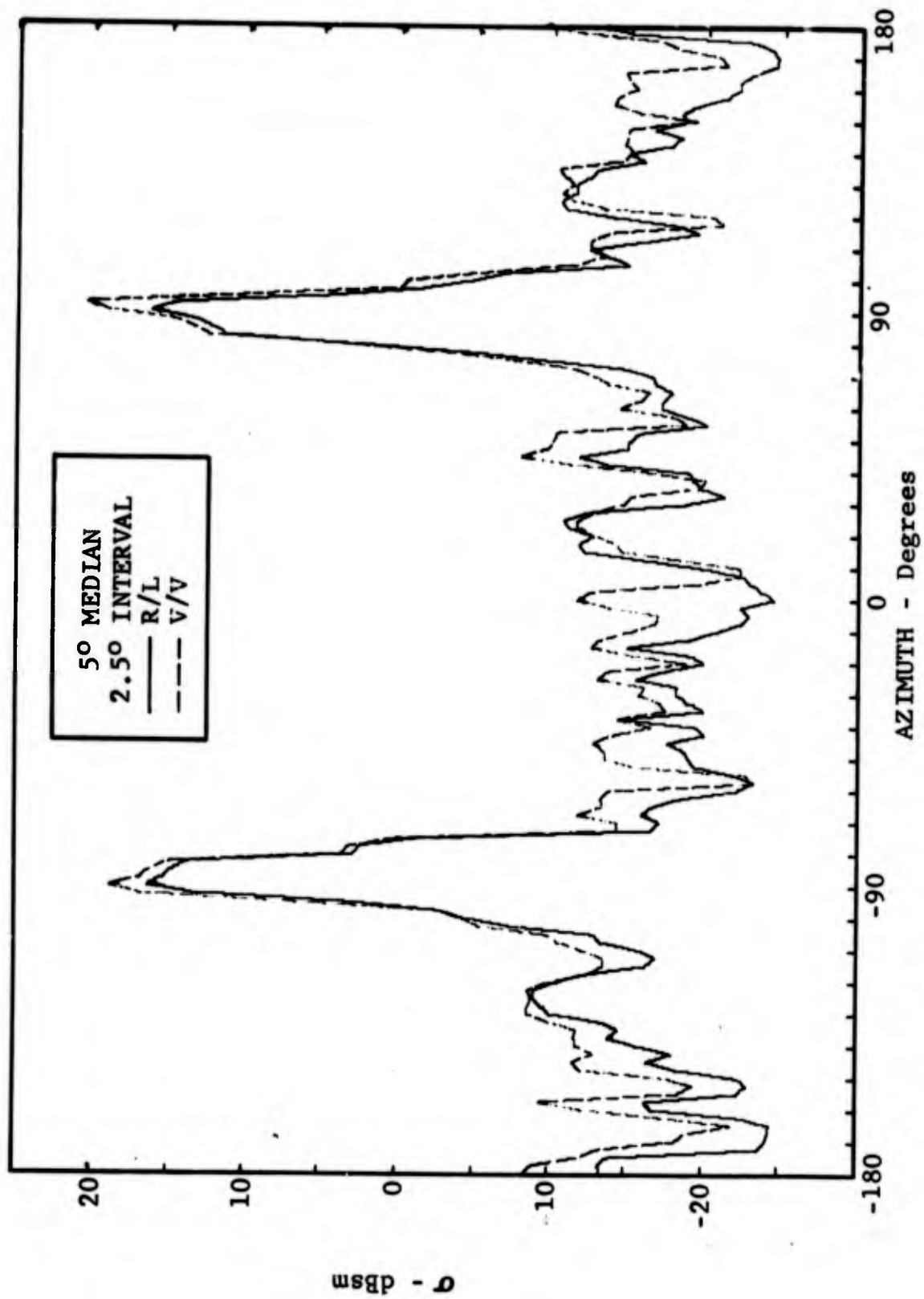


Fig. 3.1-5 MEDIAN RCS OF SCALE MODEL EQM-34A  
(R/L & V/V POLARIZATION, 0° PITCH, 0° ROLL)

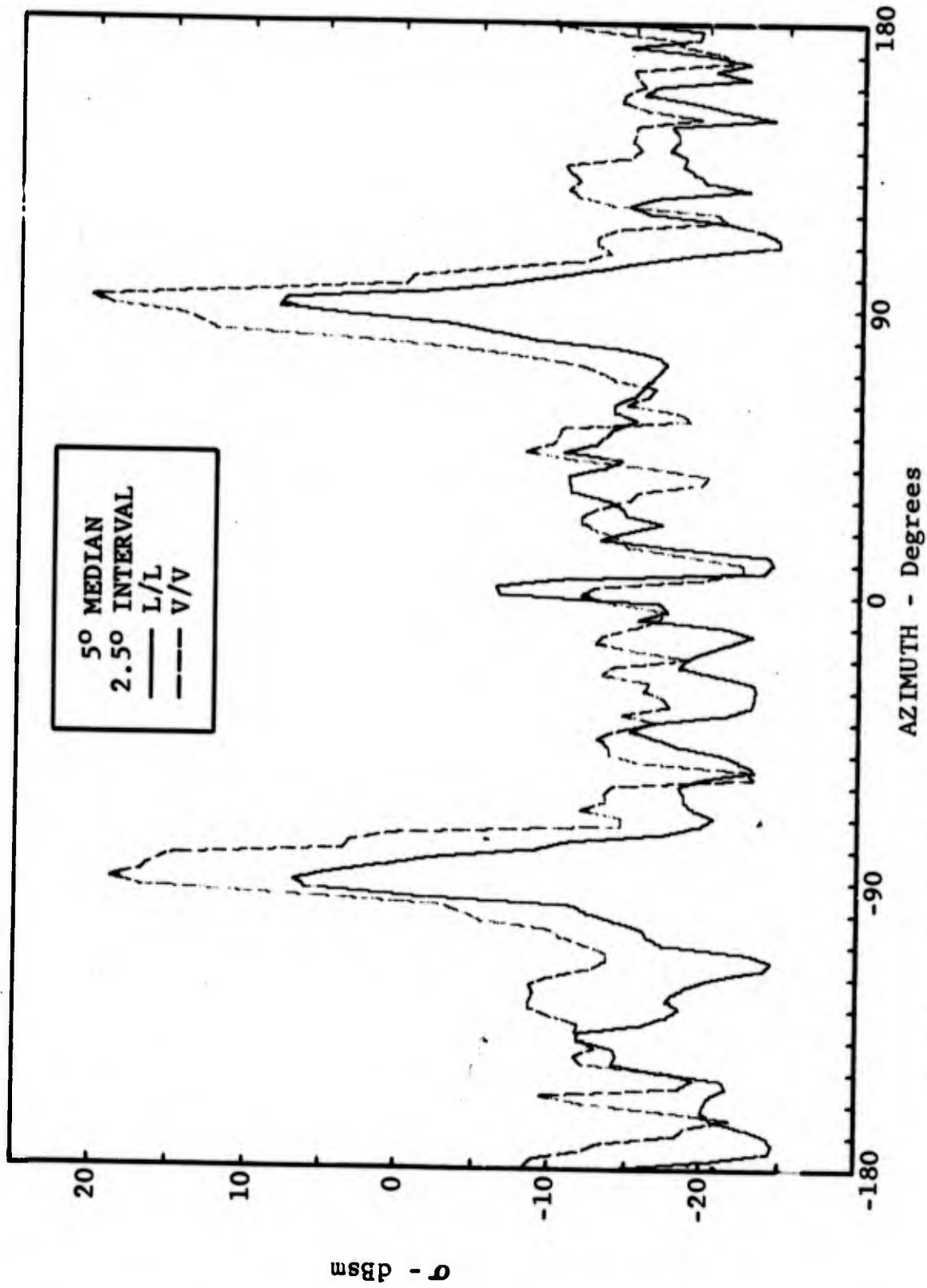


Fig. 3.1-6 MEDIAN RCS OF SCALE MODEL BQM-34A  
(L/L & V/V POLARIZATION, 0° PITCH, 0° ROLL)

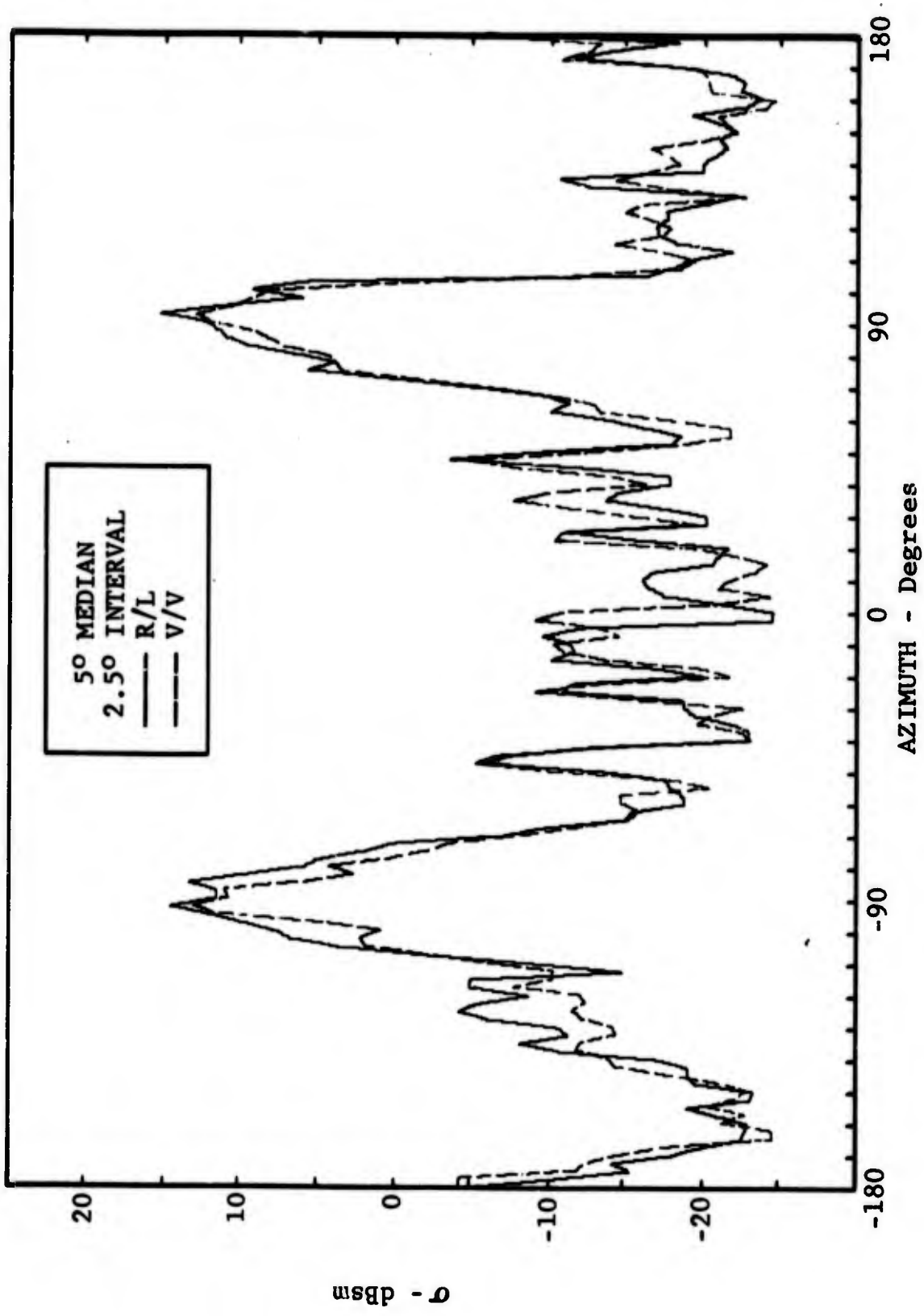


Fig. 3.1.1-7 MEDIAN RCS OF SCALE MODEL BQM-34A  
(R/L & V/V POLARIZATION, 0° PITCH, 20° ROLL)

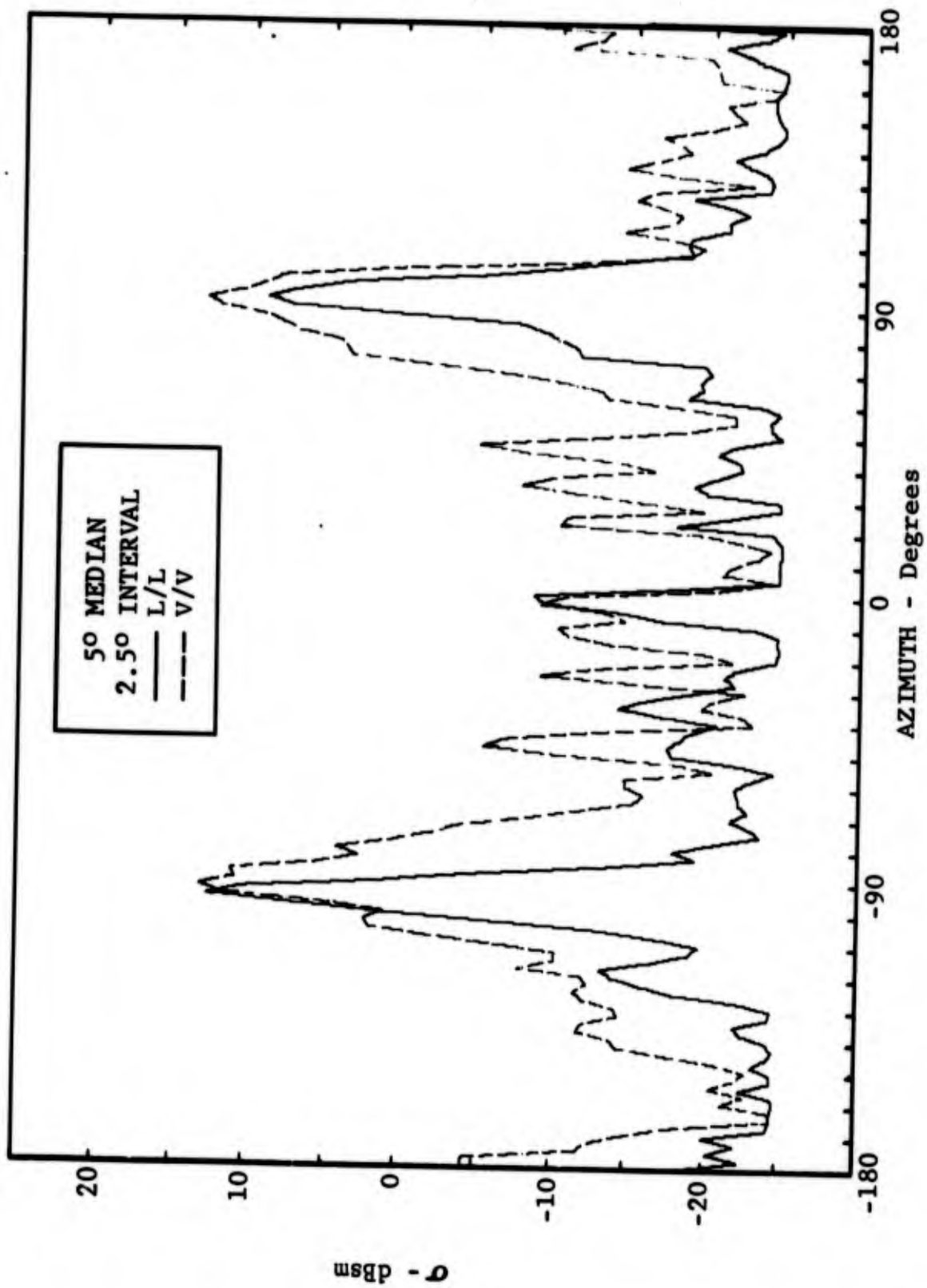


Fig. 3.1-8 MEDIAN RCS OF SCALE MODEL BQM-34A  
(L/L & V/V POLARIZATION, 0° PITCH, 20° ROLL)

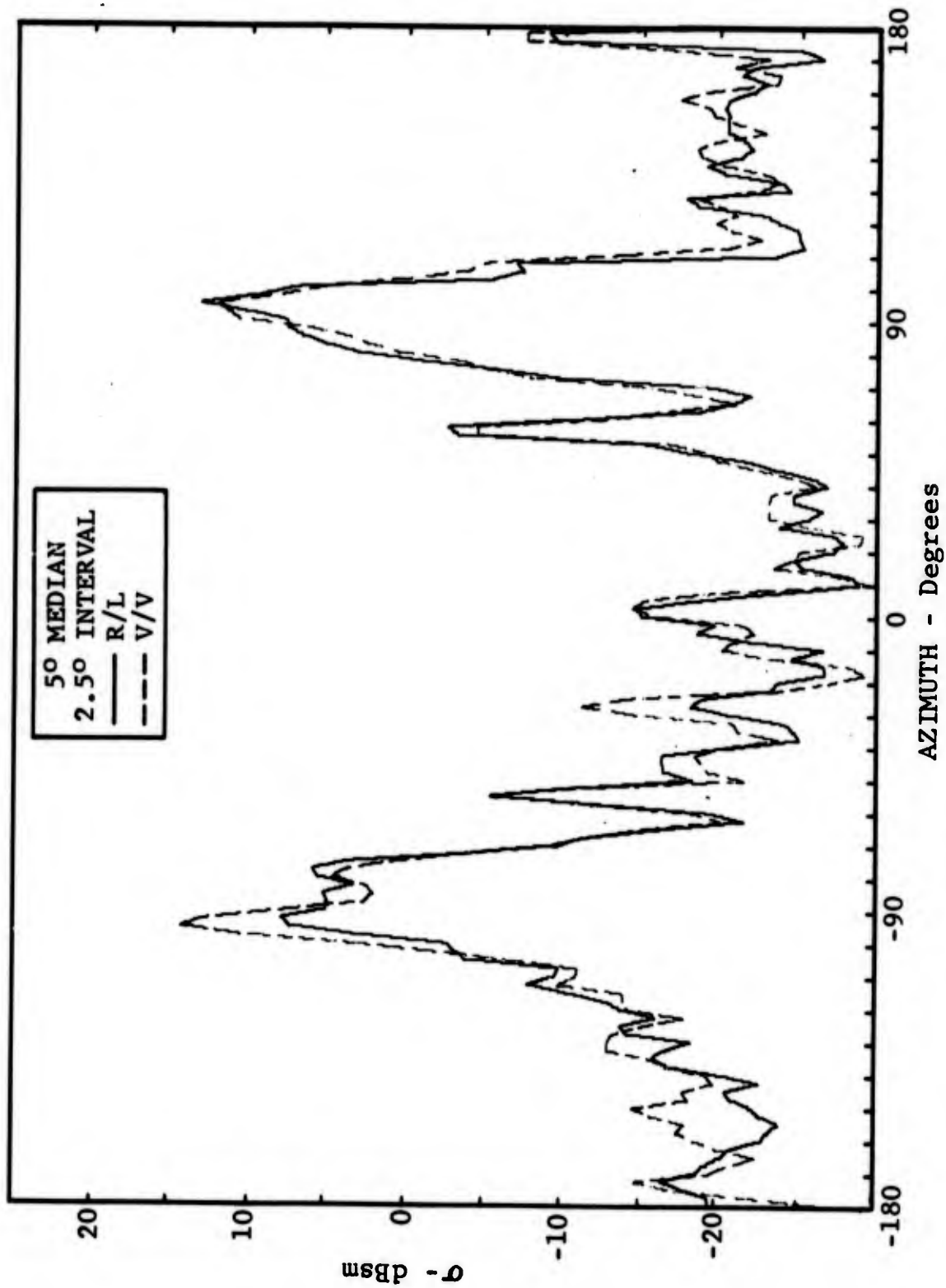


Fig. 3.1-9 MEDIAN RCS OF SCALE MODEL BQM-34A  
(R/L & V/V POLARIZATIONS, 0° PITCH, 45° ROLL)

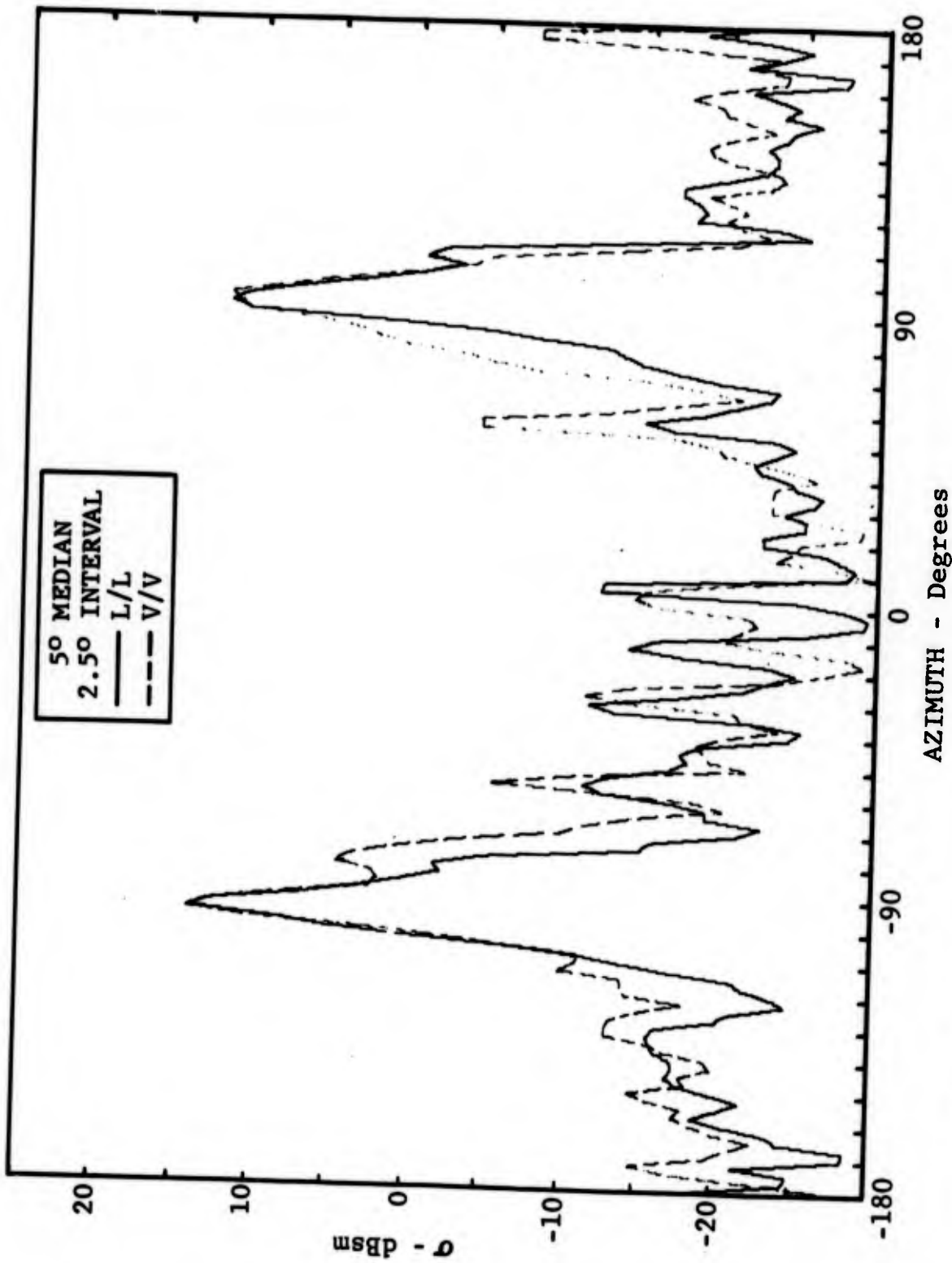


Fig. 3.1-10 MEDIAN RCS OF SCALE MODEL BQM-34A  
(L/L & V/V POLARIZATIONS, 0° PITCH, 45° ROLL)

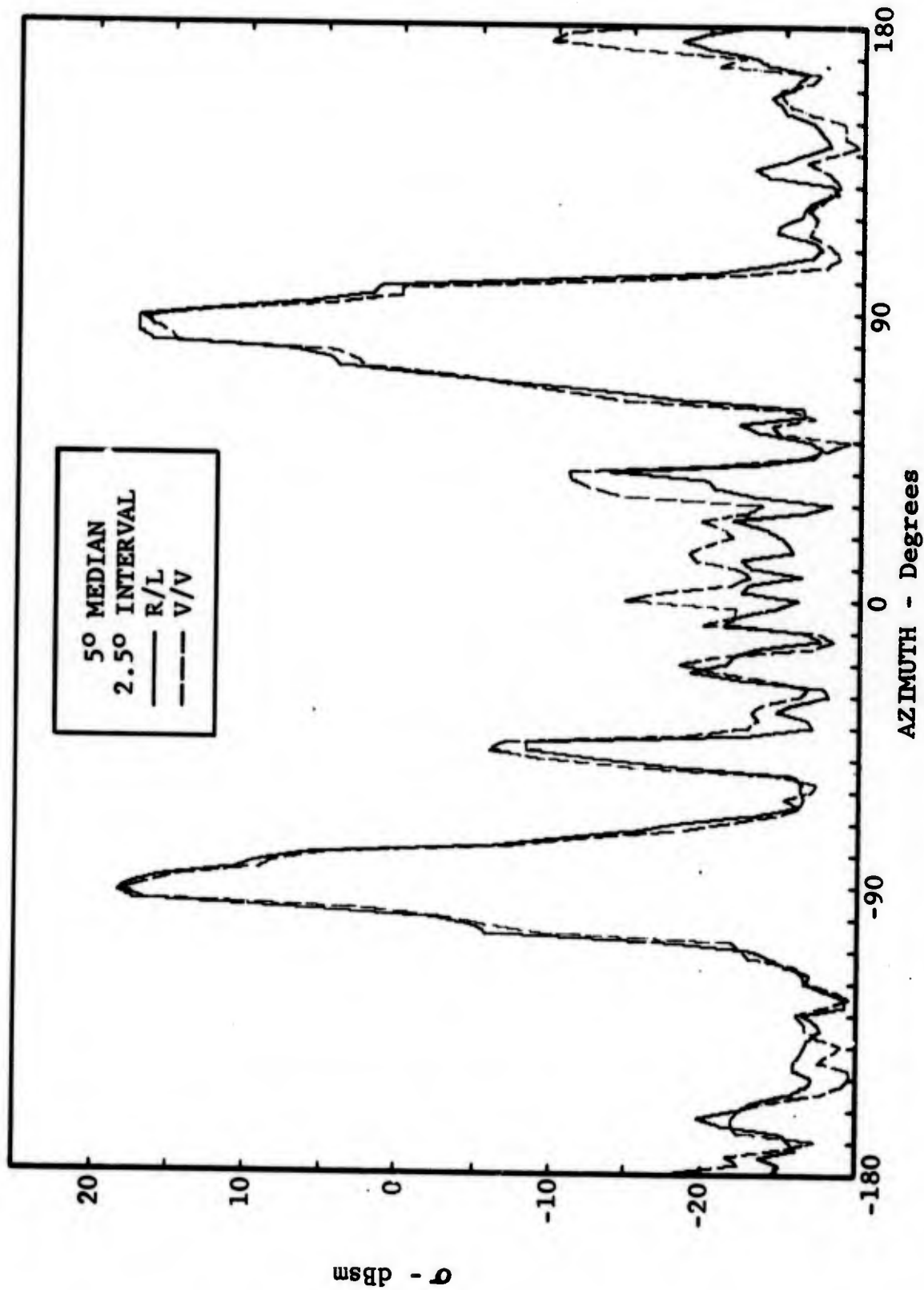


Fig. 3.1-11 MEDIAN RCS OF SCALE MODEL BQM-34A  
(R/L & V/V POLARIZATIONS, 20° PITCH, 0° ROLL)

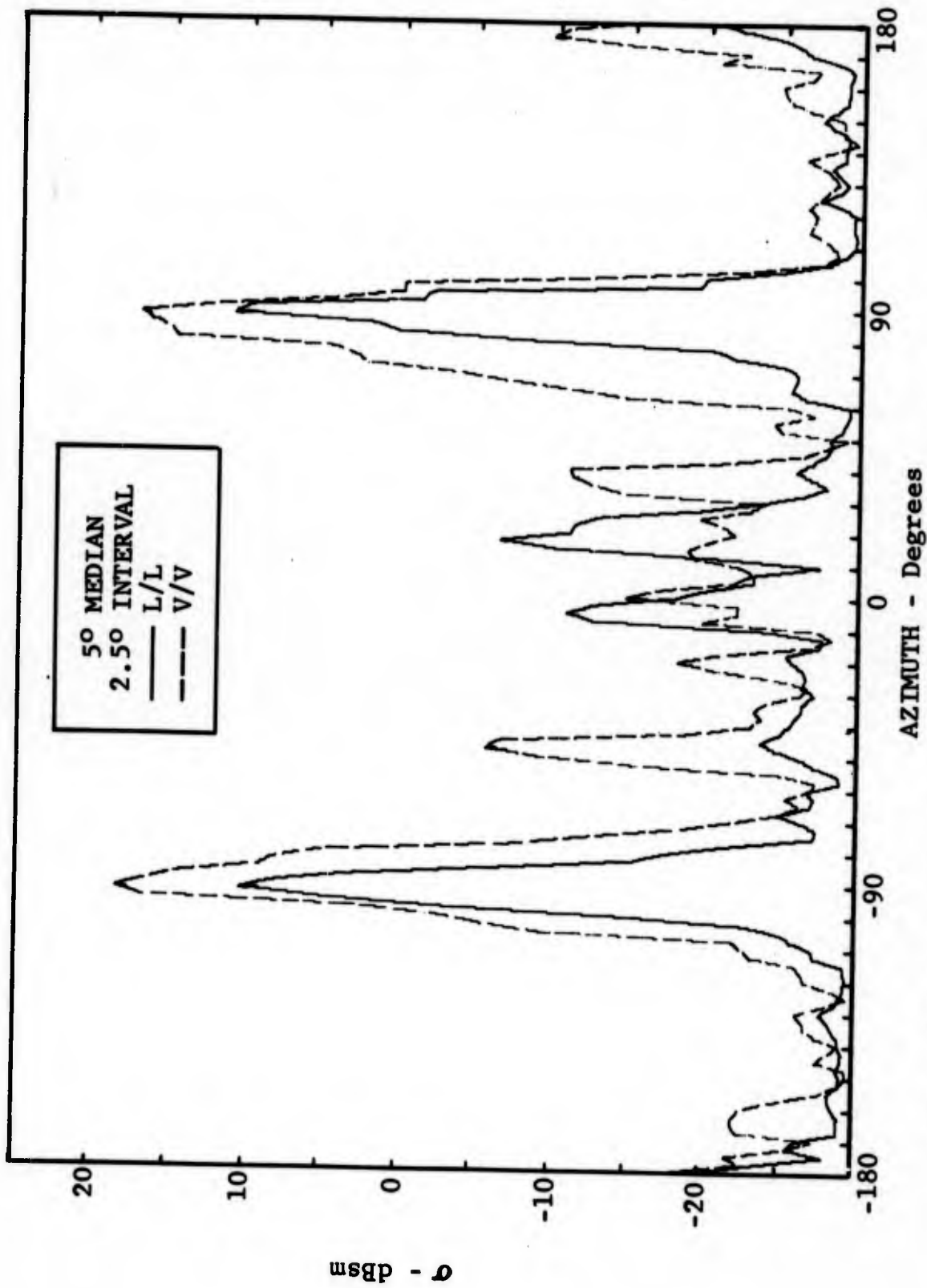


Fig. 3.1-12 MEDIAN RCS OF SCALE MODEL BQM-34A  
(L/L & V/V POLARIZATIONS, 20° PITCH, 0° ROLL)

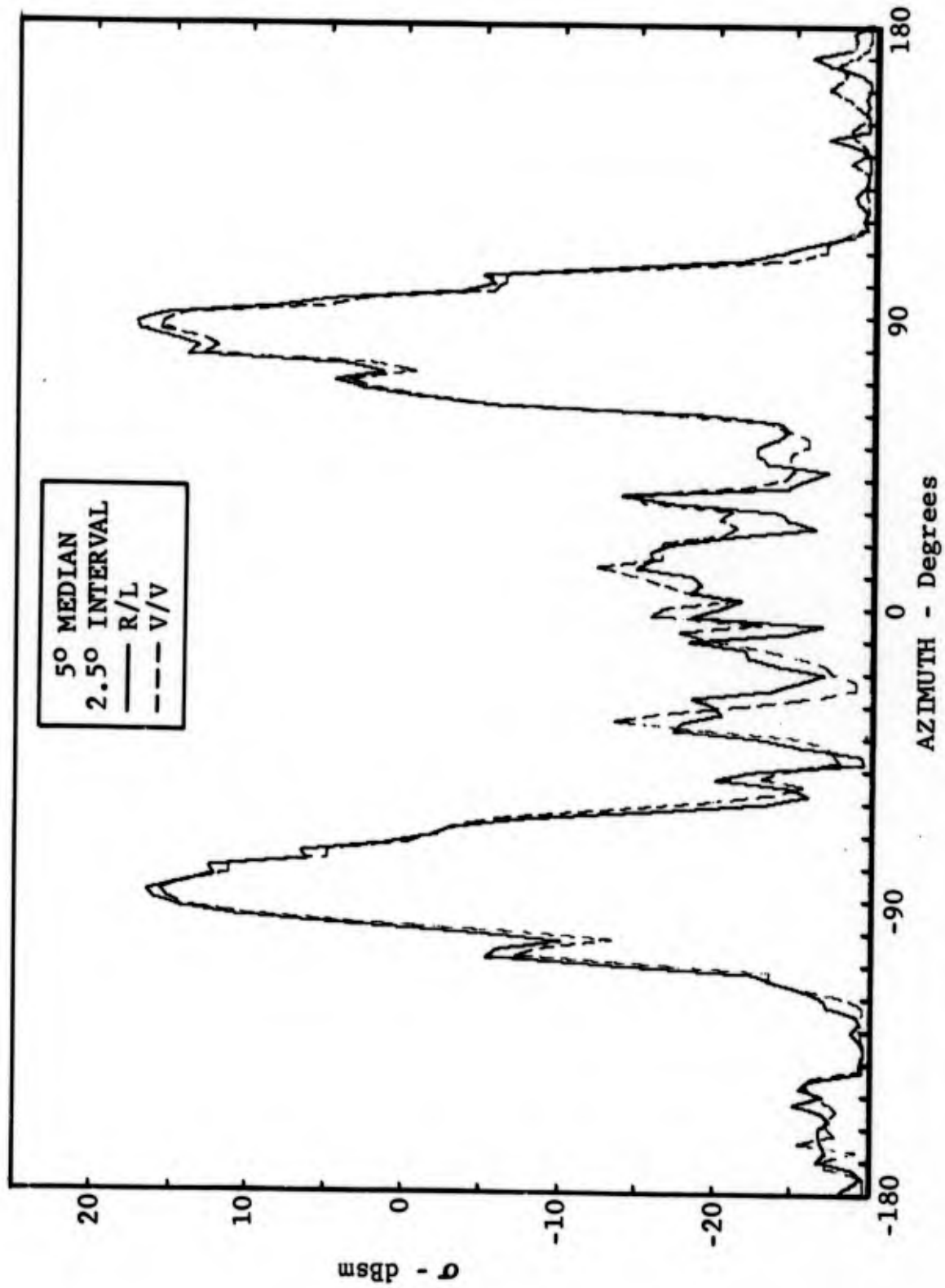


Fig. 3.1-13 MEDIAN RCS OF SCALE MODEL BQM-34A  
(R/L AND V/V POLARIZATION, 45° PITCH, 0° ROLL)

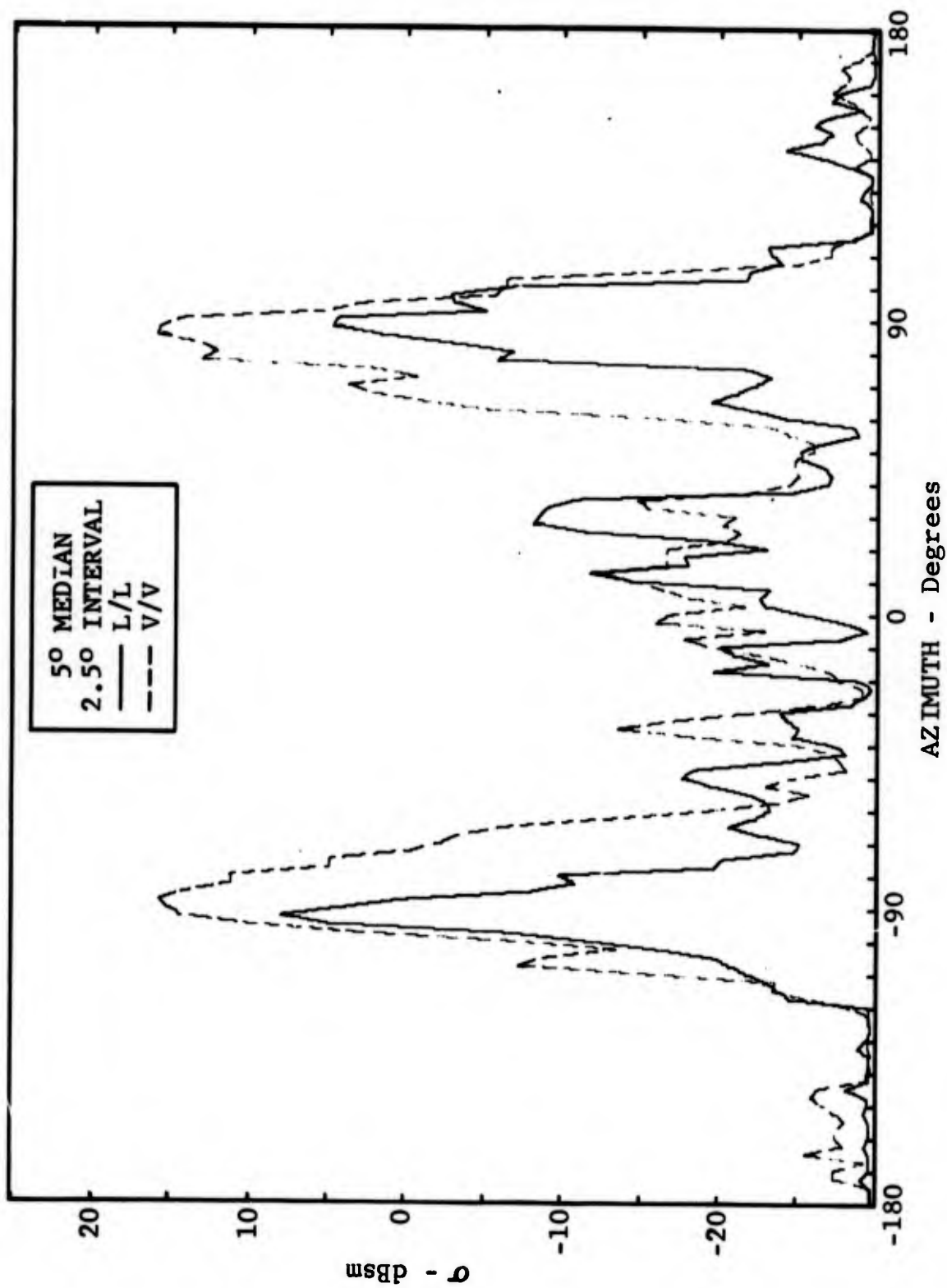


Fig. 3.1-14 MEDIAN RCS OF SCALE MODEL BQM-34A  
(L/L & V/V POLARIZATIONS, 45° PITCH, 0° ROLL)

Table 3.1-1 WIDE ANGLE MEDIAN VALUES  
OF SCALE MODEL RCS

PITCH = 0°

ROLL ANGLE				
	0	20	45	90
VV	-15.4	-16.6	-21.7	-18.1
RL	-19.1	-17.0	-22.5	-22.7
LL	-17.4	-22.3	-22.4	-24.4

ROLL = 0°

PITCH ANGLE					
	-45	-20	0	20	45
VV	-27.9	-27.4	-15.4	-22.1	-22.8
RL	-27.6	-27.8	-19.1	-24.5	-23.0
LL	-25.9	-29.0	-17.4	-25.7	-24.1

### 3.2 DISCRETE SCATTERER MODEL

A complex radar target may be described as a large number of individual shapes that scatter energy in virtually all directions. Analysis of high-resolution measurements have shown that, in the frontal region, the scattering can primarily be associated with discontinuities on the target, such as the leading edges of inlets. The conventional approach to describing the scintillation of radar echoes resulting from the phase interference of these individual sources of scattering is to assume a random spatial distribution of these scattering points with corresponding random amplitude and phases. The resultant probability density function, in conjunction with assumed correlation properties with time and frequency, provides an extremely useful technique for describing radar system performance for the case in which a wide range of targets may be encountered. This approach has been utilized extensively by Swerling (Skolnik, 1962).

The desire to evaluate the performance of sophisticated radars, in which use is made of wideband techniques and/or specialized functions, has created a need for a more flexible model of target scattering characteristics than the simple statistical models of Swerling because the Swerling models are not descriptive of target dimensions or specific scattering characteristics. Applications of a target scattering model in cases in which the simple statistical models are inadequate include the determination of (1) target-induced angle tracking errors associated with the glint phenomenon, (2) the target response to a high-resolution waveform, (3) target-induced range tracking fluctuations, and (4) cross section fluctuations for the case of a frequency-diverse MTI system (Pierson and Clay, 1972).

A more accurate representation of target scattering characteristics can be achieved by modeling the target as a number of discrete scatterers whose amplitudes and positions have been determined. In the present state of the art, the use of the discrete scatterer target model provides the best manner of rapidly determining complex target signatures for use in a computer simulation. The signature characteristics obtained with the use of such a model generally provide the accuracy required in simulation. In any event, the use of information concerning the position and amplitude of the significant sources of target scattering in formulating the discrete scatterer target model will enhance the quality of

this model in comparison to one in which the position and amplitude of the scattering sources are assumed to be random.

In particular it was desired to develop a Discrete Scatterer Model of the BQM-34A for this contract for the purpose of calculating the linear glint. Since phase data were not obtained on long pulse measurements of the scale model, the linear glint could not be computed from these measurements. Therefore, since a discrete scatterer model provides both cross section and phase information, models were developed for linear and circular polarizations and the linear glint was computed from the models for the purpose of comparing the effects of target induced tracking errors.

The following paragraphs contain a description of the techniques utilized in the development of a discrete scatterer model, the procedures used to verify the model, and a comparison of the results obtained from the models for the case of linear and circular polarizations.

### 3.2.1 Development of the Discrete Scatterer Model

The discrete scatterer model consists of a number of discrete scatterers whose positions and amplitudes are determined as a function of target orientation. The scattering model can be expressed in the following form:

$$\sqrt{\sigma(\theta)} = \sum_{i=1}^N a_i(\theta) e^{j2kr_i \cos(\theta-\theta_i)} \quad (3.2-1)$$

where:  $a_i(\theta)$  denotes the amplitude of the  $i$ th scattering source as a function of target rotation angle

$r_i \cos(\theta-\theta_i)$  denotes the position of the source with respect to the target reference point (projected onto the target rotation plane)

$$k = \frac{2\pi}{\lambda}$$

$\lambda$  = wavelength

The scattering model can be obtained by using purely analytical formulations of target scattering or by using measurements data in combination with a knowledge of the characteristics of the basic scattering mechanisms. The normal approach in computing the signature of a complex target by analytical techniques involves (1) the derivation of a simplified geometrical model of the target and (2) the use of high-frequency analytical techniques in determining the scattered field from different regions of the target. Very good results have been achieved in computing the radar cross section of several selected shapes including the cylinder, hemisphere, frustrum, and certain combinations of these bodies (Pierson, 1970; Ross, 1969). Extending the analytical techniques for applications in computing the response of a complex aircraft target is a difficult task. At the present time, state of the art analytical techniques are not adequate to accurately handle the scattering from inlet ducts, engines and exhausts of aircraft type targets. In addition the degree of complexity of analytical scattering formulations is increased and the accuracy is reduced if the target surface contains nonmetallic or poorly conducting material.

Convair Aerospace has developed a technique that utilizes wideband measurements data to isolate and determine the individual scatterer characteristics. There are essentially two steps involved in using measurements data in developing a discrete scatterer model. These steps are (1) isolation of the position of the significant individual scatterers and (2) determination of the directivity pattern and relative motion of these scatterers.

#### 3.2.1.1 Short-Pulse Measurements

As mentioned in the previous paragraphs it is necessary to isolate the individual sources of scattering in the development of a discrete scatterer model. It is therefore desirable to achieve the highest resolution possible in order to isolate, to the highest degree possible, the individual scatterers. The technique utilized by Convair Aerospace to develop a discrete scatterer model is based upon measurements data taken on the Short Pulse Radar Range located at Fort Worth.

Measurements data on the BQM-34A were obtained through use of the X-band short-pulse system which has a 3-inch range resolution capability. The measurement system used to obtain these high-resolution signature data consists of a coherent

X-band transmitter, dual transmit/receive antenna system, coherent wideband receiver, recording system, target rotator system, and environmental shelter (Pierson, et.al., 1970). A brief description of the measurement system and measurement procedures are contained in the following paragraphs.

A block diagram of the radar system is shown in Figure 3.2-1. The subnanosecond width transmitted pulse is generated by high-speed modulation of the CW output of a phase-locked source and is amplified to one kilowatt by a single high-gain pulsed-grid TWT. The received signal is amplified by a low-noise, wideband (4-gigahertz bandwidth) TWT and sampled by one channel of a high-speed dual-channel sampling scope. The dual channel sampling scope provides a sample-and-hold output of the signature data and CW reference at the PRF rate. The signature channel output is envelope-detected and filtered to provide amplitude data. Coherent data is obtained by post-sampling correlation of the received signal with the sampled CW reference output signal. The correlation process is performed on sampled data by the phase comparison circuitry.

A delayed sample of the transmitted waveform is located near the target region in order to provide a reference signal for use in calibrating measurements data. When the attenuation in the transmitter output is increased to provide an increased dynamic range, the calibration reference signal, which is independent of system attenuation, will remain at a constant amplitude. The manner in which this signal is generated is shown in Figure 3.2-1. The transmitted waveform is attenuated, delayed, and injected into the receiver at the leading edge of the 40-nanosecond-wide range window.

The amplitude data, two orthogonal channels of phase data, and the rotation angle are recorded simultaneously on an analog strip chart and on digital magnetic tape. Digital data is sampled and recorded at approximately 0.088-nanosecond time intervals to ensure accurate reproduction of the fine-structure information within a pulse.

The rotator position is recorded to the nearest 0.1 degree. The beginning of each range sweep is synchronized with a fixed aspect increment of 0.2 degree to ensure that repeated measurements will provide data at the same aspect angles.

The air-inflated shelter provides a stable environment which facilitates accurate measurement of coherent short-pulse

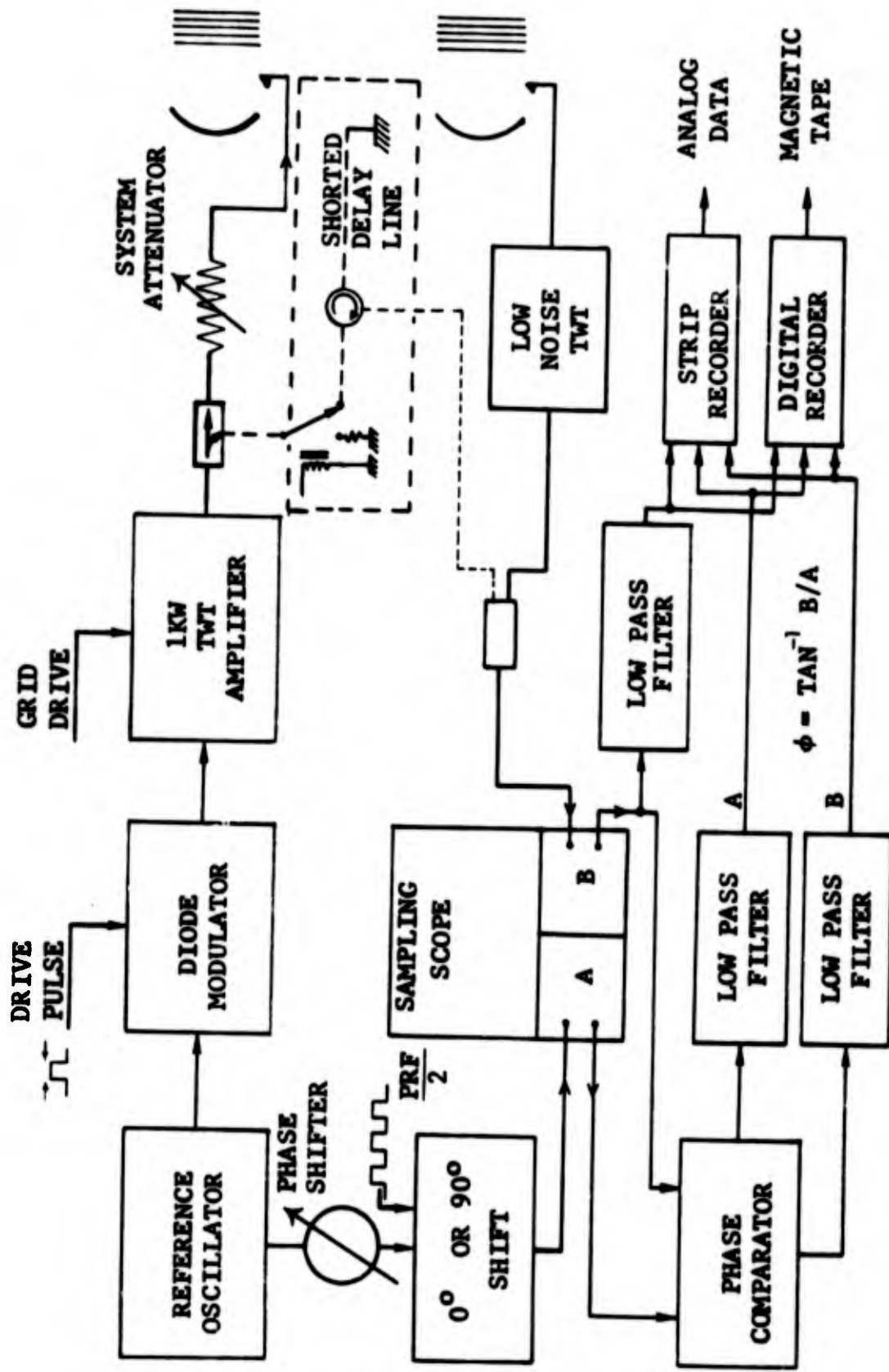


Fig. 3.2-1 SHORT-PULSE RADAR SYSTEM BLOCK DIAGRAM

signatures. The relationship of a typical short-pulse signature measurement to the range geometry is shown in Figure 3.2-2. The screens indicated in the figure are utilized to reduce multipath ground reflections that would appear as time sidelobes and to reduce the background by reducing illumination of the column. These screens are positioned well below the main beam in order to ensure a low vertical field gradient. The measurement system can also be utilized at longer ranges outside the air shelter.

Typical system parameters obtained with the short-pulse system are contained in several published reports (Pierson, 1970; Pierson and Clay, 1972). The value of these parameters will vary depending upon the target and system setup. For a large target such as the BQM-34A the antenna system consists of two 2-foot parabolic dishes with offset feeds. The feeds are defocused in order to provide the wide field required for the measurement of a large target. Field probes taken during measurement of the BQM-34A indicated less than 3-dB variation of the field over the target volume. System sensitivity was approximately -30 to -35 dBsm for the BQM-34A.

Through the use of the short-pulse system most of the sources of scattering can be isolated in range. Selected short-pulse measurements data are shown in Figures 3.2-3 and 3.2-4 to illustrate the resolution capability of the system. Five distinct returns can be observed in Figure 3.2-3.

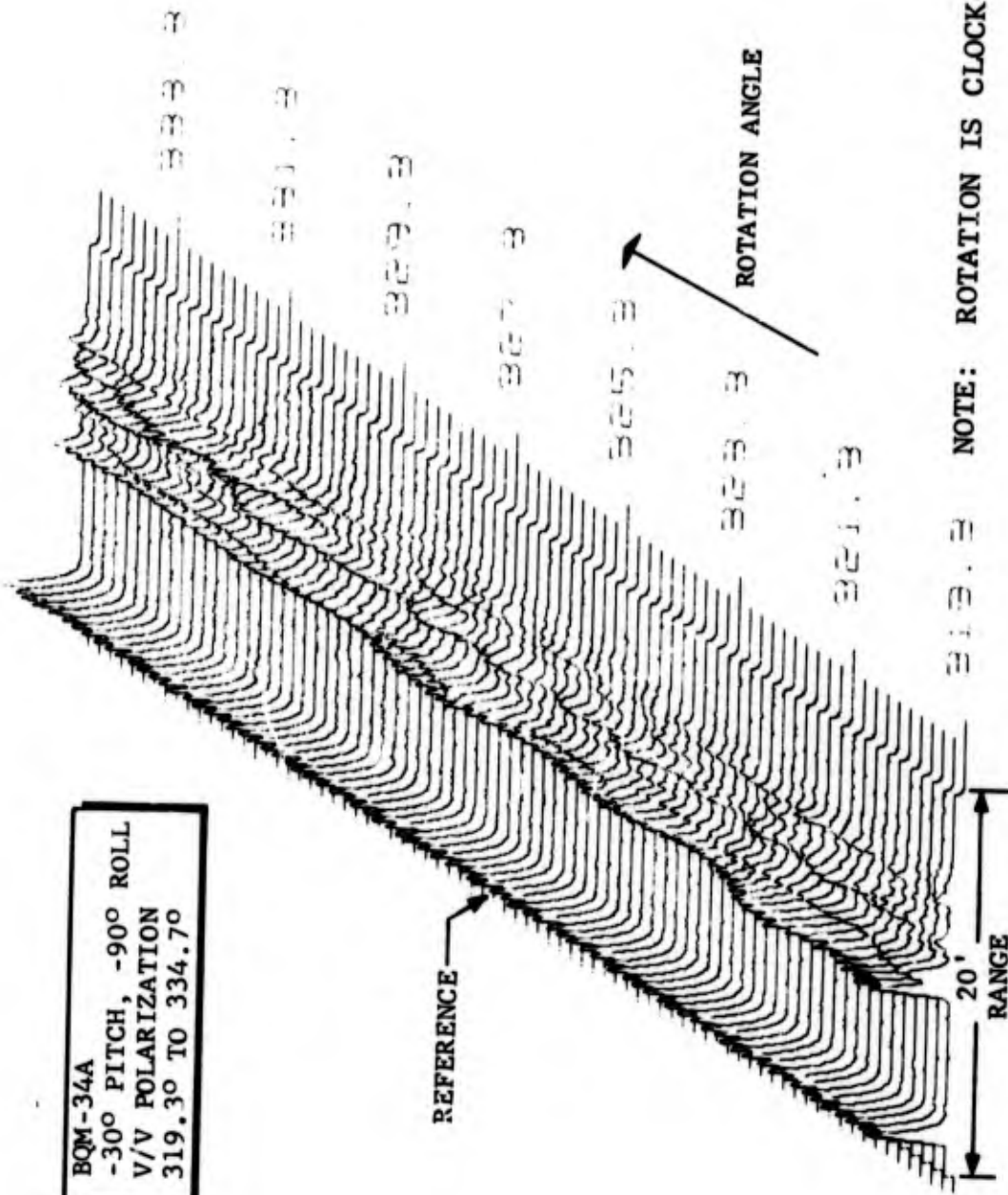
#### 3.2.1.2 Determination of Model Coefficients

The short-pulse signature of a target is characterized by the range resolution of discrete scatterers. The return from each of the scatterers will usually exhibit a change in phase as the target is rotated. The rate of change of this phase with respect to aspect angle constitutes a doppler frequency which is proportional to the perpendicular distance between the location of the scatterer, projected to the plane of target rotation, and the radar line-of-sight. The cross range position of the scatterer may be determined by correlating the measured data with the position of a postulated scatterer.

The first step in this correlation process is to postulate the individual scatterer positions based on the short-pulse measurements data. This can be done since the measurements data are recorded as a function of range for each aspect



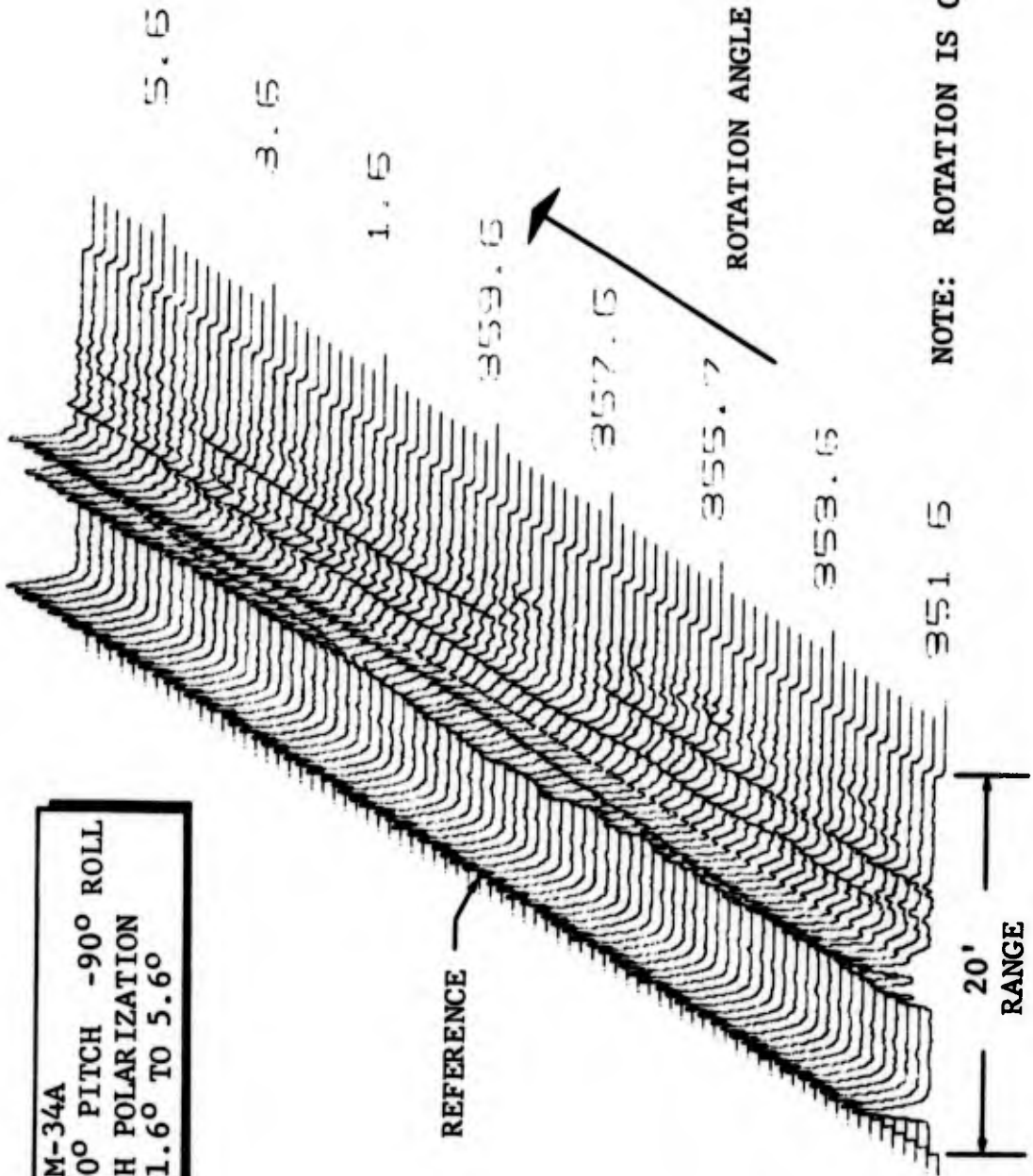
BQM-34A  
 -30° PITCH, -90° ROLL  
 V/V POLARIZATION  
 319.30 TO 334.70



NOTE: ROTATION IS CLOCK-WISE

3.2-3 SHORT-PULSE RCS OF SCALE MODEL BQM-34A  
 (V/V POLARIZATION, -30° PITCH, -90° ROLL)

BQM-34A  
 -30° PITCH -90° ROLL  
 H/H POLARIZATION  
 351.6° TO 5.6°



3.2-4 SHORT-PULSE RCS OF SCALE MODEL BQM-34A  
 (H/H POLARIZATION, -30° PITCH, -90° ROLL)

angle. Therefore, the location in range of each scatterer appears as the projection on the radar line-of-sight relative to the target center of rotation. This is illustrated in Figure 3.2-5. The location of the individual scatterers can therefore be postulated based upon a knowledge of the target once the target center of rotation is known.

Utilizing the postulated position of the scatterers, one can determine the location of these scatterers in range as observed by the short-pulse system. The measured amplitude and phase data can then be extracted at the range position determined from the postulated scatterers. This process is expressed in the following equation:

$$E(\theta, r_n, \theta_n) = \sum_{i=1}^N a_i(\theta) g(r - r_i \cos(\theta - \theta_i)) \delta(r - r_n \cos(\theta - \theta_n)) \cdot e^{j2kr_i \cos(\theta - \theta_i)} \quad (3.2-2)$$

$$\text{where: } \delta(r - r_n \cos(\theta - \theta_n)) = \begin{cases} 1 & \text{if } r = r_n \cos(\theta - \theta_n) \\ 0 & \text{otherwise} \end{cases}$$

$a_i(\theta)$  is the angular amplitude dependence of the  $i$ th scatterer

$g(\alpha)$  is the wideband waveform of the short-pulse system

and  $r_n, \theta_n$  is the postulated scatterer position

The extracted data is then multiplied by the complex conjugate of the geometrical phase of the postulated scatterer to form a correlation function  $C(\theta, r_n, \theta_n)$ .

$$C(\theta, r_n, \theta_n) = E(\theta, r_n, \theta_n) \cdot e^{-j2kr_n \cos(\theta - \theta_n)} \quad (3.2-3)$$

Equation 3.2-3 can be reduced to the following form:

$$C(\theta, r_n, \theta_n) = \sum_{i=1}^N a_i(\theta) g \left[ (X_n - X_i) \cos \theta + (Y_n - Y_i) \sin \theta \right] \cdot e^{-j2k \left[ (X_n - X_i) \cos \theta + (Y_n - Y_i) \sin \theta \right]} \quad (3.2-4)$$

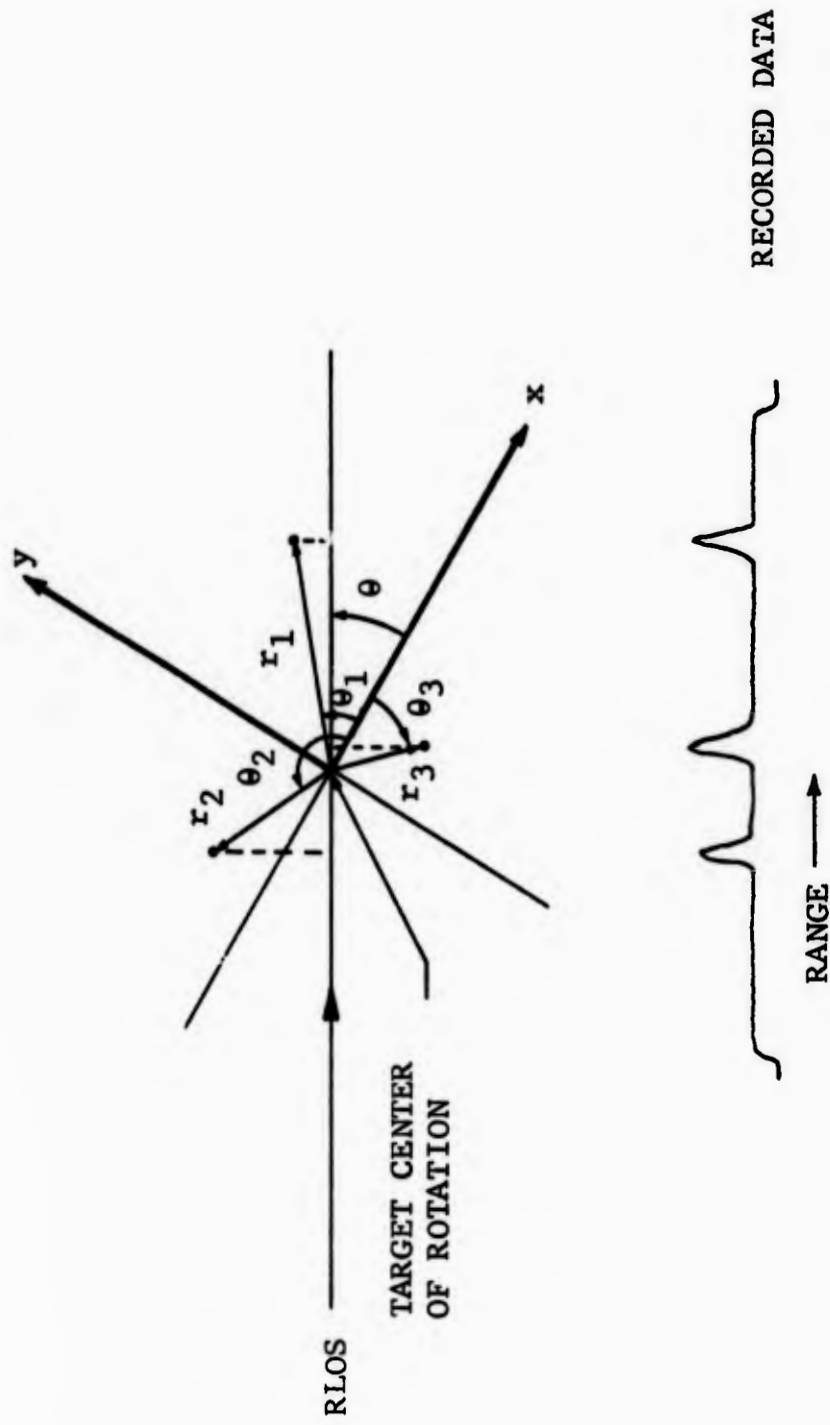


Fig. 3.2-5 SCATTERER COORDINATE GEOMETRY

The cross-range position of the scatterers which are approximately in the same range cell as the desired scatterer can be determined by computing the Fourier transform of Equation 3.2-4 with respect to aspect angle. (This process is analogous to the formation of a synthetic aperture.)

$$T'(\gamma, r_n, \theta_n) = \frac{1}{2\Delta\theta} \int_{-\Delta\theta}^{\Delta\theta} C(\theta, r_n, \theta_n) e^{-j\gamma\theta} d\theta \quad (3.2-5)$$

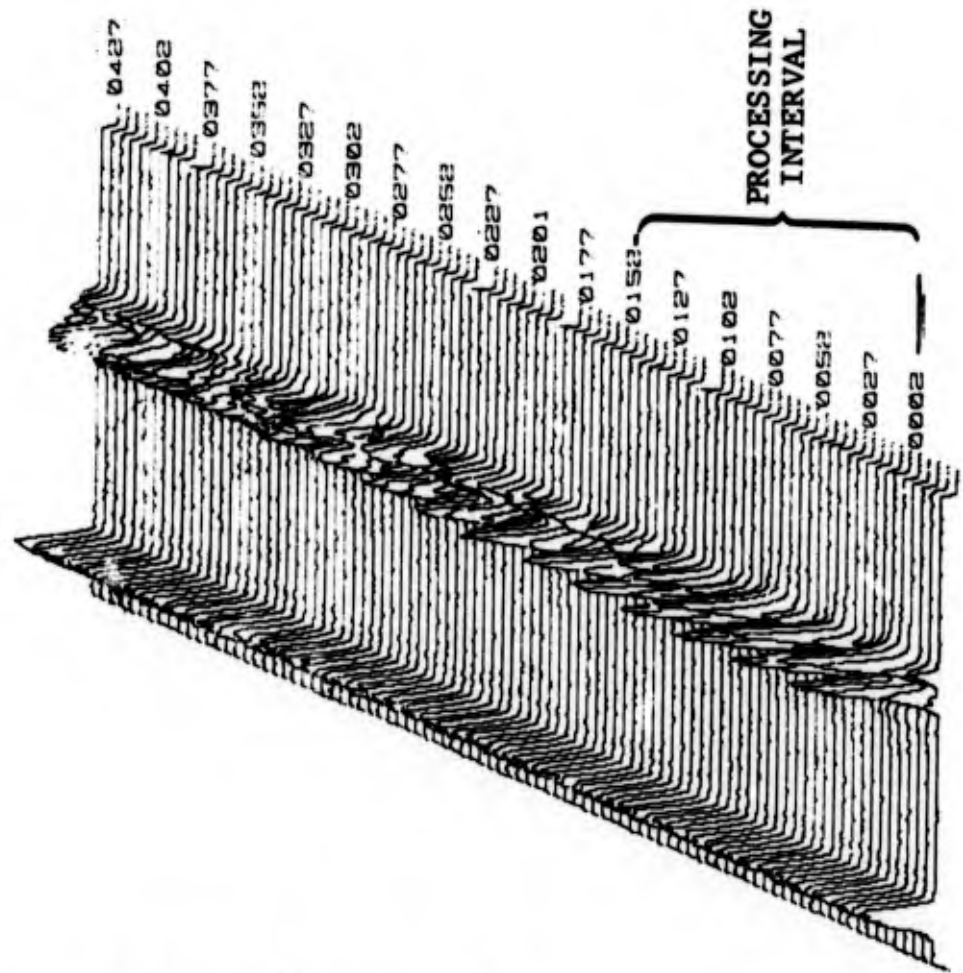
where:  $\gamma = 2ky$  ( $y$  being the cross range dimension)

The transformed function  $T'$  can be utilized to determine the difference in cross-range position of the postulated scatterer and the actual scatterer. Utilizing a 128 point transform ( $25.6^\circ$  of short pulse data) it is possible to achieve a cross range resolution of approximately 1.45 inches. It can be seen from equations 3.2-4 and 3.2-5 that if the postulated scatterer and the actual scatterer positions are the same, the scatterer will appear at zero cross-range. Since it is desired to completely isolate each scatterer, it is necessary to filter the transformed data  $T'$  in cross range if other scatterers are in the same range cell.

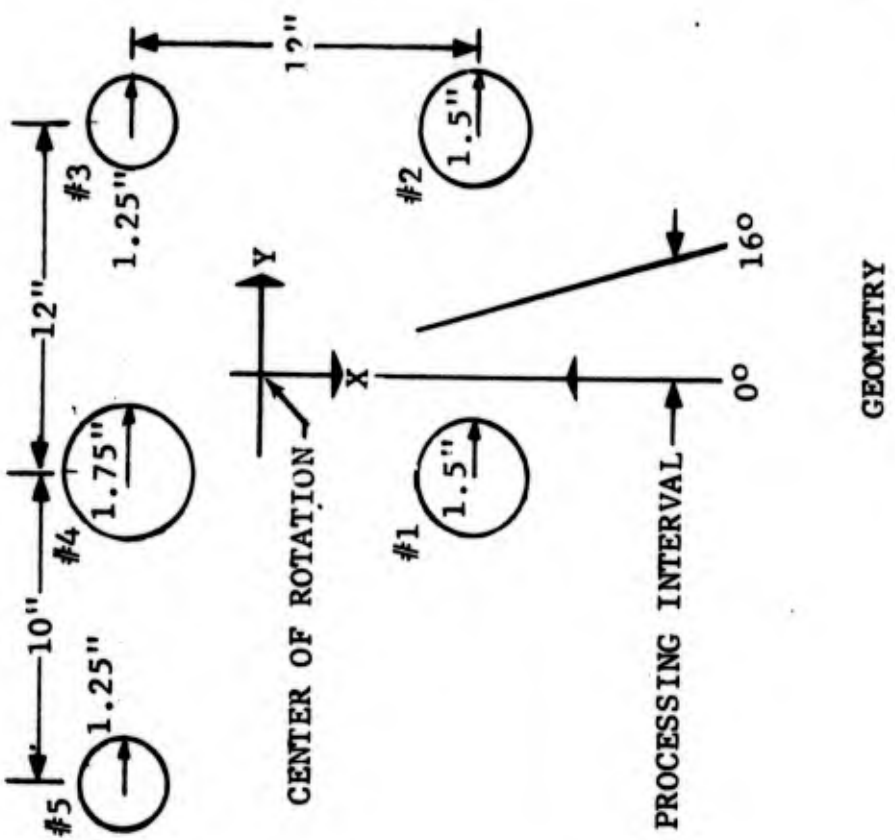
$$T(\gamma, r_n, \theta_n) = T'(\gamma, r_n, \theta_n) * F(\gamma) \quad (3.2-6)$$

The filtered function  $T$  may then be inverse transformed to obtain the amplitude variation of a single scatterer as a function of aspect angle. It is therefore possible to describe the amplitude variation of a scatterer by use of the filtered function  $T$  and the scatterer position.

Perhaps this process may best be described through an example. Figure 3.2-6 contains the geometry and plot of the short pulse data taken on five spheres. The data were processed over a sixteen degree window following the steps outlined above. Positions were postulated for each of the spheres based on the geometry and measurements data, amplitude and phase data were extracted at the range locations determined from the postulated scatterers and the correlation function for each scatterer formed. The results of transforming, filtering and inverse transforming the correlation function are shown for each of the spheres in Figures 3.2-7 and 3.2-8. The cross-range filtering was accomplished simply



SHORT PULSE DATA



GEOMETRY

Fig. 3.2-6 SHORT-PULSE RESPONSE OF FIVE-SPHERE TARGET

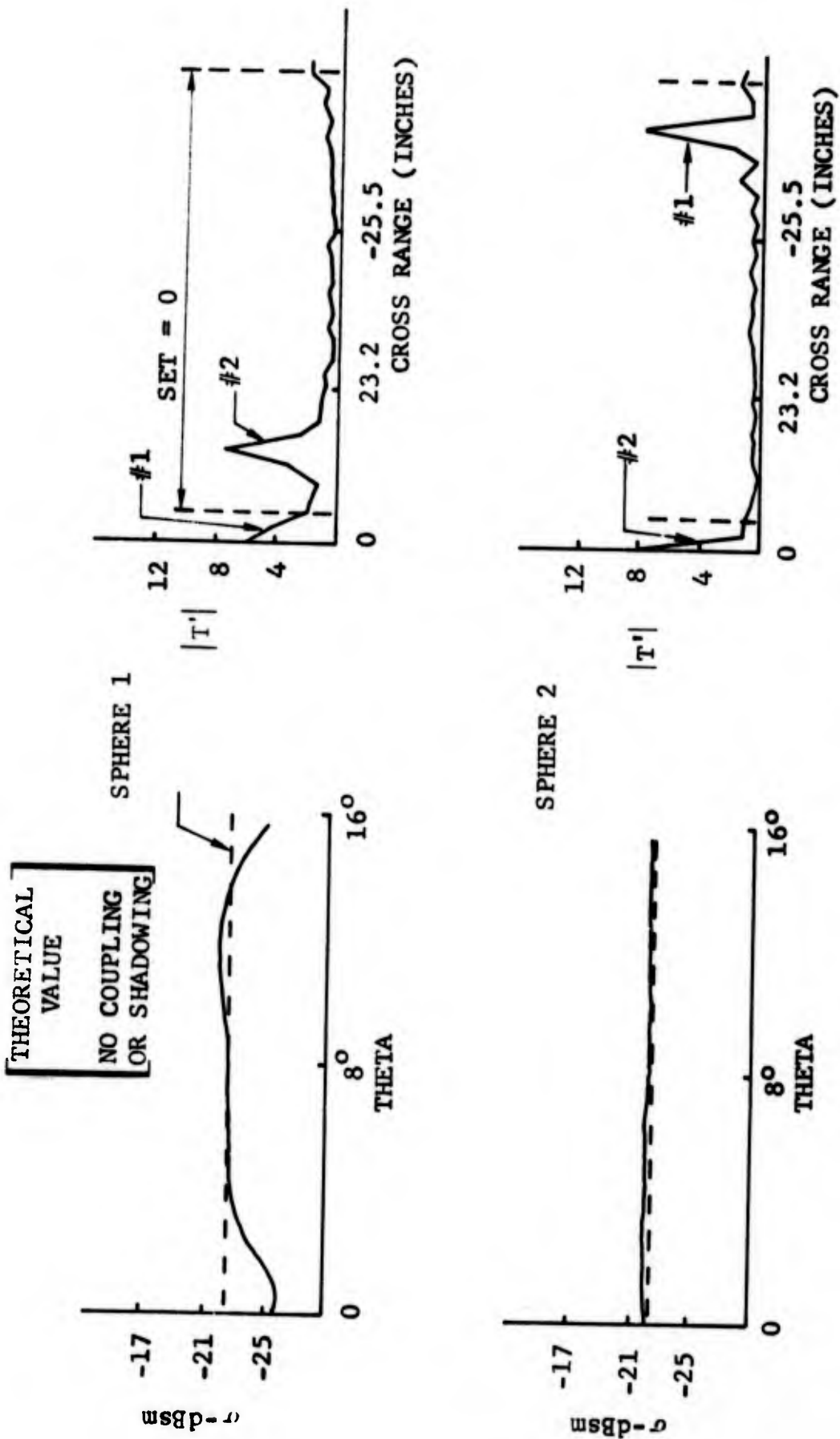


Fig. 3.2-7 RESOLVED AMPLITUDE FUNCTION AND CROSS RANGE RESPONSE (SPHERES 1 AND 2)

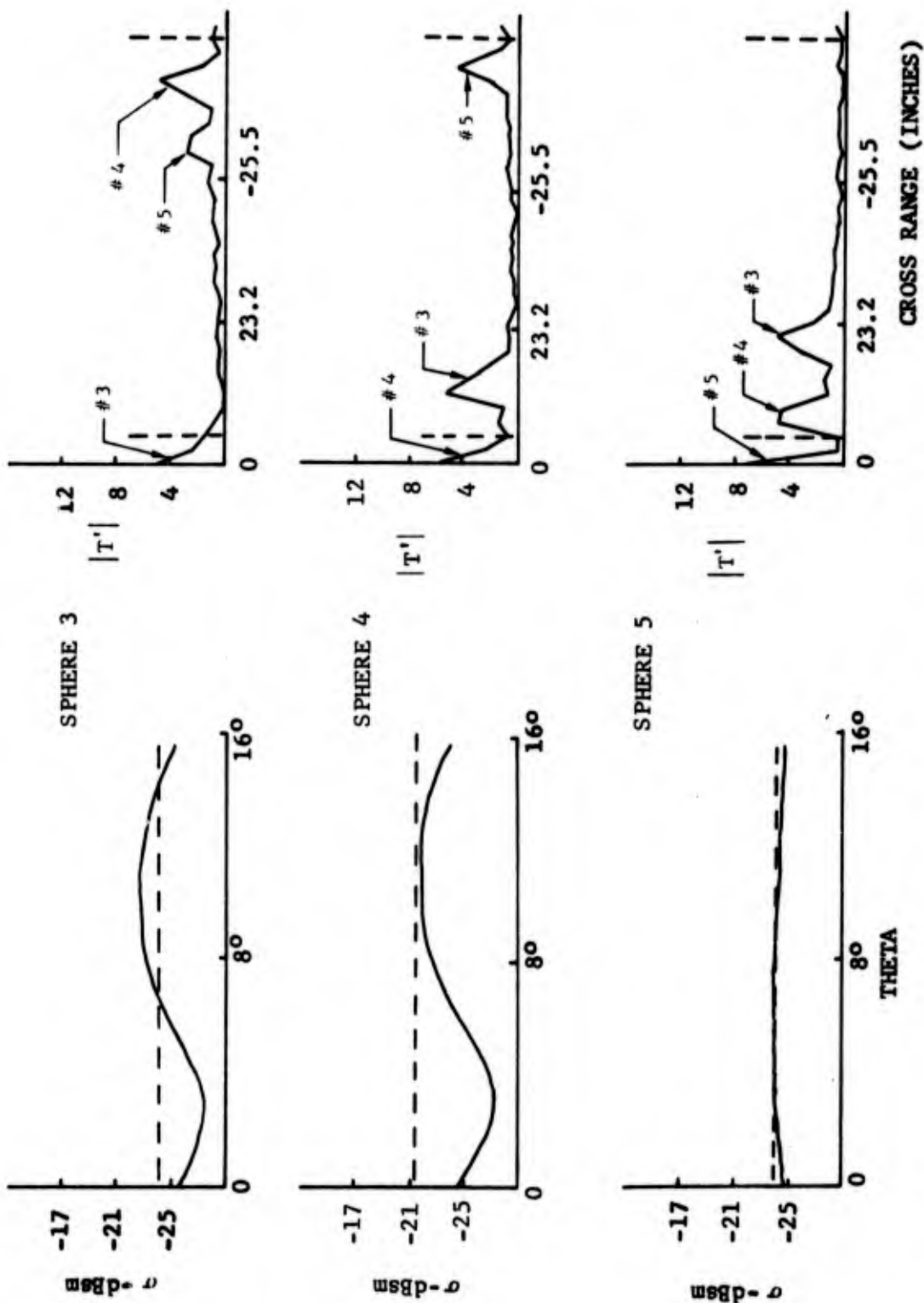


Fig. 3.2-8 RESOLVED AMPLITUDE FUNCTION AND CROSS RANGE RESPONSE (SPHERES 3, 4 AND 5)

by setting equal to zero the data beyond the expected cross-range position of the scatterer as shown in Figures 3.2-7 and 3.2-8. It should be noted that the data presented are the "unfolded" output of the Fourier transform. The theoretical value of each sphere, with no shadowing or coupling assumed, is plotted as a dashed line in the figures.

### 3.2.1.3 Computation of RCS and Glint

As explained in the previous section the amplitude variation of each scatterer as a function of aspect angle can be obtained by inverse transforming the filtered function  $T(\gamma, r_n, \theta_n)$  as shown below:

$$a_i(\theta) = \int T_i(\gamma) e^{j\gamma\theta} d\theta \quad (3.2-7)$$

Equation 3.2-7 can be expressed in terms of a summation in the following manner:

$$a_i(\theta) = \sum_{\ell=0}^{M-1} T_i(\gamma_\ell) e^{j\gamma_\ell \theta} \quad (3.2-8)$$

Substituting Equation 3.2-8 into Equation 3.2-1 results in the following expression for radar cross section.

$$\sqrt{\sigma(\theta)} = \sum_{i=1}^N \left[ \sum_{\ell=0}^{M-1} T_i(\gamma_\ell) e^{j\gamma_\ell \theta} \right] e^{j2kr_i \cos(\theta - \theta_i)} \quad (3.2-9)$$

or in terms of a discrete Fourier transform

$$\sqrt{\sigma(n)} = \sum_{i=1}^N \left[ \sum_{\ell=0}^{M-1} T_i(\gamma_\ell) e^{j\frac{2\pi\ell n}{M}} \right] e^{j2kr_i \cos(\theta - \theta_i)} \quad (3.2-10)$$

for  $n = 0, 1, \dots, M-1$

In computing the cross section, the sum on  $\ell$  has to be computed only for the non-zero terms.

The method described above has been found to work well for scatterers which do not have a rapidly varying angular

amplitude dependence. Wing speculars are examples of scatterers having a rapidly varying amplitude. If processed using this technique, these specular returns would be distributed in cross-range and require a very large number of coefficients to describe them. To avoid the necessity of storing a large number of coefficients, specular type scatterers were modeled using analytical techniques. Wing speculars for example were modeled using sinc(X) functions. The expression given for the radar cross section in Equation 3.2-10 would therefore have to be modified to include these analytical expressions in regions where specular-type scatterers are present.

The linear glint may be computed by either one of two methods: (1) by use of the balance point equation or (2) by use of the phase derivative process. The glint may be computed using the following balance point equation (Peters and Weimer, 1963).

$$G(\theta) = \text{Re} \left\{ \frac{\sum_{i=1}^N (y_i \cos\theta - x_i \sin\theta) \left[ \int T_i(\gamma) e^{j\gamma\theta} d\gamma \right] e^{j2k(x_i \cos\theta + y_i \sin\theta)}}{\sqrt{\sigma(\theta)}} \right\} \quad (3.2-11)$$

The use of this equation, however, implies that the target can be assumed to be represented by a number of point scatterers. In deriving the Discrete Scatterer Model it was at times necessary to include scattering complexes (more than one scatterer) therefore making the use of Equation 3.2-11 questionable. Since the output of the Discrete Scatterer Model  $\sqrt{\sigma(\theta)}$  is a complex number, the phase of the return can be computed by taking the arctangent of the two components. The linear glint may therefore be found from the rate of change of phase with respect to rotation angle using the following relation.

$$G(\theta) = \frac{1}{2k} \frac{d\phi}{d\theta} \quad (3.2-12)$$

where: 
$$\phi = \tan^{-1} \left[ \frac{\text{Im}(\sqrt{\sigma(\theta)})}{\text{Re}(\sqrt{\sigma(\theta)})} \right]$$

### 3.2.2 Verification of the Discrete Scatterer Model

The Discrete Scatterer Model was verified by comparing the RCS computed with the use of the model with measured RCS values. This comparison includes the basic structures of the RCS patterns and cumulative distributions of the RCS within the small angular sectors.

A visual comparison of the analog plots of the measured long-pulse data and the three-dimensional plots of the measured short-pulse data indicated that certain scattering phenomena which are observed in selected short-pulse data are not observed in the long-pulse measurements results. Additional investigation of the two measurements results indicated that the long-pulse measurements data, within certain angular sectors, were extremely sensitive to small variations in the initial target position on the rotator. It was observed that a very small change in the initial target position could result in significant changes in the measured RCS.

A technique was proposed in order that the RCS obtained using the Discrete Scatterer Model could be compared with the measurements data upon which the model is based. This technique involves the computation of the long-pulse radar cross section using the measured short-pulse data. The technique is illustrated in the block diagram of Figure 3.2-9.

The short-pulse signature is in the form of a complex amplitude (using the coherent phase data) versus time where the carrier frequency has been removed. By processing the data using a Fourier transform, the corresponding frequency response can be obtained. As this frequency response function consists of the product of the target scattered field response and the radar system waveform (Pierson, et.al., 1970; Liang and Clay, 1973), the target response can be obtained by dividing the transformed data by the radar system waveform. (This waveform can be obtained by measuring the response of a calibration target whose frequency response can be accurately computed.) Then, the target response function can be multiplied by the frequency spectrum of the desired system waveform and a new target response obtained in the frequency or time domain. The technique obviously is not applicable if the bandwidth of the desired system waveform exceeds that of the measurement system.

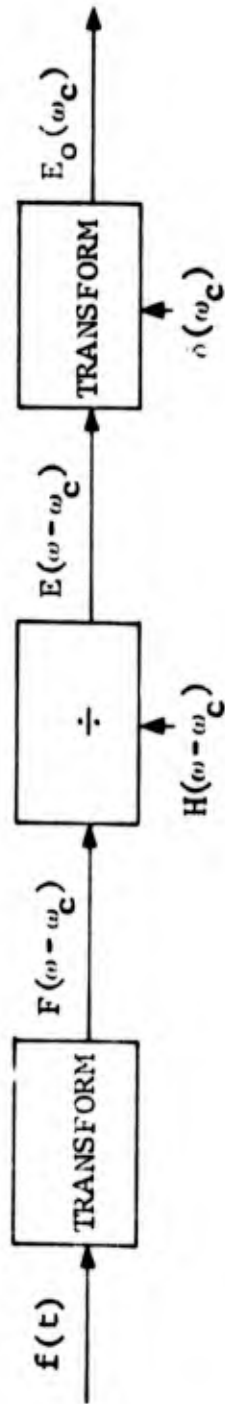


Fig. 3.2-9 TARGET RESPONSE COMPUTED FROM MEASURED SHORT-PULSE DATA

For the case of a single frequency response at the carrier frequency of the short-pulse system, the long-pulse RCS is computed by summing the in-phase and quadrature signals obtained at each range sample within the target region. Thus, for the case of the BQM-34A, the equivalent long-pulse RCS could be obtained by summing the phase data from sample 120 to 480, a distance of approximately 15 feet. These sums are then calibrated using the summed response of a referenced target. It is expected that these data would be somewhat noise sensitive due to the large bandwidth of the measurement system; however, the general trends and average value of the cross section should be accurate.

Selected RCS data computed with the use of the Discrete Scatterer Model are compared with both the long-pulse measurements results and the long-pulse RCS computed directly from short-pulse measurements data. The data are plotted in Figures 3.2-10 through 3.2-13 in the form of RCS versus angle and cumulative distributions within a given angular sector.

All of the results are in reasonably good agreement; however, the RCS computed using the model and that computed from the short-pulse data generally compare more favorably with each other than with the measured long pulse data. This feature is attributed to the sensitivity of the measured RCS to slight deviations in the initial positioning of the target.

### 3.2.3 Comparison of RCS and Glint

The RCS and glint were computed within selected angular sections using the discrete scatterer model and Equations 3.2-10 through 3.2-12. Selected results are presented in Figures 3.2-14 through 3.2-17. These results are typical of those obtained in several other small angular sectors. The RCS shown in Figure 3.2-14 is representative of the signature of a small number of dominant scatterers whose relative phase is slowly varying, whereas the RCS shown in Figure 3.2-16 is representative of a larger number of scatterers whose relative phase varies rapidly. The V/V and R/L signatures shown in Figure 3.2-16 also contain an analytical representation of the specular return from the leading edge of the wing at aspects near  $-45^\circ$ .

The different characteristics of the target RCS in the two angular sectors are indicated in the target glint within those sectors. The slowly varying RCS returns within the angular sector from  $-15^\circ$  to  $0^\circ$  correspond to the small, slowly

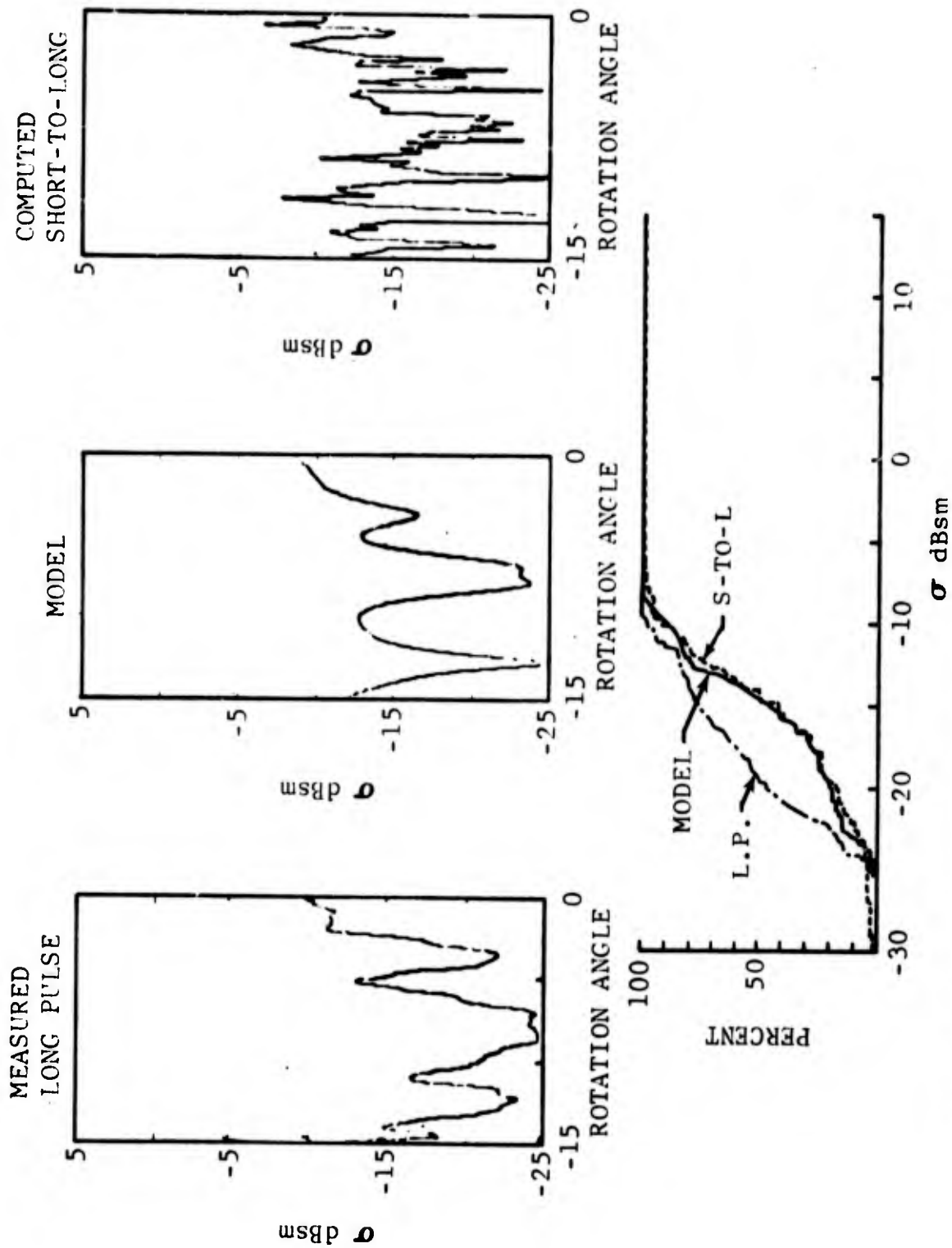


Fig. 3.2-10 DISCRETE SCATTERER MODEL VERIFICATION  
 (V/V POLARIZATION, 0° PITCH, 0° ROLL, -15° TO 0°)

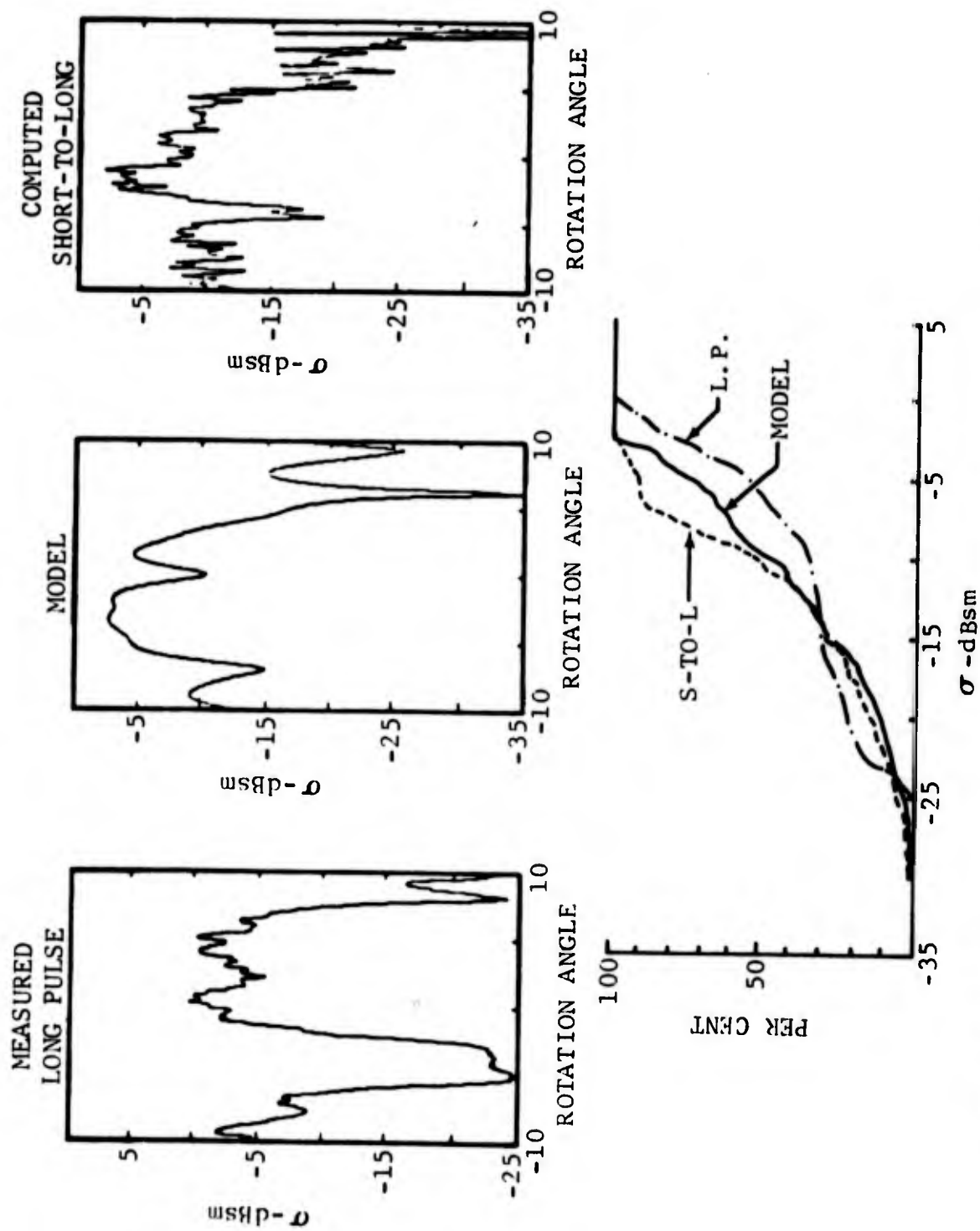


Fig. 3.2-11 DISCRETE SCATTERER MODEL VERIFICATION  
(V/V POLARIZATION, 0° PITCH, -90° ROLL, -10° TO 10°)

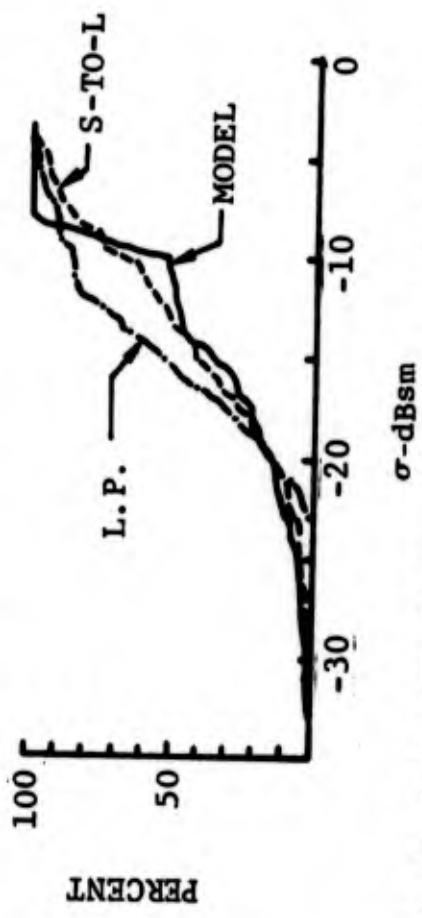
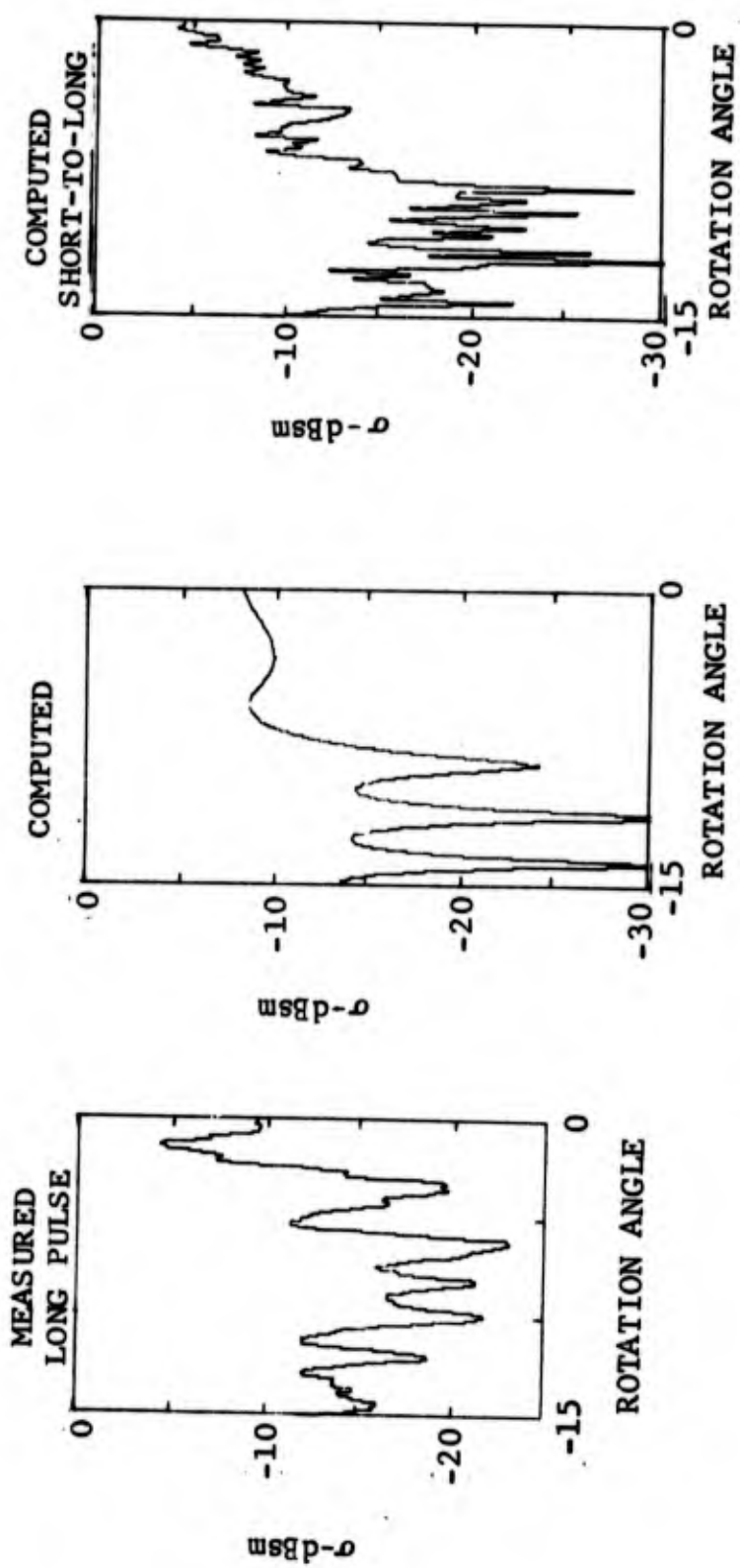


Fig. 3.2-12 DISCRETE SCATTERER MODEL VERIFICATION  
(V/V POLARIZATION, 20° PITCH, 0° ROLL, -15° TO 0°)

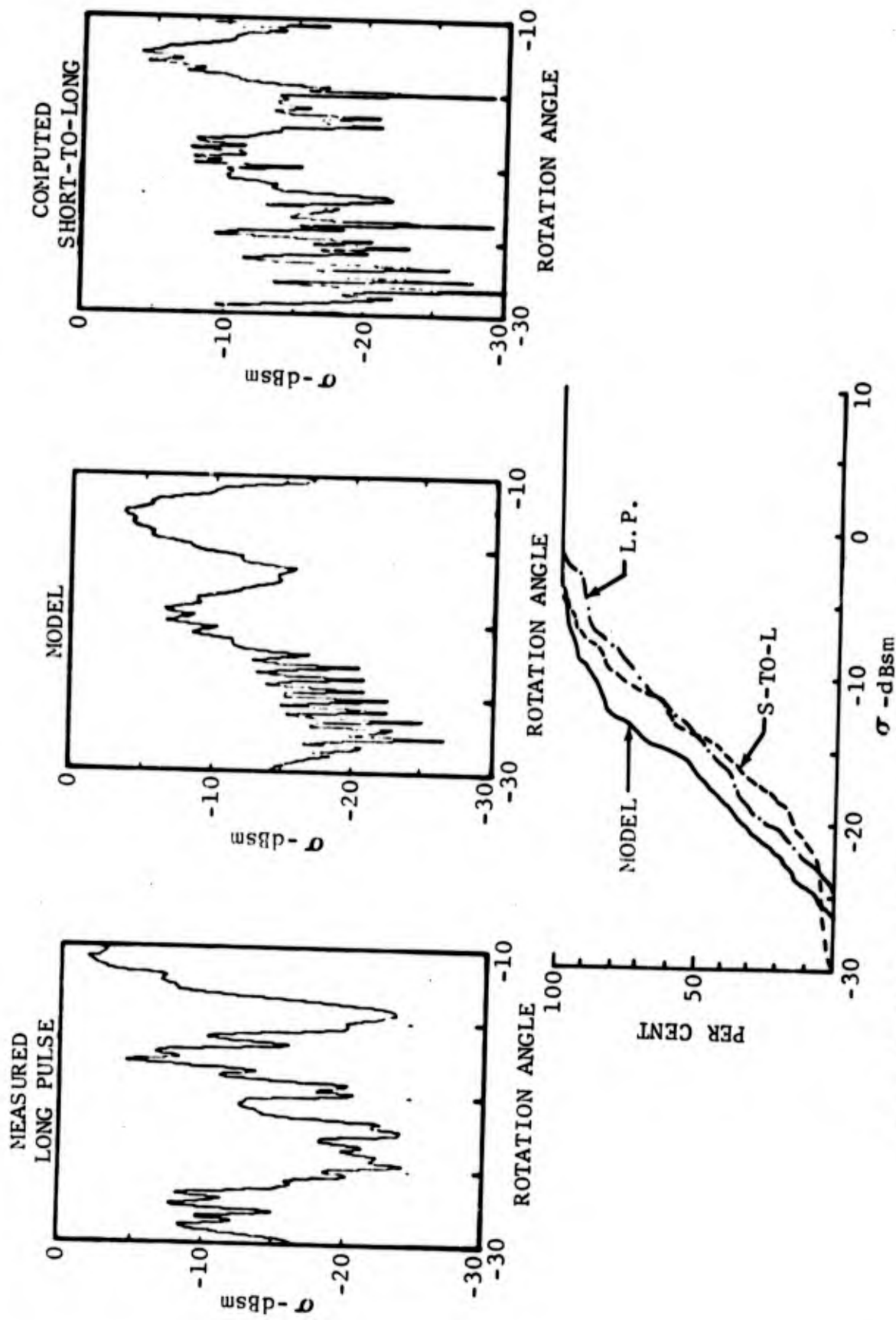


Fig. 3.2-13 DISCRETE SCATTERER MODEL VERIFICATION  
 (V/V POLARIZATION, 0° PITCH, -90° ROLL, -30° TO -10°)

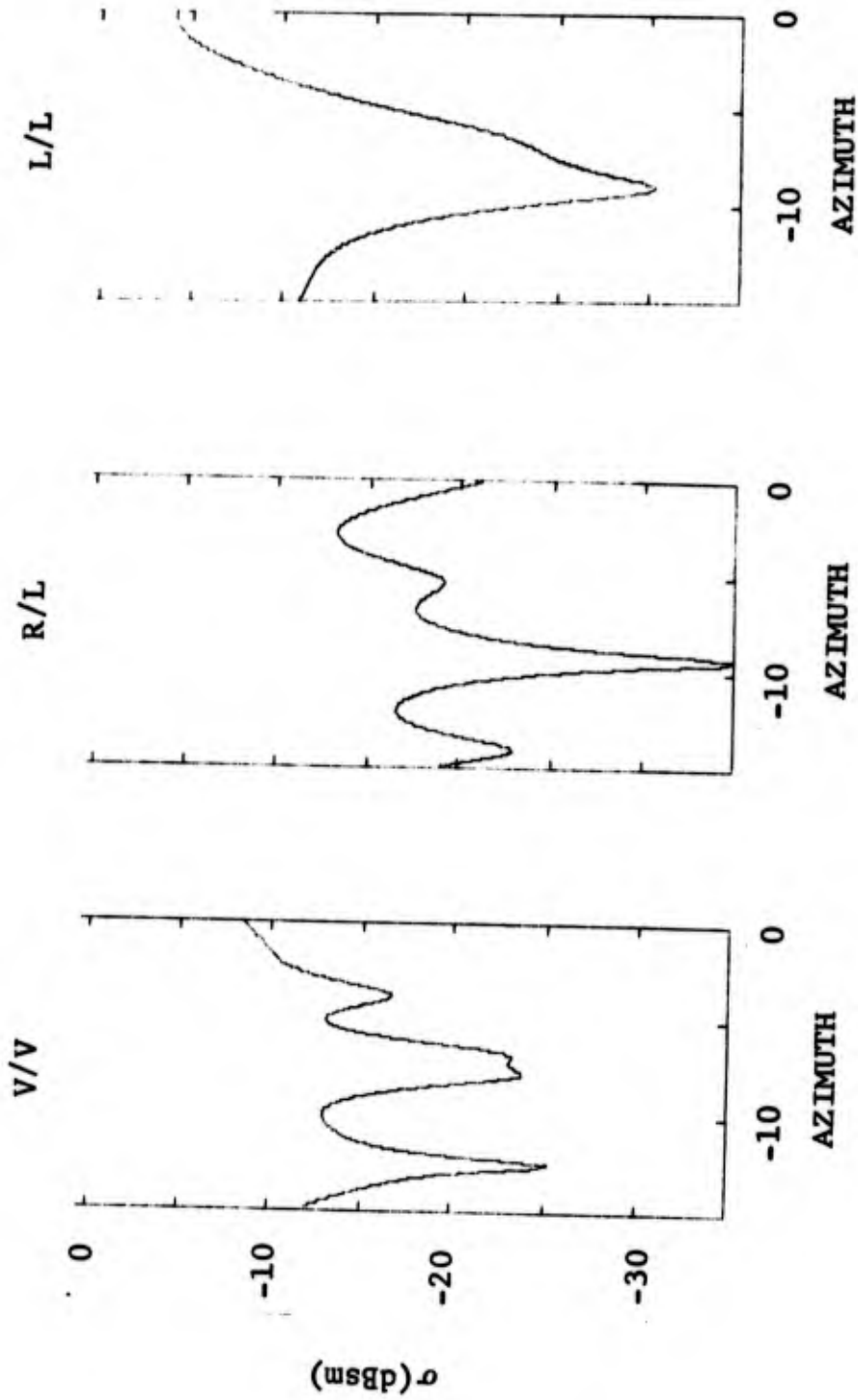


Fig. 3.2-14 RCS COMPUTED FROM DISCRETE SCATTERER MODEL  
( $0^\circ$  PITCH,  $0^\circ$  ROLL,  $-15^\circ$  TO  $0^\circ$ )

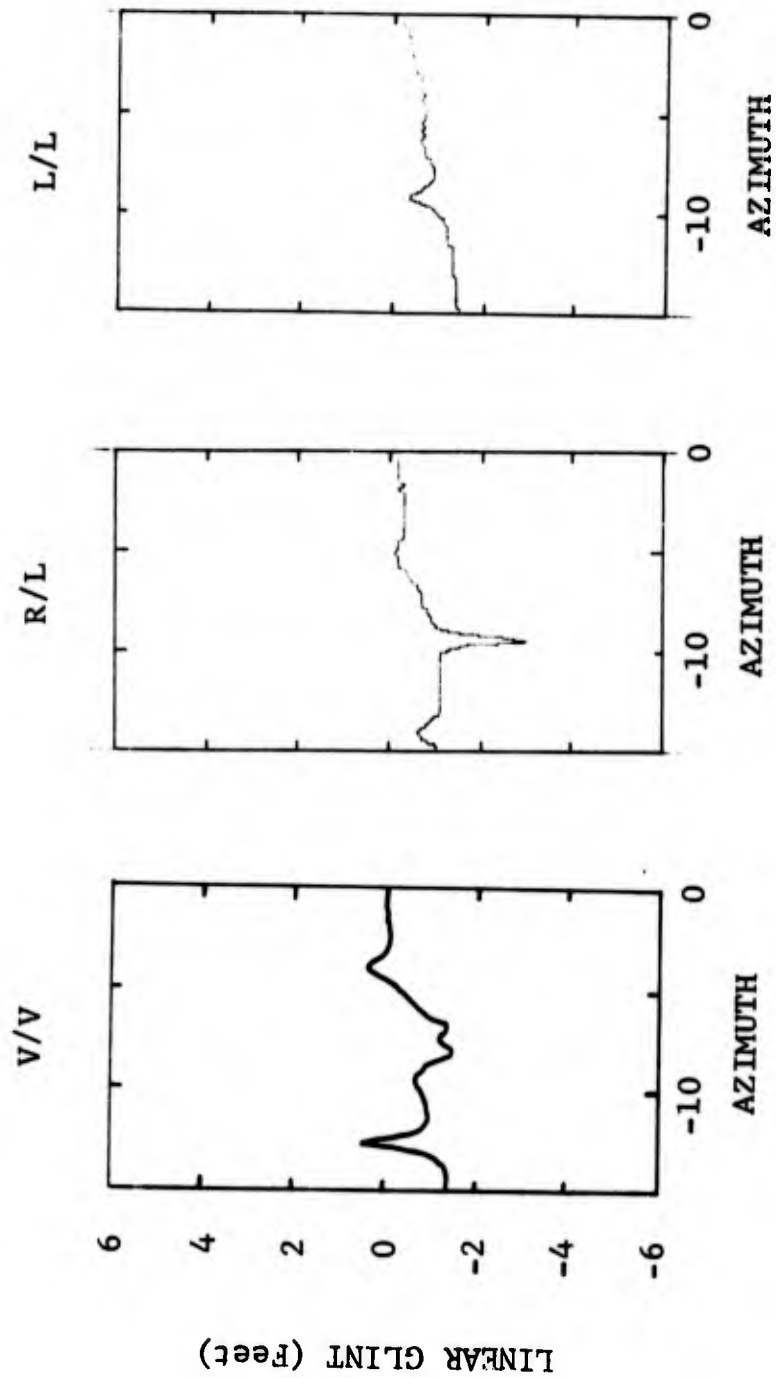


Fig. 3.2-15 GLINT COMPUTED FROM DISCRETE SCATTERER MODEL  
(0° PITCH, 0° ROLL, -15° TO 0°)

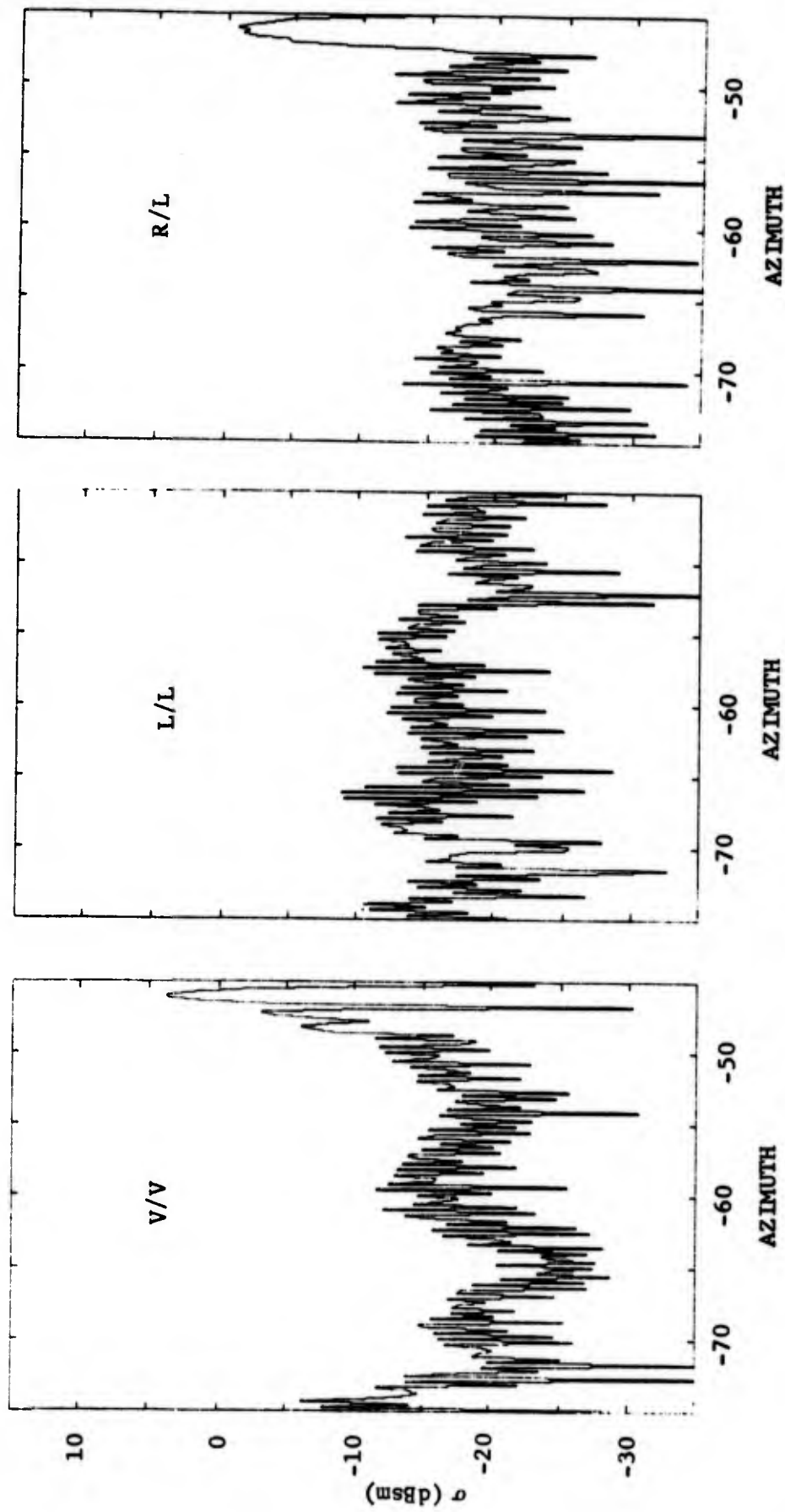


Fig. 3.2-16 RCS COMPUTED FROM DISCRETE SCATTERER MODEL  
(0° PITCH, 0° ROLL, -75° TO -45°)

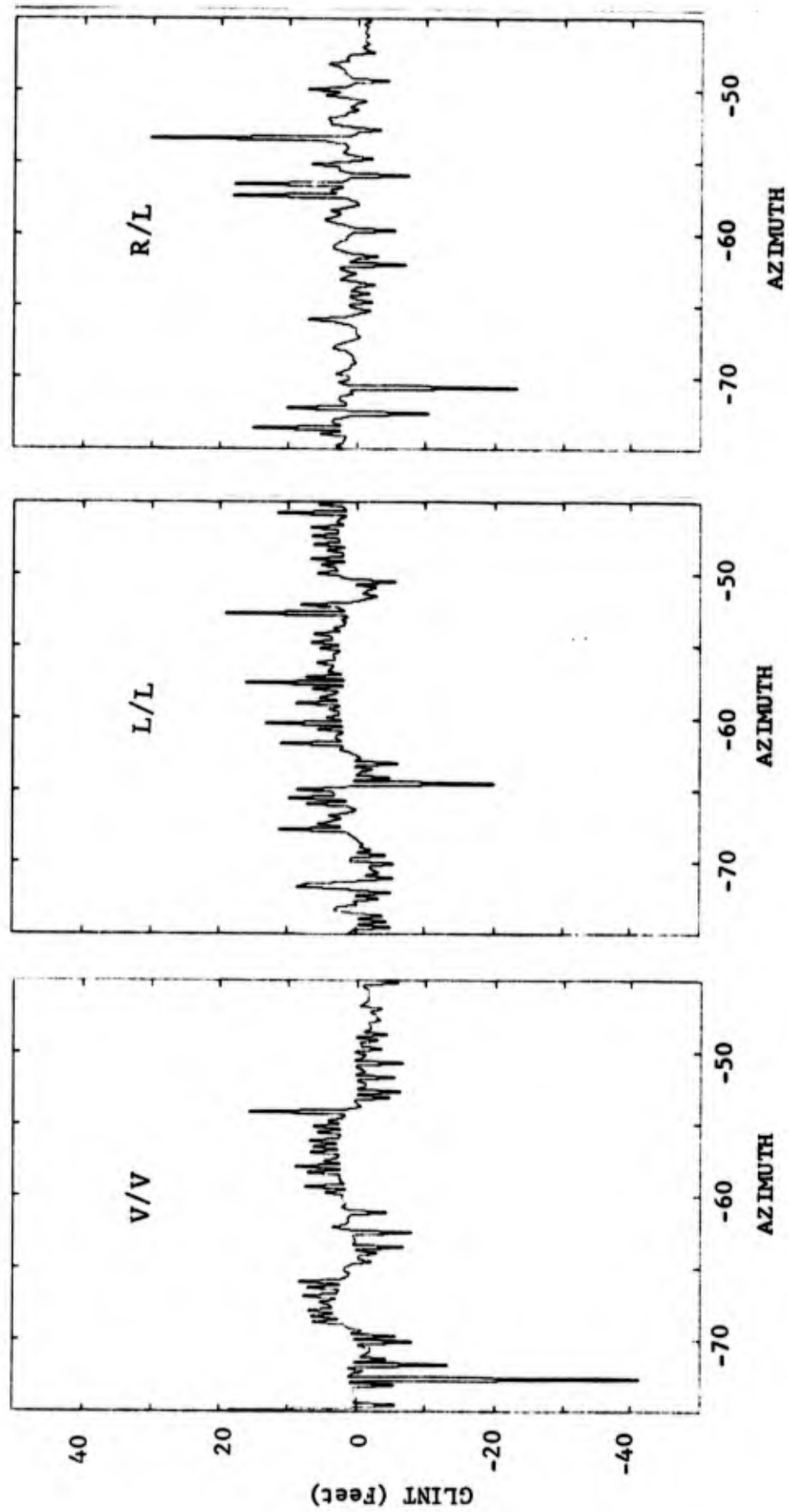


Fig. 3.2-17 GLINT COMPUTED FROM DISCRETE SCATTERER MODEL  
(0° PITCH, 0° ROLL, -75° TO -45°)

varying glint spikes shown in Figure 3.2-15. The glint within the angular sector from  $-45^{\circ}$  to  $-15^{\circ}$  is oscillating rapidly, and contains spikes which are more than twice the target length.

The RCS and glint obtained using circular and linear polarization are similar in structure when compared within the angular sectors shown in Figures 3.2-14 through 3.2-17. In the region about the nose ( $-15^{\circ}$  to  $0^{\circ}$ ), the RCS is generally higher in L/L polarization than in V/V or R/L polarization and the largest glint spike is approximately three feet. In the angular region centered about an azimuth angle of 60 degrees, the average RCS is largest in V/V polarization. Within this region, the largest glint spike is also in V/V polarization, but the difference in the standard deviation of the glint is less than one foot varying from a maximum of 5.3 feet in V/V polarization to 4.37 feet in L/L polarization.

SECTION 4  
PROCESSING AND  
COMPARISON OF ACTUAL  
VEHICLE MEASUREMENTS DATA

In addition to the measurements data available from the discrete scatterer modeling effort, the contractor was supplied, by the project monitor, with additional data obtained for the case of an actual BQM-34A drone vehicle. These data were measured at the Radar Target Scatter Site (RATSCAT) and include cross section, phase and linear glint for the case of the three principal polarizations. The data were supplied on magnetic tapes and was recorded at increments of 0.01 degrees. The original intent in supplying the contractor with these data was to provide additional results with which to compare the glint data computed using a discrete scatterer model. However, upon an examination of the RCS data, differences in the scale model measurements and the actual vehicle measurements were apparent.

These differences in the radar cross section are postulated to be basically due to perturbations and discontinuities in the target surface. Whereas the scale model is representative of a drone which has not been flown, some of the surfaces of the actual vehicle were not smooth at the junctions. In addition to discontinuities in the vehicle surface at some of the junctions, some of the surfaces contained small indentations and small, fluctuating changes in curvature. Selected sectors of the actual vehicle measurements data were processed in order to determine the circular polarization loss and the relationship between the linear and circular polarization glint data.

4.1 COMPUTATION OF CIRCULAR POLARIZATION  
RESULTS

The measurements of the actual BQM-34A radar signature included the three principal linear polarizations. Although circular polarization measurements were not made, the monostatic circular polarization signatures can be computed from the measured linear polarization data using the polarization scattering matrix (Ruck, et. al., 1970). Since the target is essentially a perfect conductor for purposes of radar

measurements, and the measurements were essentially monostatic measurements, i.e., the bistatic angle was very small; the approximation was made that the V/H signature is equal to the H/V signature, where the first literal denotes the transmitter polarization and the second literal denotes the receiver polarization. This is the only approximation required to compute the circular polarization signatures provided the radar to target phase did not change as the antenna polarization was varied.

The form of the equations used in computing the circular polarization signatures is the following:

$$\sqrt{\sigma_{RR}} e^{j\phi_{RR}} = 0.5 * (S_{HH} - S_{VV}) + e^{j\pi/2} S_{VH} \quad (4-1)$$

$$\sqrt{\sigma_{RL}} e^{j\phi_{RL}} = 0.5 * (S_{HH} + S_{VV})$$

$$\sqrt{\sigma_{LL}} e^{j\phi_{LL}} = 0.5 * (S_{HH} - S_{VV}) + e^{-j\pi/2} S_{VH}$$

where  $\sigma$  is the radar cross section

$\phi$  is the associated phase

$$\text{and } S_{HH} = \sqrt{\sigma_{HH}} e^{j\phi_{HH}}$$

$$S_{VV} = \sqrt{\sigma_{VV}} e^{j\phi_{VV}}$$

$$S_{VH} = \sqrt{\sigma_{VH}} e^{j\phi_{VH}}$$

This form of the circular polarization signatures can be utilized to illustrate the use of R/R or L/L circular polarizations in all-weather radar systems in order to reduce the effects of rain clutter.

In the case of backscatter from rain, each raindrop can be considered to be a small dielectric sphere and is thus polarization insensitive, i.e.,

$$\sqrt{\sigma_{HH}} e^{j\theta_{HH}} = \sqrt{\sigma_{VV}} e^{j\theta_{VV}} \quad (4-2)$$

$$\sqrt{\sigma_{VH}} e^{j\theta_{VH}} = 0$$

thus

$$\sqrt{\sigma_{RR}} \approx 0 \quad \text{or} \quad \sqrt{\sigma_{LL}} \approx 0$$

Hence rain clutter can be significantly reduced by using circular polarization. However, the backscatter from a complex target such as an aircraft is polarization sensitive ( $\sigma_{HH} \neq \sigma_{VV}$ ,  $\sigma_{VH} \neq 0$ ) and thus will be characterized by a non-zero cross circular polarization backscatter. The penalty that is paid for utilizing circular polarization to enhance the target to rain clutter ratio is normally considered to be the ratio  $\sigma_{\text{circ}} / \sigma_{\text{linear}}$ . This ratio is defined as the circular polarization loss.

The importance of the motion of the apparent phase center of a radar target to the solution of the radar tracking problem has been described (Brockner, 1951). A measure of this motion in a direction perpendicular to the radar line of sight is denoted as linear glint. Glint equations have been derived for the case of targets consisting of several discrete point scatterers and a direct relationship between the magnitude of the glint spikes and minima in the target RCS has been derived analytically (Peters and Weimer, 1963) and verified experimentally (Pierson, 1969). An examination of additional RCS and glint measurements data will also confirm this relationship (Mensa, 1971). The circular polarization target signature described in terms of the scattering matrix can be described as an average of the linear polarization signatures; therefore, it can be postulated that the circular polarization glint will be smaller than the linear polarization glint.

## 4.2 CALCULATION OF GLINT FROM MEASURED PHASE DATA

### 4.2.1 Direct Computation

The linear glint can be determined using balance point equations where the target signature is represented as a summation of discrete point scatterers (Peters and Weimer,

1963) or as the derivative of the target phase with respect to rotation angle (Ross and Bechtel, 1968). For the case of experimental determination of target glint, the radar system can be utilized to measure the received phase and the glint can be obtained by using the differentiation process or the glint can be measured using two receiving antennas.

Since measured circular polarization glint data was not available, the circular polarization glint was determined from the circular polarization signatures computed using the scattering matrix. The equation used in determining the circular polarization glint is the following:

$$G = \frac{1}{2k} \frac{\Delta\theta}{\Lambda\theta} \quad (4-3)$$

where  $G$  is the linear glint

$k$  is the wave number ( $2\pi/\lambda$ )

$\Lambda\theta$  is the angular difference between adjacent sample points (.01 degrees)

$\Delta\theta$  is the difference in the phase between adjacent sample points

Selected results of glint computed from measured phase data are presented in Figures 4.1-1 to 4.1-3. Glint spikes which are approximately four times the target length are observed. The data shown in the figures are somewhat noise sensitive due to the differentiation process and the extremely small angular increments. However, the measured amplitude and phase data can be processed to reduce the phase noise.

#### 4.2.2 Data Processing (Filtering)

The glint data computed from the measured phase data are rather noisy due to the extremely high angular sampling rate and the sensitivity of the differentiation process to high frequency noise. The glint determined using the smallest angular increment (0.01 degrees) and a phase difference of one degree, is approximately 1.4 feet. Thus, a small phase error will result in a rather significant glint error. However, since the angular sampling rate is quite high, the

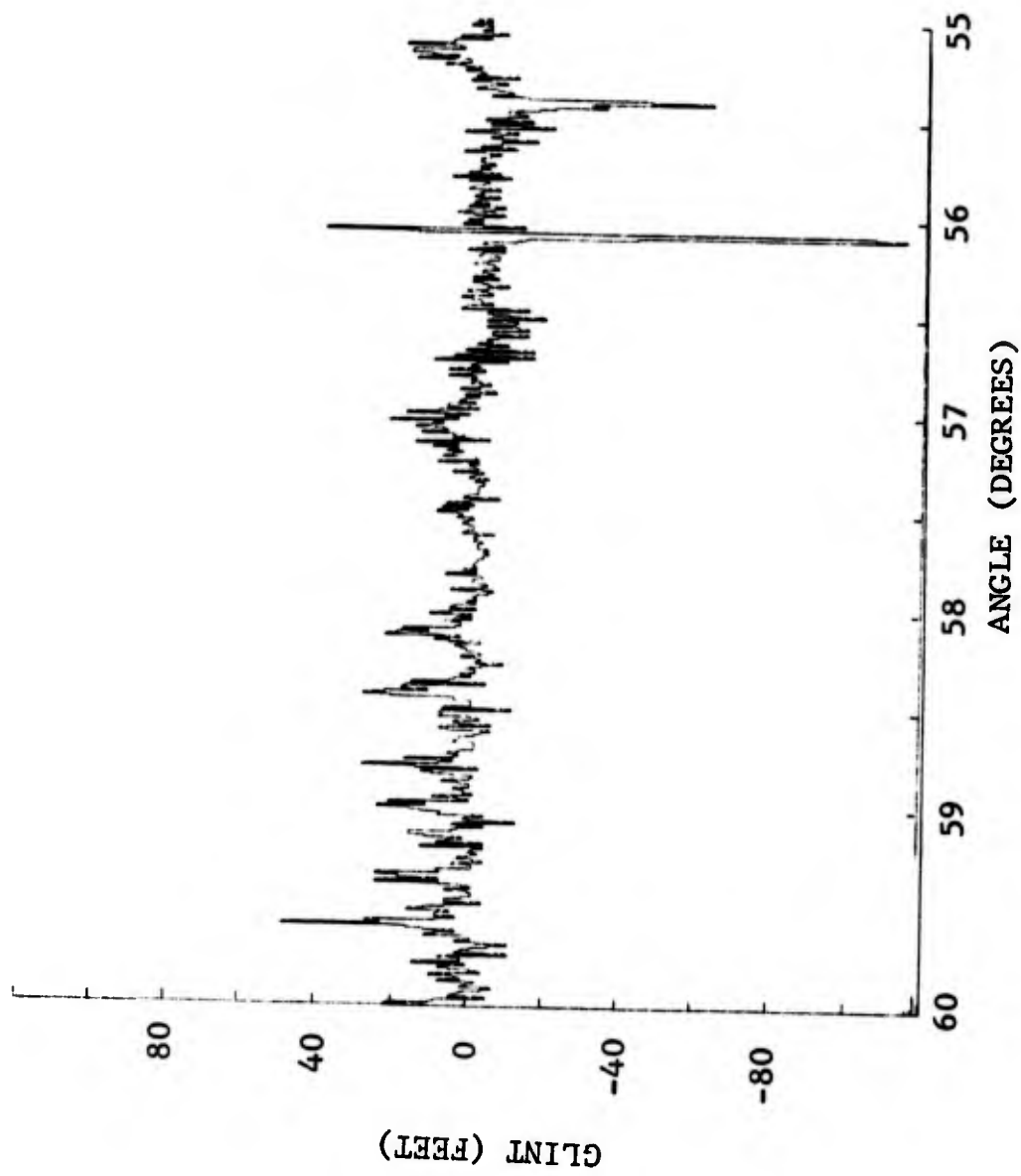


Fig. 4.2-1-1 GLINT DETERMINED FROM PHASE DATA  
(60° TO 55°)

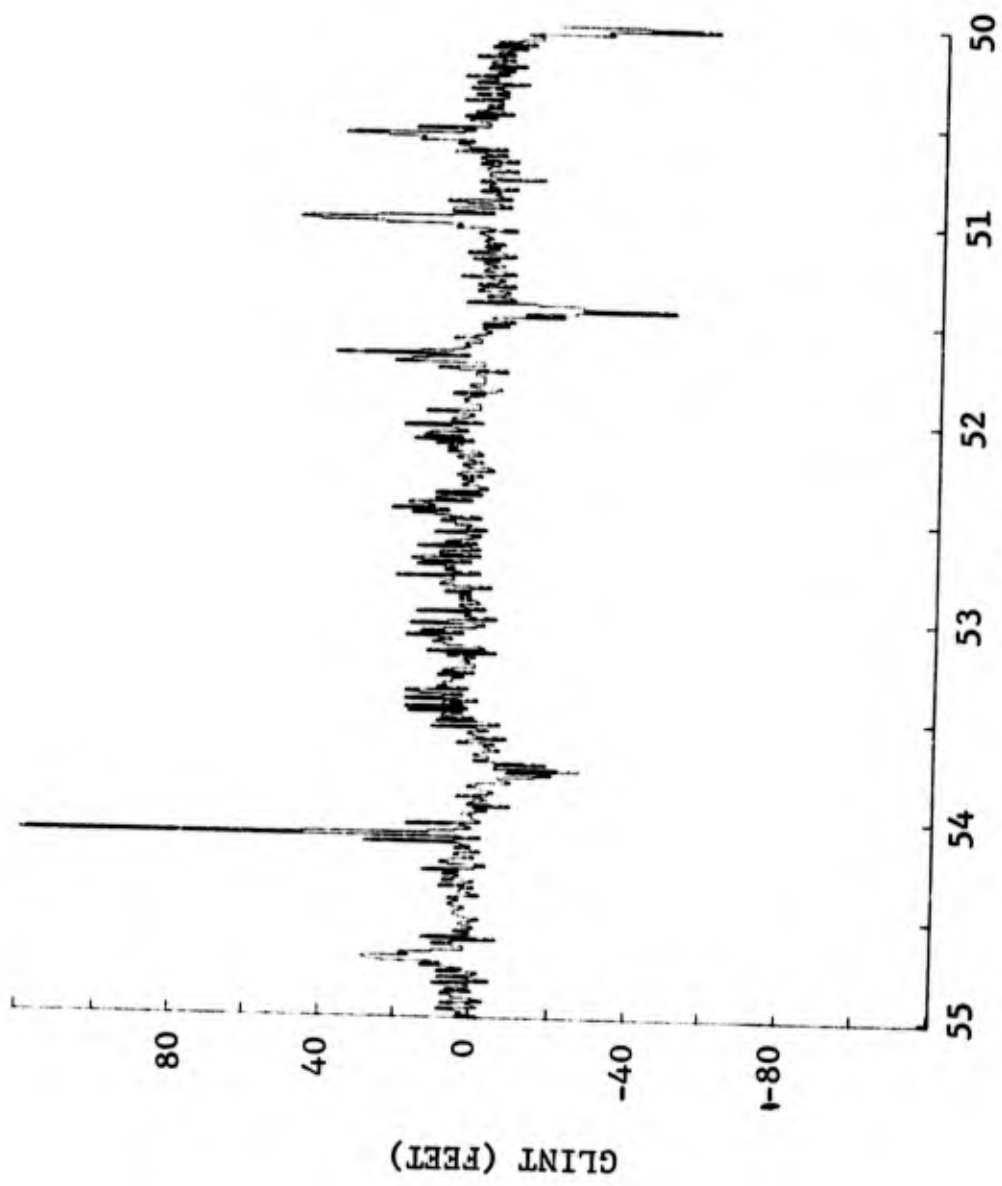


Fig. 4.2-2 GLINT DETERMINED FROM PHASE DATA  
(55° TO 50°)

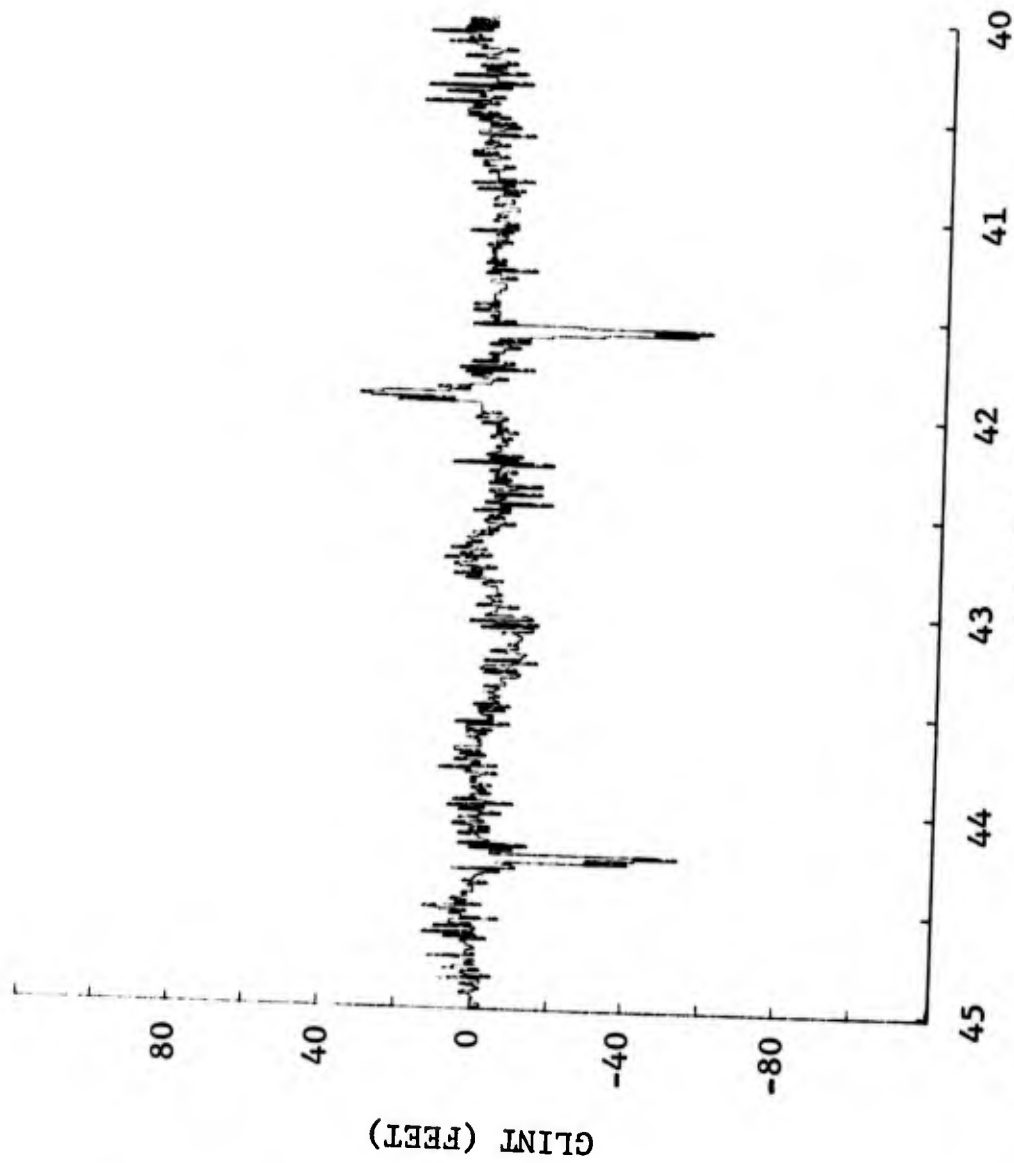


Fig. 4.2-3 GLINT DETERMINED FROM PHASE DATA  
(45° TO 40°)

amplitude and phase data can be processed to reduce the phase noise with little or no degradation in the resulting glint computation.

The data processing in order to reduce the phase noise involves removal of the high frequency components of the measured data. This process is easily implemented by transforming the data from an angle space to a cross-range or aperture space using the Fast Fourier Transform, filtering the result, and performing an inverse transform. The initial transformation is similar to synthetic aperture imaging and results in a measure of the cross-range position of the localized sources of the target scattered field. Although the energy from a specular return, such as the signal from the leading edge of the wing at an aspect of normal incidence to the wing will be distributed in cross-range, the amplitude of these returns should be insignificant at a position in cross-range which is more than twice the length of the target. The filtering is implemented by setting to zero all components of the transformed data which appear at a cross-range position which is approximately twice the entire target length. The filtered data are then inversely transformed in order to obtain the amplitude and phase data with the high frequency components removed.

The steps in the filtering process are illustrated mathematically in the following:

1. Transform Data to Cross-Range Space

$$T(y) = \frac{1}{2\theta_s} \int_{\theta_c - \theta_s}^{\theta_c + \theta_s} [\sqrt{\sigma} e^{j\theta}] e^{-j(2ky)\theta} d\theta \quad (4-4)$$

where  $y$  is the cross range position

$2\theta_s$  is the width of the angular data sector

$\theta_c$  is the center angle of the sector

2. Filter the data

$$F(y) = T(y) \text{ for } |y| < y_f \quad (4-5)$$

$$F(y) = 0 \quad \text{for} \quad |y| > y_f$$

where  $y_f$  is chosen to be approximately twice the target length

3. Inverse transform to obtain the smoothed amplitude and phase data

$$\sqrt{\sigma_f} e^{j\theta_f} = \int F(y) e^{j(2ky)\theta_d(2ky)} \quad (4-6)$$

The process was actually implemented using the FFT algorithm and an angular sector of 512 data points corresponding to 5.12 degrees. The transformed data then corresponded to a cross-range span of approximately 256 feet on either side of the center of rotation of the target. These data which exceeded a span of 50 feet (50 data samples) on either side of the zero cross-range position were set to zero. The remaining data were transformed using the inverse FFT algorithm. Because the two transformation process results in a periodic function, the first 6 and last 6 sample points were not included in the computation of the glint from the filtered phase data.

Selected glint data determined from the filtered amplitude and phase data are presented in Figures 4.2-4 through 4.2-6. Also included in the figures are plots of the amplitude of the transformed data in the cross-range or aperture space. The relative amplitude of these data is plotted on a linear scale, and the data which are set to zero are indicated. The resulting glint data can be compared to the data presented in Figures 4.2-1 through 4.2-3 where the glint was computed directly from the measured phase data. The basic shapes of the two sets of data are in good agreement, and the glint computed from the filtered phase data appears to be a smoothed version of the glint computed directly from the measured phase data.

#### 4.2.3 Comparison With Measured Glint Data

Although measured glint data were not available for the case of circular polarization, glint measurements were available for the case of the three principle linear polarizations.

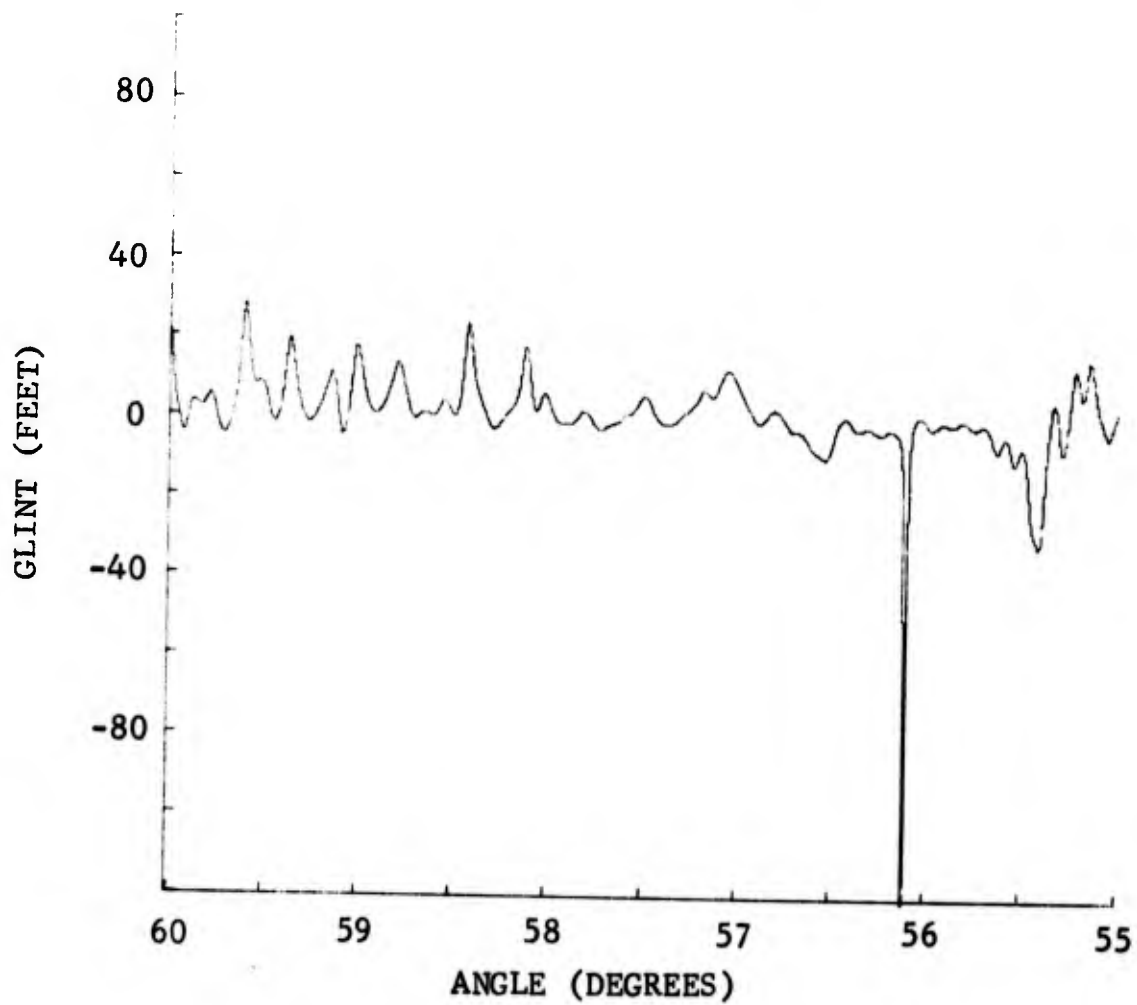
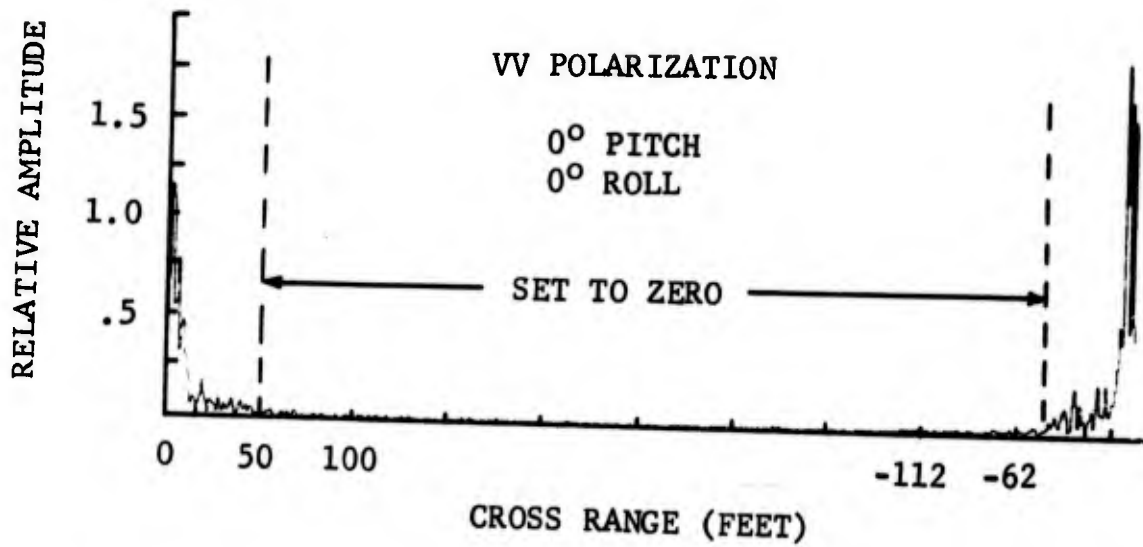


Fig. 4.2-4 GLINT COMPUTED FROM FILTERED PHASE  
 (60° TO 55°)

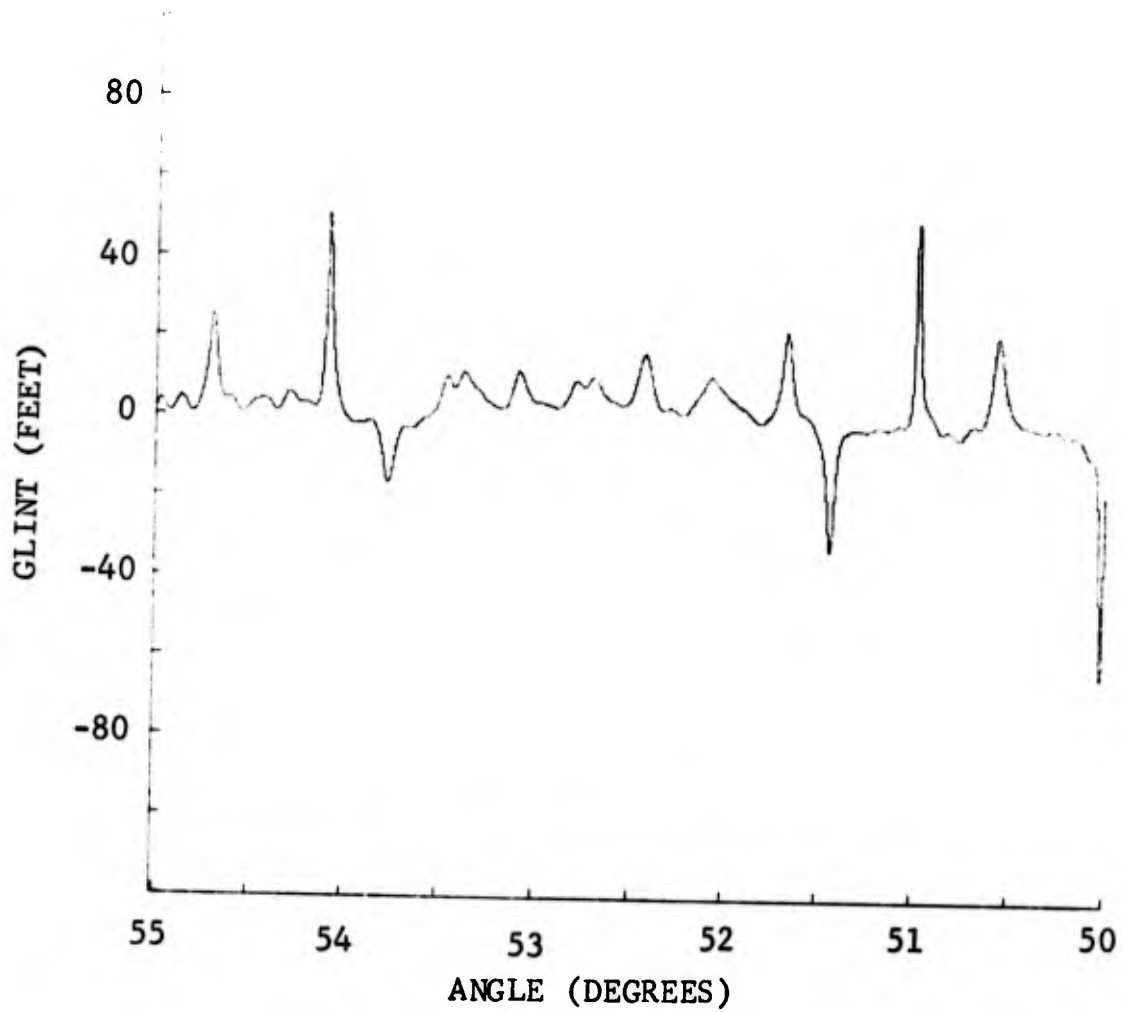
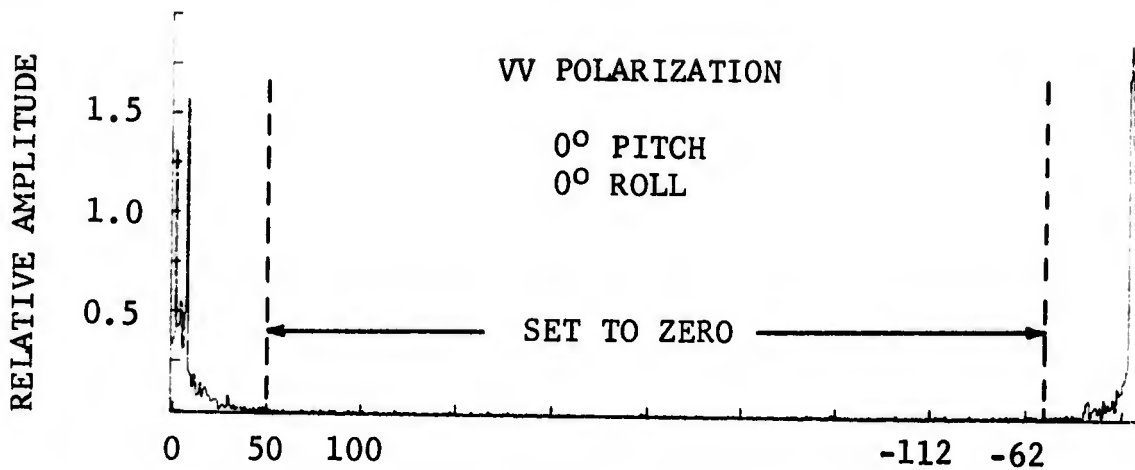
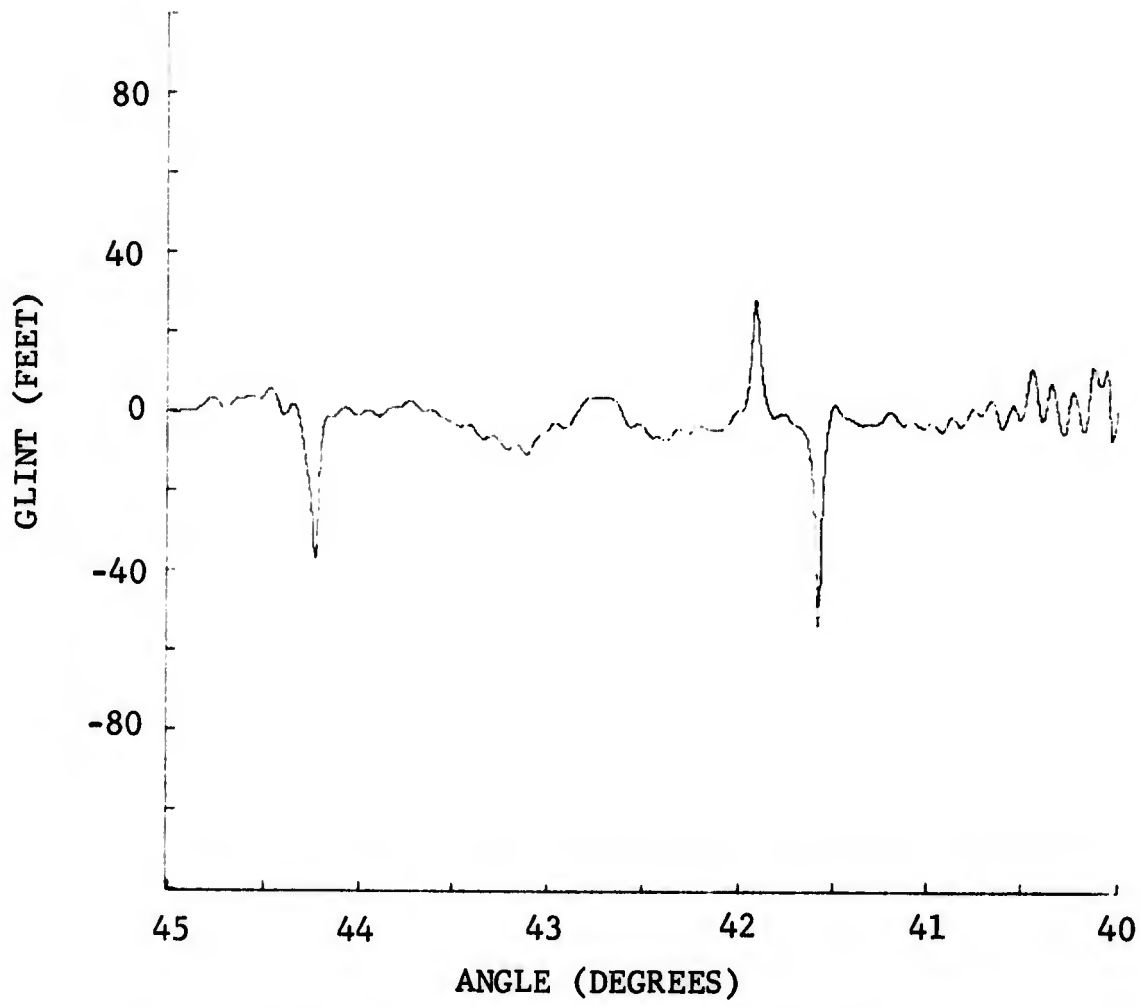
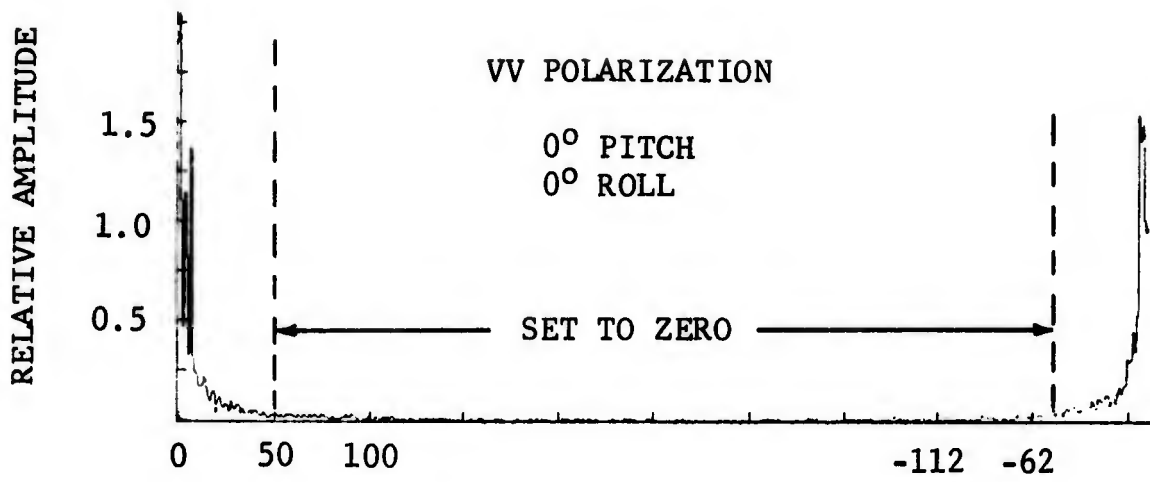


Fig. 4.2-5 GLINT COMPUTED FROM FILTERED PHASE  
(55° TO 50°)



4.2-6 GLINT COMPUTED FROM PHASE DATA  
(45° TO 40°)

Selected portions of these measurements data were compared to glint data computed both from the measured phase data and from the processed (filtered) phase data.

The measured glint data were obtained using two antennas, separated in space, to receive the target scattered field. The received signals are then processed to obtain a relative phase. The difference of the two phase signals can be calibrated in terms of the linear glint (Mensa, 1971). Since the maximum unambiguous phase difference is 180 degrees, the measured glint is limited to a value which corresponds to this phase difference. For the case of the BQM-34A glint measurements, the maximum glint value corresponded to 60 feet on either side of the center of rotation. This limit exceeds the maximum target displacement from the center of rotation by a factor of approximately five. However, due to the extremely high angular sampling rate, glint spikes are occasionally observed which exceed this value and are folded into the cross-range position on the opposite side of the target.

The measured data corresponding to the same angular sectors within which the glint was computed from the phase data are presented in Figures 4.2-7 through 4.2-9. The magnitude of the glint spike exceeded the range of the measurement system configuration in only one angular region at approximately 56 degrees.

The basic structure of the measured glint is in good agreement with either the glint computed from the measured phase or the glint computed from the processed phase data. However, due to the large number of small fluctuations in the glint computed directly from the measured phase data, the glint computed from the processed amplitude and phase data appears to be in better agreement with the measured glint.

The mean value and standard deviation of the glint data obtained within selected angular sectors were determined in order to compare numerically the three types of results. These data are presented in Table 4.2-1. It was expected that the mean values would be in generally good agreement in all cases and that the standard deviation of the glint computed directly from the phase data would be slightly higher than the values obtained using the other two methods. Although these expectations were correct in several cases, in particular, the selected VV polarization data; conclusive

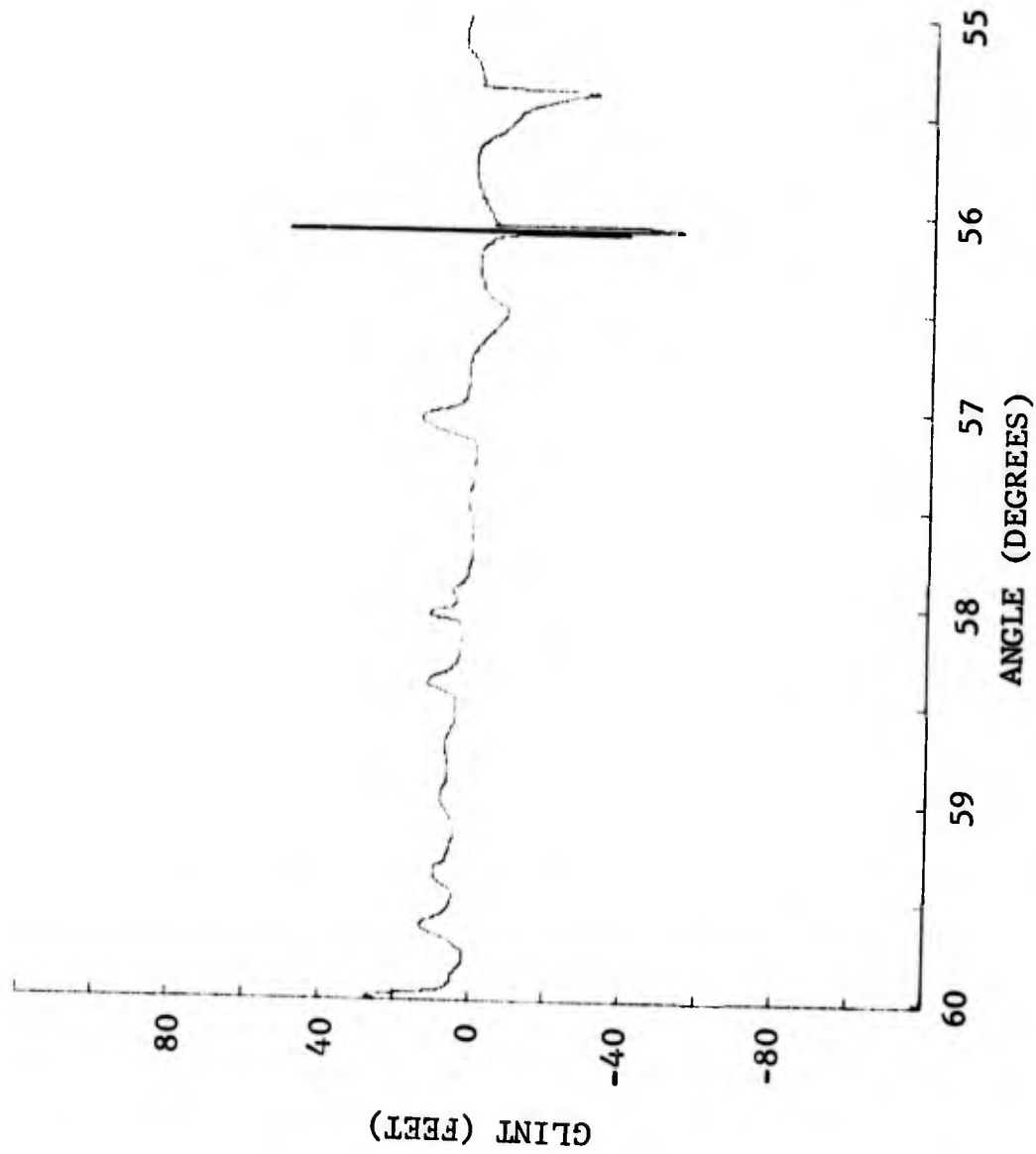


Fig. 4.2-7 MEASURED GLINT (60° TO 55°)

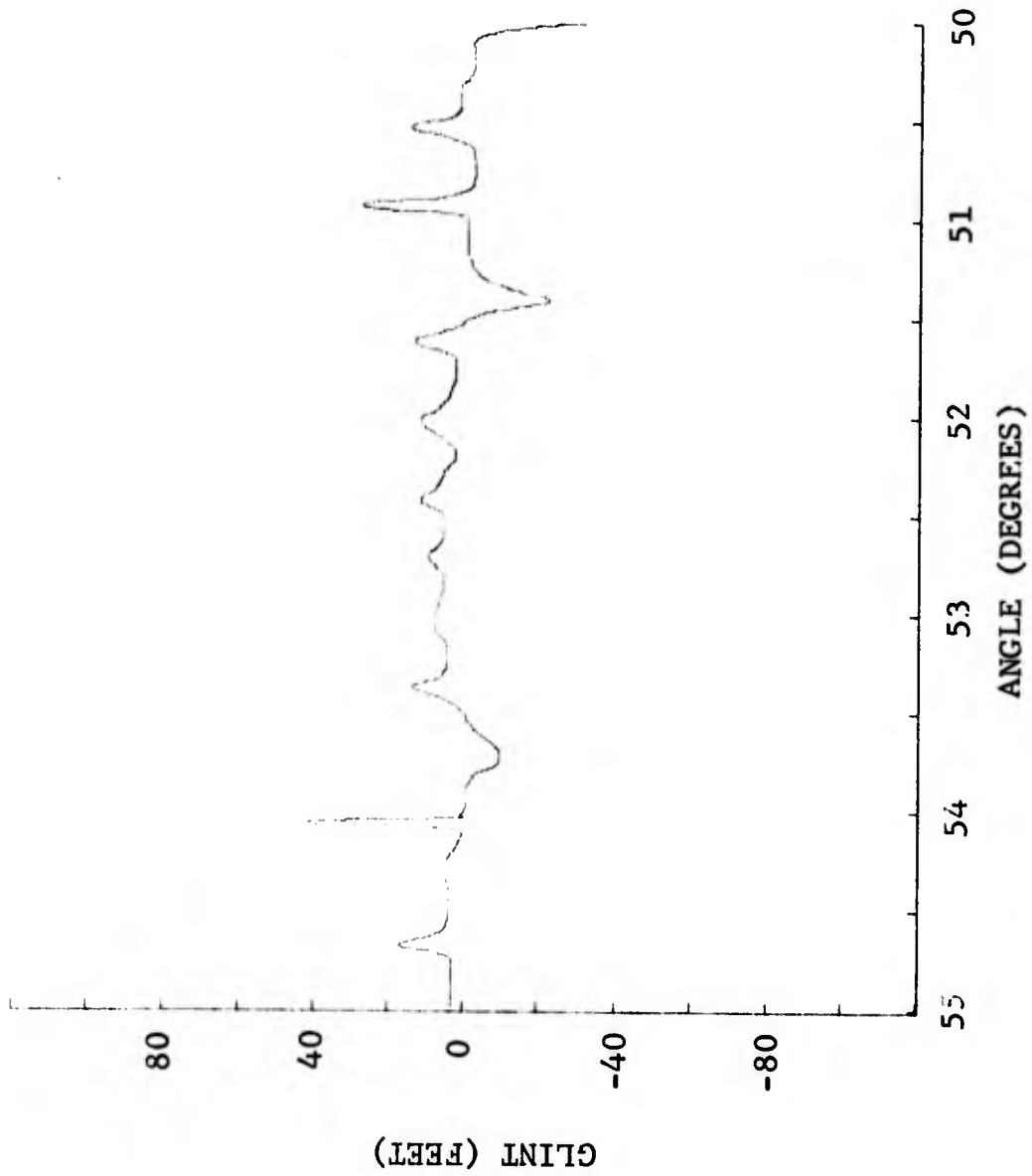


Fig. 4.2-8 MEASURED GLINT (55° TO 50°)

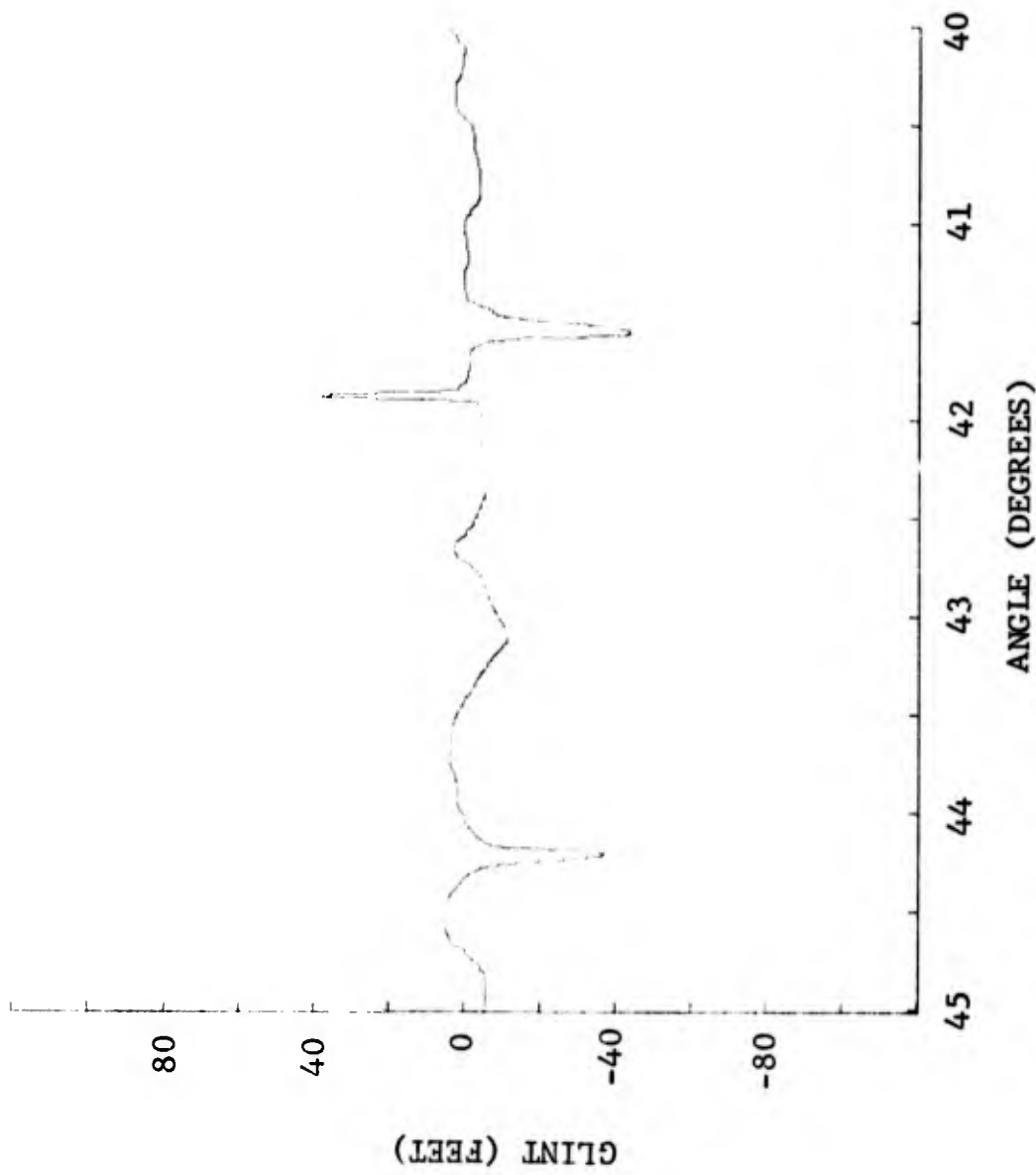


Fig. 4.2-9 MEASURED GLINT (45° TO 40°)

Table 4.2-1 COMPARISON OF MOMENTS OF MEASURED AND COMPUTED GLINT DATA

ANGULAR SECTOR	MEASURED		COMPUTED FROM MEASURED PHASE		COMPUTED FROM PROCESSED PHASE	
	MEAN	STANDARD DEVIATION	MEAN	STANDARD DEVIATION	MEAN	STANDARD DEVIATION
VV POLARIZATION						
60-55	3.96	6.48	2.26	11.56	2.28	9.86
55-50	4.31	6.49	3.52	11.29	3.53	9.00
45-40	-1.21	7.01	-.44	8.31	-.47	6.73
HH POLARIZATION						
55-50	1.77	12.75	-4.06	16.26	-4.06	12.73
50-45	5.32	9.61	2.13	10.85	2.18	8.71
45-40	-.53	9.01	-1.30	9.37	-1.34	7.71

results were not obtained. Perhaps the expected results would be achieved if a larger sampling of data were utilized and precautions were made to exclude from comparison all sectors in which the glint spikes exceeded the range of the measurement system configuration.

### 4.3 COMPARISON OF LINEAR AND CIRCULAR POLARIZATION RESULTS

The measured RCS and computed glint of the linear polarization data obtained for the case of the full scale vehicle are compared to the RCS and glint computed for the case of three circular polarizations. The glint data are obtained using (1) the data processing technique described in subsection 4.2.2 in order to reduce the phase noise and (2) the difference between two adjacent phase samples of the filtered data. Selected results are presented in Figures 4.3-1 through 4.3-5.

The lobing structure of typical RCS data can be compared for the case of three linear and three circular polarizations in Figure 4.3-1 and Figure 4.3-4 and the corresponding glint data can be compared in Figure 4.3-2 and Figure 4.3-5. The RCS data contain deep nulls for the case of all polarizations and the angular sector from 55 to 50 degrees; thus, the presence of rather large glint spikes could be predicted. Some of these glint spikes are greater than four times the largest physical target dimension.

The cumulative distributions of the RCS and glint data obtained from a uniform distribution of aspect angles within the angular region from 55 to 50 degrees are presented in Figure 4.3-3. For the case of this angular sector, the median values of the R/R and L/L polarization RCS are larger than the median of the H/H polarization RCS. The glint data are plotted to a scale which provides an indication of the magnitude of the tails of the probability distribution. For the case of all polarizations, these tails are pronounced.

The data shown in Figure 4.3-4 and Figure 4.3-5 were obtained within the angular region from 35 to 30 degrees. The structure of the RCS data contains fewer nulls and their depths are generally smaller than those shown in Figure 4.3-1; therefore, the glint spikes shown in Figure 4.3-5 are generally smaller than those shown in the preceding sector.

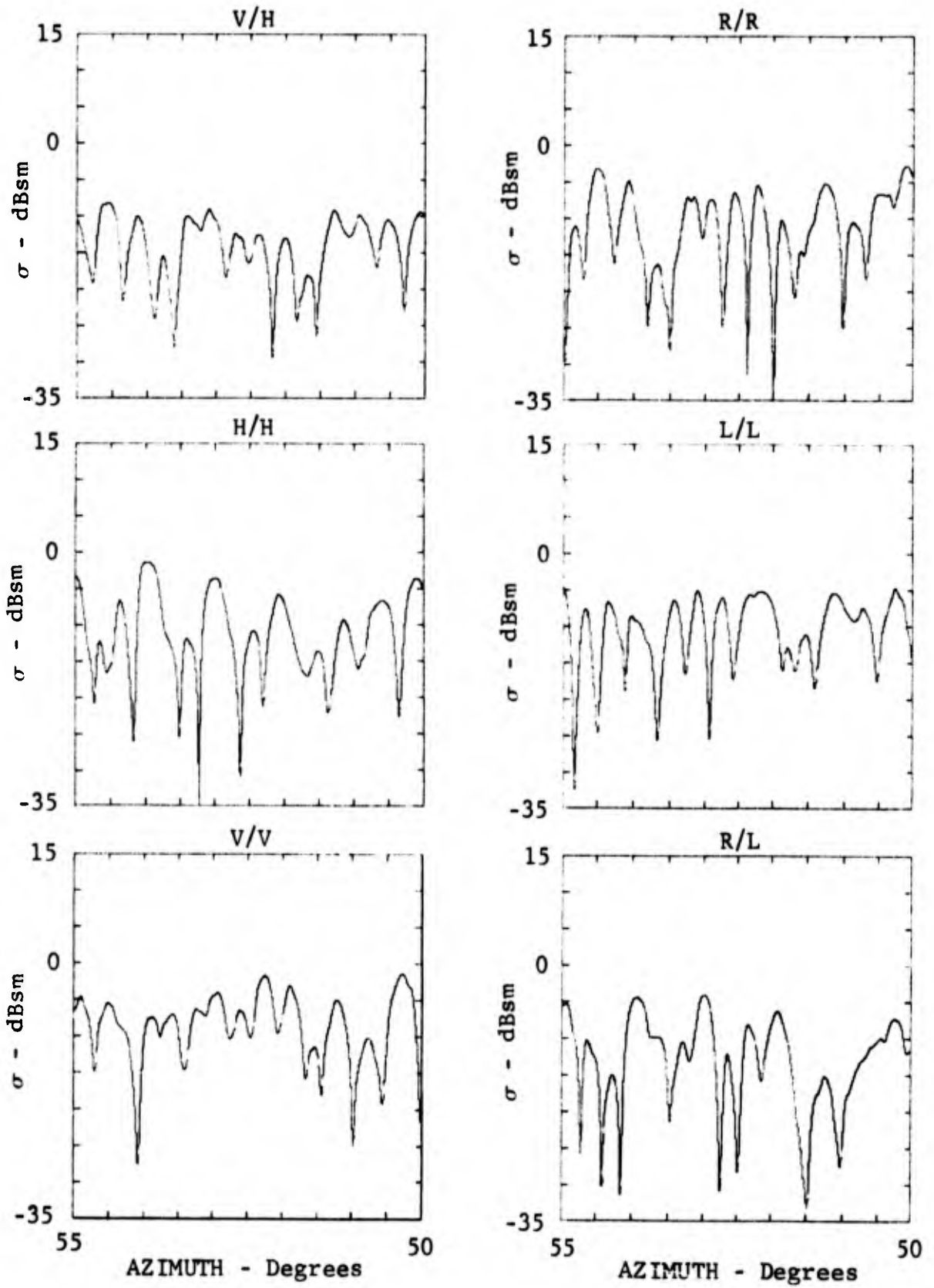


Fig. 4.3-1 RCS OF BQM-34A DRONE (55 to 50 Degrees)

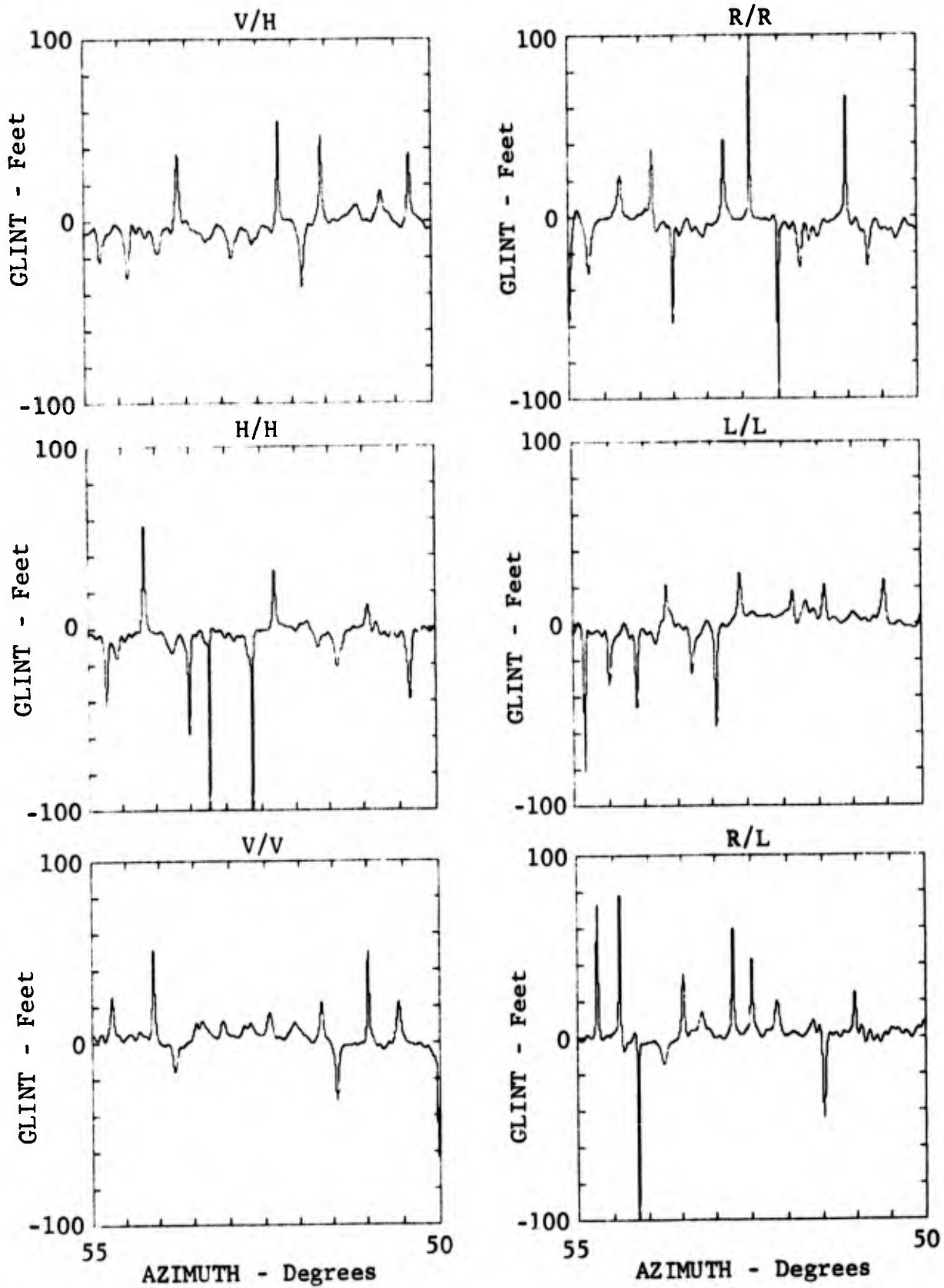


Fig. 4.3-2 GLINT OF BQM-34A DRONE (55 to 50 Degrees)

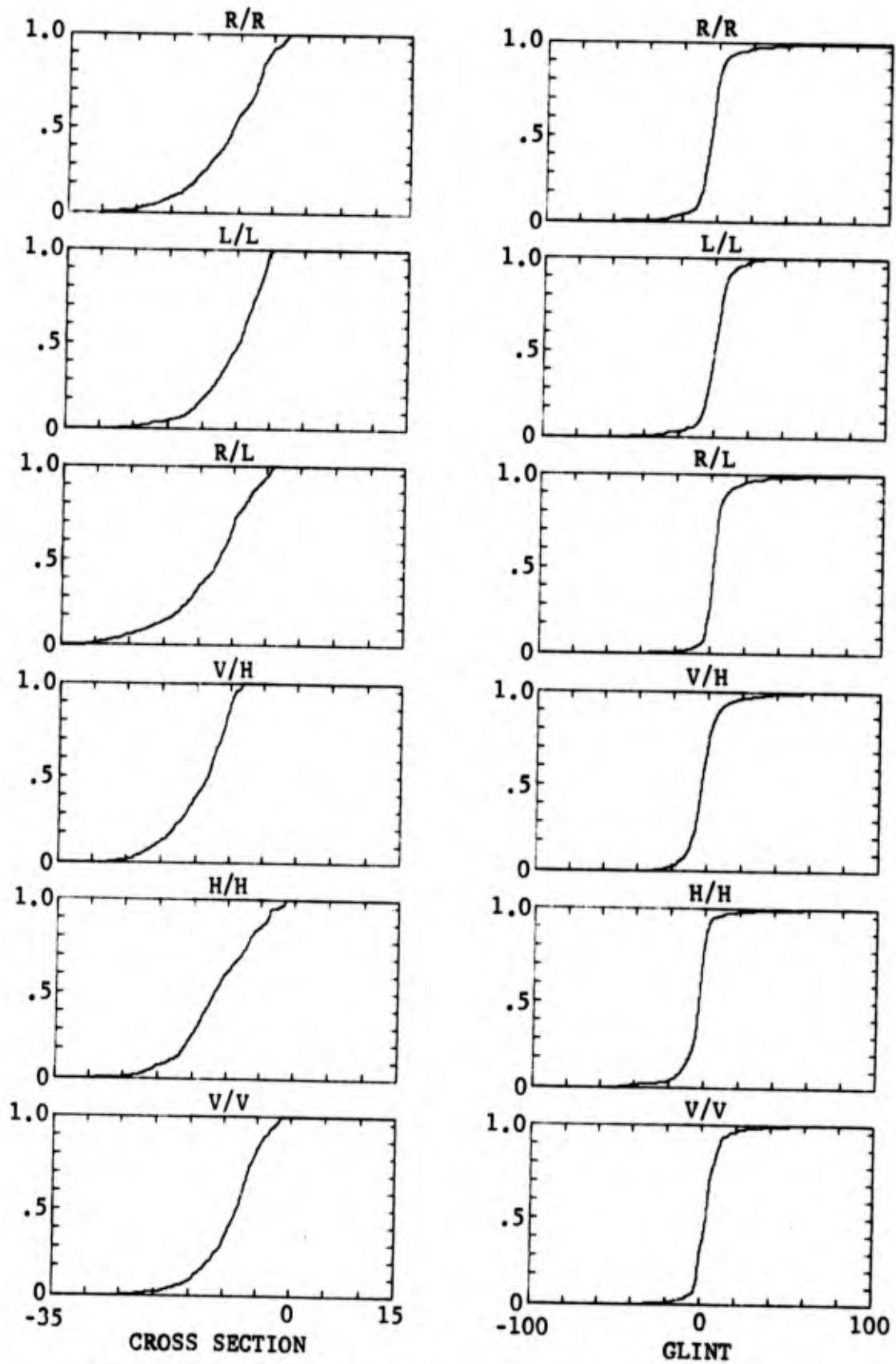


Fig. 4.3-3 CUMULATIVE DISTRIBUTION OF BQM-34A RCS AND GLINT (55 to 50 Degrees)

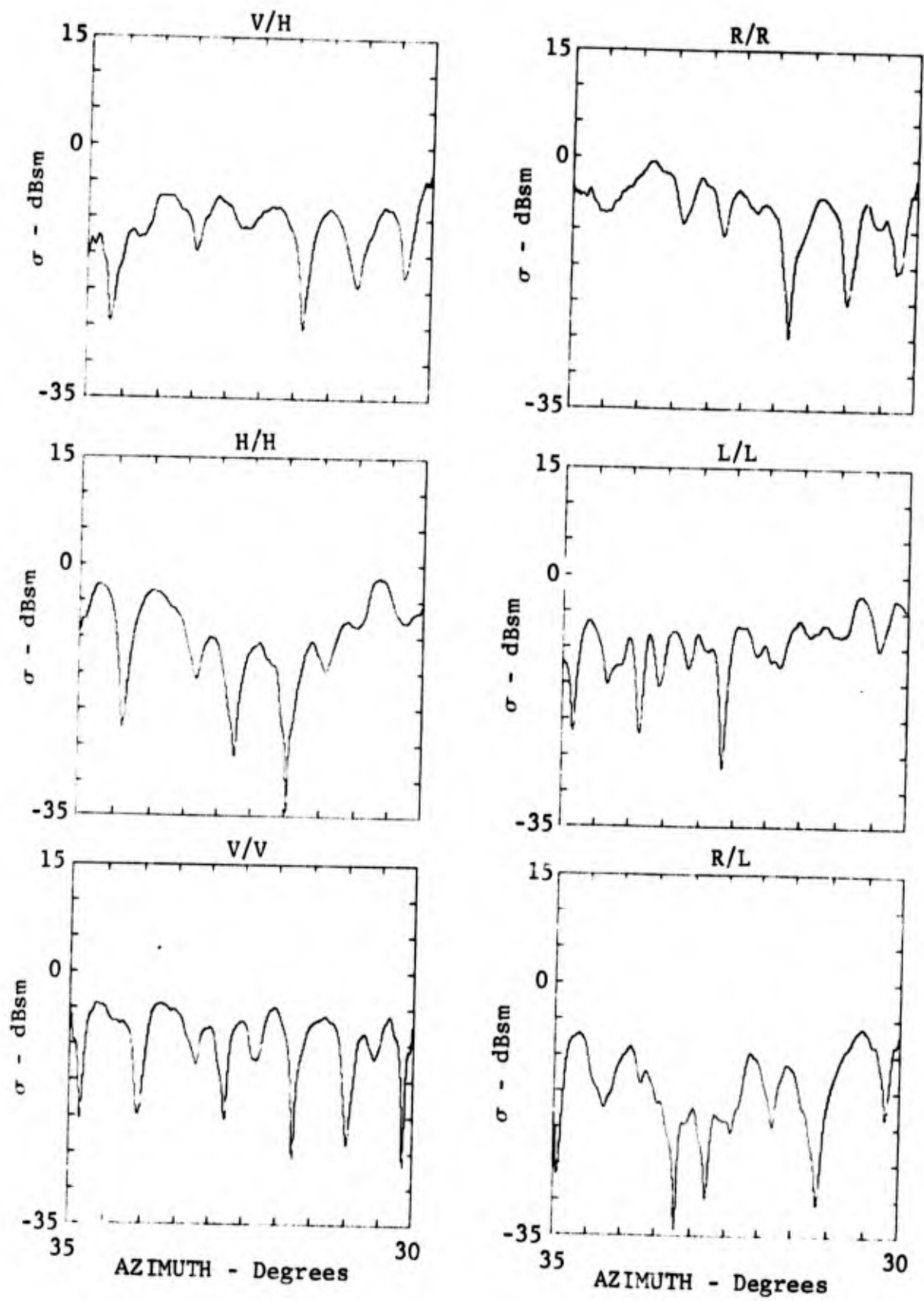


Fig. 4.3-4 RCS OF BQM-34A DRONE (35 to 30 Degrees)

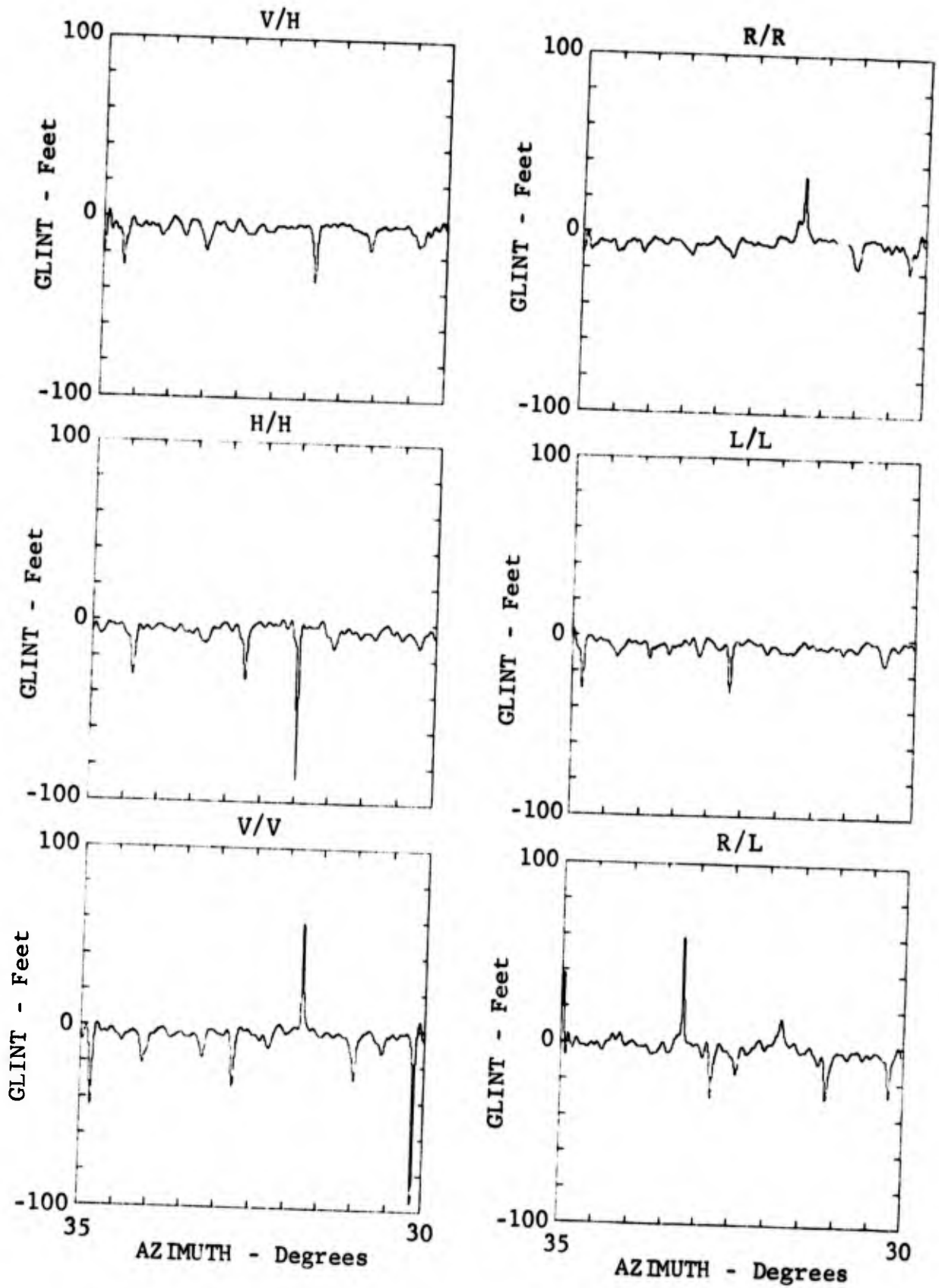


Fig. 4.3-5 GLINT OF BQM-34A DRONE (35 to 30 Degrees)

In examining the magnitude of the glint spikes and the standard deviation of the glint data obtained within small angular sectors, no conclusion could be drawn concerning the effects of polarization upon the magnitude of the glint data. It could be concluded that the magnitude of the glint spikes was highly dependent upon polarization as well as aspect angle. Results obtained for the case of 5 degree angular sectors each containing 500 data points are presented in Table 4.3-1 and Table 4.3-2.

Although the angular coverage of the data examined is limited to a region within 60 degrees of the nose and the horizontal plane of the target, two observations can be made concerning the polarization characteristics of the RCS and glint data. These observations involve the circular polarization loss and the effect of polarization on the magnitude of the glint data obtained from a complex target.

The circular polarization loss measured by the difference in the average value of the circular and linear polarized RCS is approximately 1 to 2 dB and varies from a loss to a gain depending upon the angular sector and the particular circular and linear polarization used in the comparison.

No significant trend was observed in comparing the polarization characteristics of the standard deviation of the glint data. Although the standard deviation of the glint was somewhat smaller for the case of linear polarization as compared to circular polarization, the differences in the average values of all the sectors are small and no trend was found to be consistent in the majority of the small angular sectors.

Although the results presented in Figures 4.3-1 through 4.3-5 and in Tables 4.3-1 and 4.3-2 are representative of circular polarization data obtained using the technique described in Section 4.1, the numerical results should be considered preliminary since it was determined, immediately prior to publication, that the relative phase measurements among the V/V, H/H, and V/H data were not recorded. Additional effort is required in order to verify that the relative phase is zero or to determine the constant phase correction terms required.

Table 4.3-1 MEAN VALUE OF SELECTED CROSS SECTION DATA

ANGULAR SECTOR	TRANSMIT/RECEIVE POLARIZATION							
	V/V	H/H	V/H	R/L	L/L	R/R	L/L	R/R
55-50	-6.93	-8.34	-12.65	-10.15	-8.81	-8.76	-8.81	-8.76
49-44	-3.56	-1.26	-10.18	-7.29	-2.95	-2.99	-2.95	-2.99
45-40	-6.16	-2.00	-9.40	-8.02	-3.15	-5.18	-3.15	-5.18
35-30	-7.99	-7.39	-10.03	-12.04	-8.18	-5.80	-8.18	-5.80
30-25	-10.00	-6.80	-11.55	-9.43	-9.40	-9.73	-9.40	-9.73
25-20	-8.32	-5.06	-10.94	-9.02	-5.58	-10.35	-5.58	-10.35
21-16	-2.85	-6.29	-5.00	-6.91	-.69	-9.00	-.69	-9.00
15-10	-2.74	-6.19	-7.28	-5.68	-5.22	-5.16	-5.22	-5.16
10-5	-1.63	-6.11	-14.02	-8.26	-3.18	-6.37	-3.18	-6.37
5-0	-5.64	-3.17	-18.01	-5.01	-13.25	-9.63	-13.25	-9.63
AVERAGE	-4.81	-4.65	-9.69	-7.74	-4.75	-6.64	-4.75	-6.64

(CROSS SECTION IN dBsm)

Table 4.3-2 STANDARD DEVIATION OF SELECTED GLINT DATA

ANGULAR SECTOR	TRANSMIT/RECEIVE POLARIZATION							
	V/V	H/H	V/H	R/L	L/L	R/R	L/L	R/R
55-50	9.00	12.72	10.19	11.31	10.23	13.35	10.23	13.35
49-44	6.75	6.00	4.26	6.26	14.68	10.26	14.68	10.26
45-40	6.72	7.71	7.20	11.85	7.93	9.47	7.93	9.47
35-30	8.71	6.30	4.60	7.58	3.82	4.94	3.82	4.94
30-25	8.07	5.25	5.69	8.68	5.00	6.74	5.00	6.74
25-20	8.36	3.72	5.11	4.22	5.66	6.52	5.66	6.52
21-16	4.89	3.44	2.43	10.16	1.49	8.26	1.49	8.26
15-10	3.50	2.00	2.66	2.29	7.93	2.57	7.93	2.57
10-5	1.54	4.83	4.44	2.62	1.33	5.14	1.33	5.14
5-0	2.12	1.73	2.27	1.35	12.61	4.31	12.61	4.31
AVERAGE	5.97	5.37	4.89	6.63	7.07	7.16	7.07	7.16

(STANDARD DEVIATION OF GLINT IN FEET)

SECTION 5  
CONCLUSIONS AND  
RECOMMENDATIONS

A large volume of measured signature data of the BQM-34A drone was processed and analyzed to determine the polarization dependence of the radar cross section and glint. Analyses of short-pulse and long-pulse measurements data and the data computed using the discrete scatterer model have resulted in the following observations and conclusions:

1. The results are highly dependent upon the angular sector or region of azimuth angles. By careful selection of an angular sector, the circular polarization loss can be made to vary from 17 dB to -6 dB.
2. In general, the CP loss is not as large as the often quoted figure of 6 dB and ranges from approximately 0 to 3 dB. For the case of the BQM-34A, the typical CP loss is 2 dB.
3. Although the position, magnitude, and number of the spikes of the BQM-34A glint signature are highly dependent upon polarization as well as azimuth, no significant differences were observed in the glint characteristics of the linear and circular polarized target signatures.

The BQM-34A is a single-inlet vehicle which is used extensively in radar system testing. However, within some angular regions, the scale-model vehicle cross section is extremely low and consists of the composite returns from a small number of discontinuities in the target surface. Since the characteristics of the inlet structure and vehicle shape of the BQM-34A are very different from those of a fighter aircraft, it is recommended that additional effort be directed toward the analysis of the polarization characteristics of a more complex aircraft target.

In comparing the cross section measurements data of the scale model and the actual vehicle, it was discovered that the scale model RCS reached extremely low levels within a large angular region. These extremely low-level returns were

not observed in the measurements data of the actual vehicle. It has been postulated that these differences are due to perturbations and discontinuities in the surface of the actual target vehicle. It is recommended that the scale-model BQM-34A be modified and selected additional measurements be made in order to verify this postulate.

## S E C T I O N 6

### R E F E R E N C E S

- Brockner, E. C. (1951), "Angular Jitter in Conventional Scanning Automatic Tracking Radar Systems," Proc. IRE, Vol. 39, pp. 51-56.
- Liang, C. S. and Clay, R. W. (1973), Improved Wideband Scattering Analysis, RADC-TR-73-11 (Rome Air Development Center, Rome, N.Y.)
- Mensa, D. L. (1971), Scintillation Characteristics of Aircraft Targets, TP-71-13, (Naval Missile Center, Point Mugu, California).
- Pierson, W. A. (1969), A Study of X-Band Glint from an Aircraft Target, Report No. DRL-TM-69-19 (Defense Research Laboratory, Austin, Texas).
- Pierson, W. A. , Liang, C. S., Clay, R. W., and Gruver, G. W. (1970), Short Pulse Scattering Measurements and Analysis (U), Vol. I (Confidential), RADC-TR-70-68-I (Rome Air Development Center, Rome, N.Y.)
- Pierson, W. A. and Clay, R. W. (1972), T-33 Radar Cross Section Measurements and Scintillation Analysis, RADC-TR-72-30 (Rome Air Development Center, Rome, N.Y.)
- Peters, L. and F. C. Weimer (1963), "Tracking Radars for Complex Targets", Proc. IEE, Vol. 110, No. 12, pp. 2149-2162.
- Ross, R. A. and C. C. Freeny (1964), An Analysis of the Scattering Matrix Measurement Capabilities of a Ground Plane Radar Cross Section Range, RADC-TDR-64-317, (Rome Air Development Center, Rome, N.Y.)
- Ross, R. A. and Marley E. Bechtel (1968), "Scattering-Center Theory and Radar Glint Analysis", IEEE Transactions on Aerospace and Electronic Systems, Vol. AES-4, No. 5, pp. 756-762.
- Ross, R. A. (1969), Investigation of Scattering Principles, Volume III-Analytical Investigation, RADC-TR-69-340, Vol. III (Rome Air Development Center, Rome, N.Y.)

Ruck, G. T., D. E. Barrick, W. D. Stuart, and C. K. Kirchbaum  
(1970), Radar Cross Section Handbook, (Plenum Press,  
New York).

Skolnik, Merrill I. (1962), Introduction to Radar Systems,  
(McGraw-Hill, San Francisco).

## A P P E N D I X A

### L O N G - P U L S E M E A S U R E M E N T S

#### D A T A

Long-pulse measurements of the 0.55 scale model BQM-34A drone were made during the Discrete Scatterer Target Modeling program for the Missile Systems Division of the Raytheon Company. Presented in this appendix are the raw measurements data obtained at X-band for the cases of V/V, L/L, R/L (transmit/receive) polarizations. Included is a brief description of the measurements system utilized in obtaining these data.

#### A.1 MEASUREMENTS SYSTEM DESCRIPTION

The X-band long-pulse measurement system is a pulsed system which is range-gated at the range of interest. This system provides the capability of recording amplitude and phase data over a 50-dB dynamic range.

The transmitter consists of a coherent source which contains two stages of traveling wave tube amplification. The unique receiving system accurately measures both the amplitude and the phase of the returned signal. A range-gated receiver gates the 60-megahertz IF amplifier in order to pass only the target echo. The IF amplifier is again gated at a time when no target is present, and a 60-megahertz pulsed coherent signal is injected through a linear variable attenuator and a variable phase shifter. The receiver processing circuitry is used to compare the amplitude and the phase of the target signal with the amplitude and the phase of the injected signal. If differences exist, servos drive the variable attenuator and variable phase shifter to force a correspondence in both the amplitude ( $\sigma$ ) and the phase ( $\phi$ ) of the two signals. The amplitude linearity of the system is 0.5 dB and its phase linearity is 2 degrees.

Frequency is controlled by locking the master oscillator and local oscillator to a frequency synthesizer to provide a short-term frequency stability of one part in  $10^9$ . Frequency, transmitter power, and pulse shape are monitored during measurements.

## A.2 MEASUREMENT TECHNIQUES

The long-pulse measurements acquired during this program were obtained in conjunction with a ground plane radar scattering facility with an 1800-foot measurement range. The ground plane technique is based upon the utilization of both the direct and the indirect (or ground reflected) waves to illuminate the target being measured. A previous investigation of the use of a ground plane range in making scattering matrix measurements (Ross and Freeny, 1964) culminated in a detailed explanation of the salient features of the ground plane concept, including the advantages and disadvantages of the technique.

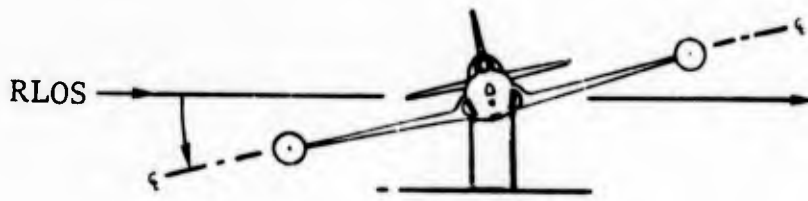
Amplitude calibration of the measured cross section data for the case of linear and similar sense circular polarizations was accomplished by the use of a precision sphere as a primary standard and a corner reflector which was located outside of the target range gate as a secondary standard. Calibration of cross circular polarization was based on the use of a dihedral corner reflector as a primary reference. The radar system was initially calibrated by placing the reference sphere or dihedral corner of known cross section on the target rotator and measuring the received power. The range gate was then moved to the vicinity of the secondary reference corner reflector and the signal from the corner was measured; its cross section was then calibrated in terms of the cross section of the primary reference. The secondary reference was subsequently measured before and after the measurement of each target so that system changes would be detected and corrected before the target was removed from the rotator.

## A.3 MEASUREMENTS DATA

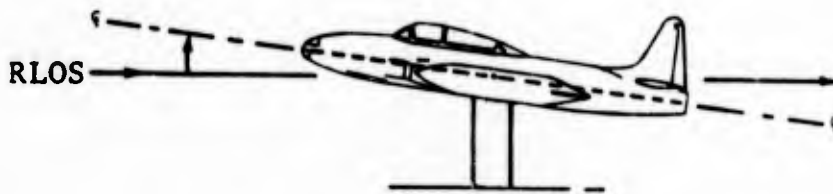
The following pages contain the analog plots of the cross section measurements data. These data correspond to a scale model BQM-34A drone and must be increased by a constant value in order to obtain equivalent results for the case of the actual vehicle. These data were obtained during continuous rotation of the target which was mounted with fixed pitch and roll angles. Table A-1 contains the matrix of target configurations. The pitch, roll, and rotations conventions are shown in Figure A-1 and the data are shown in Figures A-2 through A-34. All angles are referenced to the nose of the model. Digital data were recorded every 0.1 degree of azimuth rotation and are available in card-image format on 7-track magnetic tape.

Table A-1 LONG PULSE MEASUREMENT MATRIX  
(V/V, L/L, R/L POLARIZATIONS)

PITCH (Deg)	ROLL (Deg)	AZIMUTH SECTOR (Deg)
0	0	0-360
0	20	0-360
0	45	0-360
0	90	0-360
20	0	0-360
-20	0	0-360
45	0	0-360
-45	0	0-360
-15	-90	0-360
-30	-90	0-360
-45	-90	0-360



POSITIVE ROLL ANGLE



POSITIVE PITCH ANGLE



POSITIVE ROTATION ANGLE

Fig. A-1 TARGET ORIENTATION CONVENTIONS

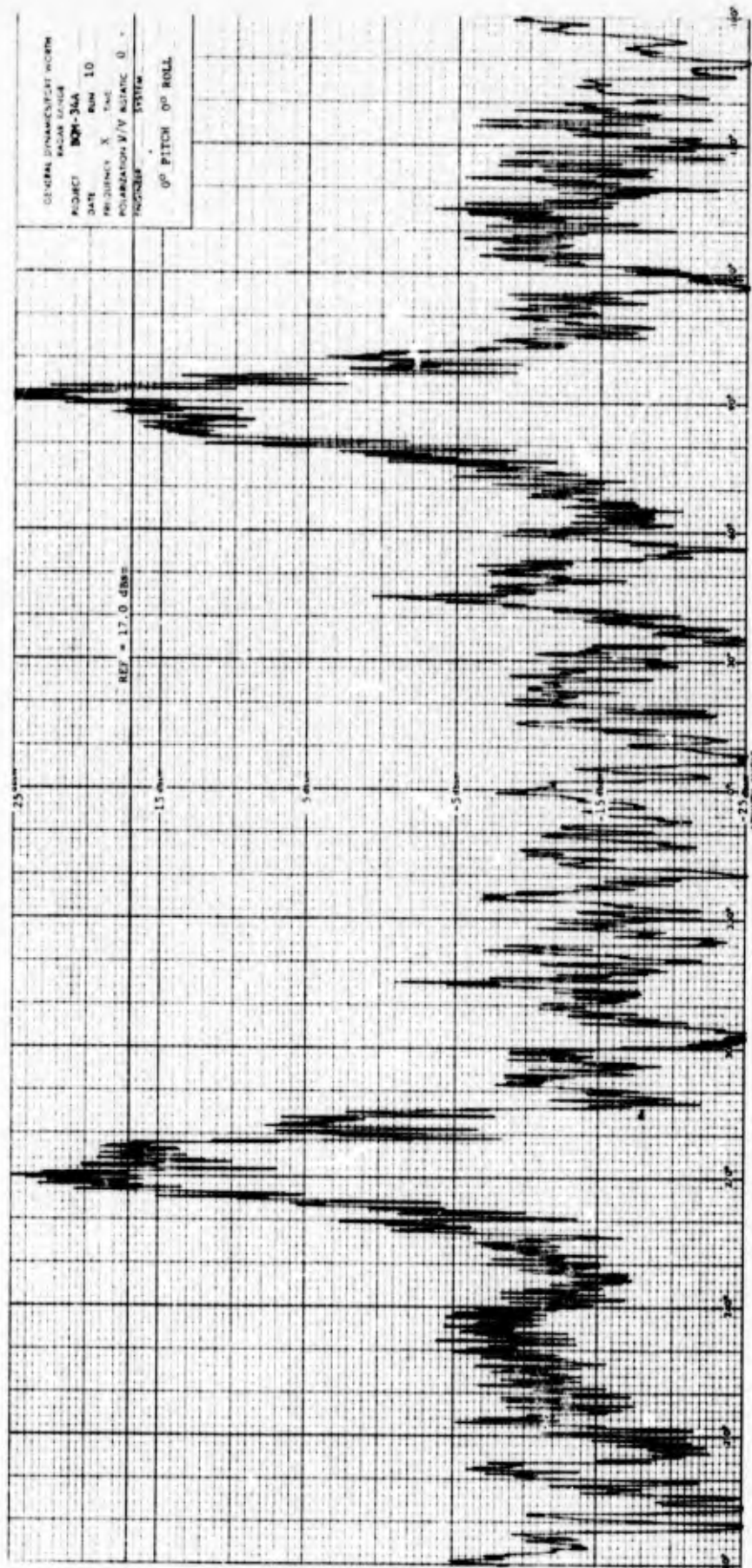


Fig. A-2 X-BAND RCS OF BQM-34A DRONE MODEL  
 (V/V POLARIZATION, 0° PITCH, 0° ROLL)

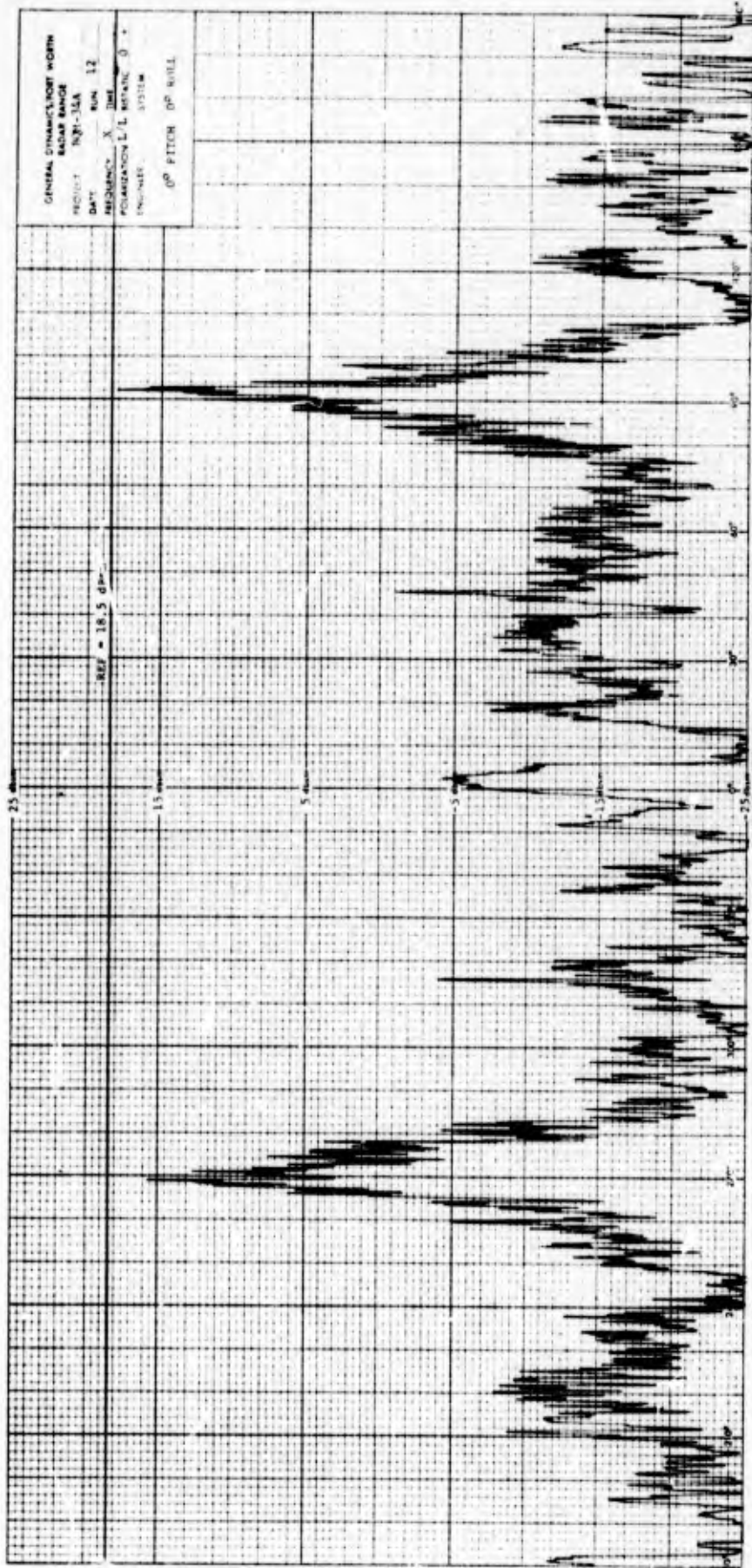


Fig. A-3 X-BAND RCS OF BQM-34A DRONE MODEL  
(L/L POLARIZATION, 0° PITCH, 0° ROLL)

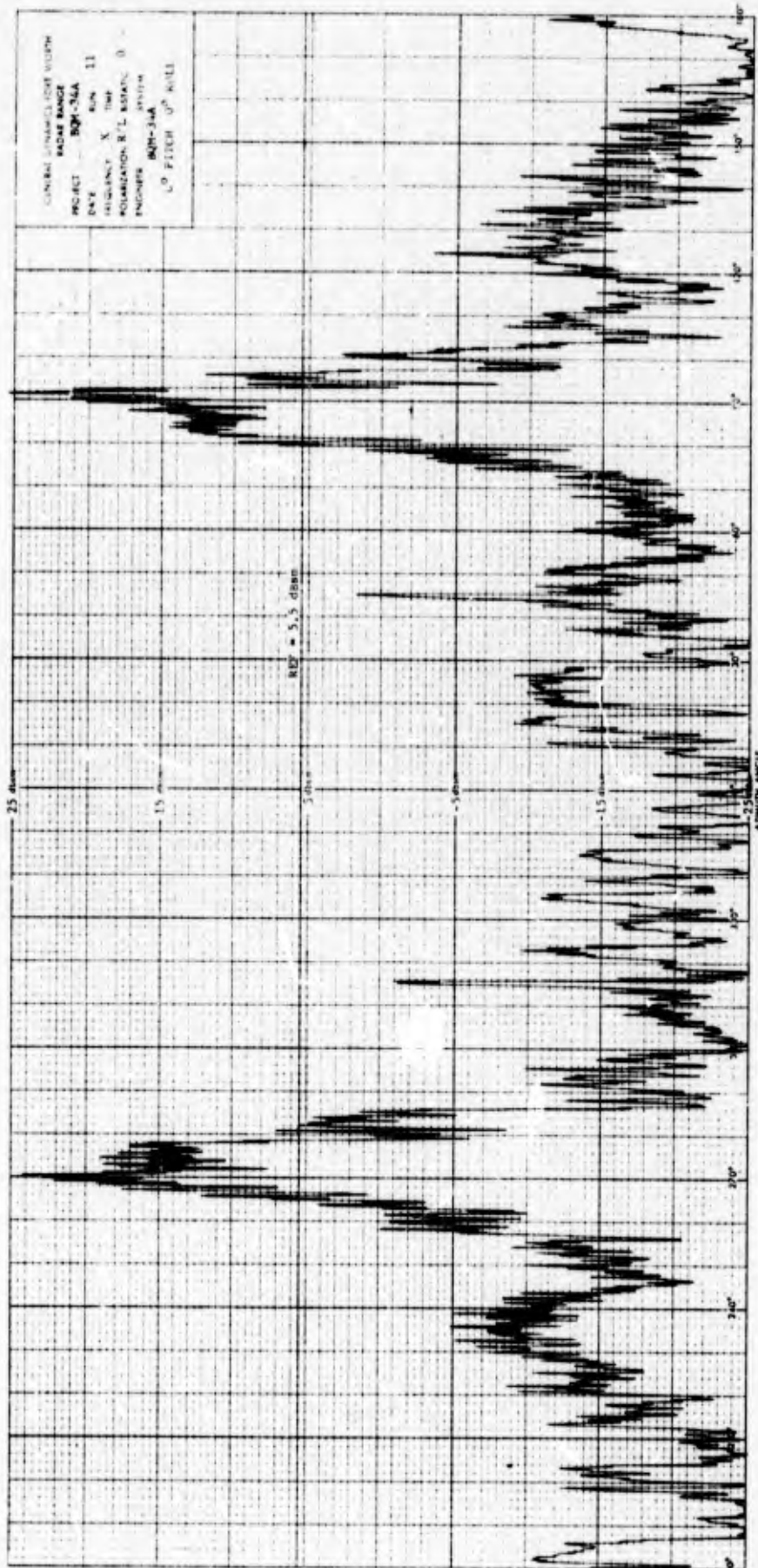


Fig. A-4 X-BAND RCS OF BQM-34A DRONE MODEL  
 (R/L POLARIZATION, 0° PITCH, 0° ROLL)

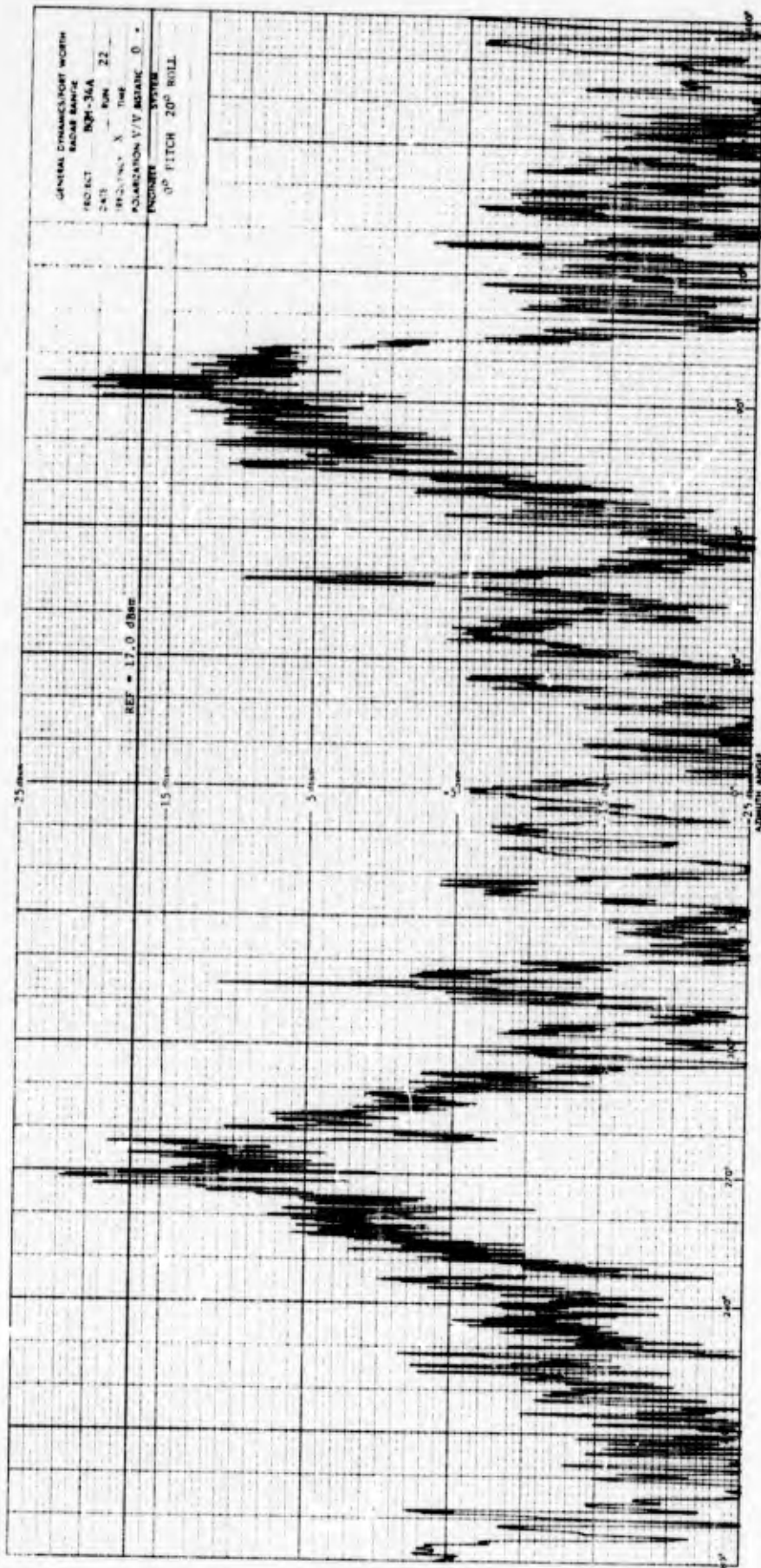


Fig. A-5 X-BAND RCS OF BQM-34A DRONE MODEL  
 (V/V POLARIZATION, 0° PITCH, 20° ROLL)

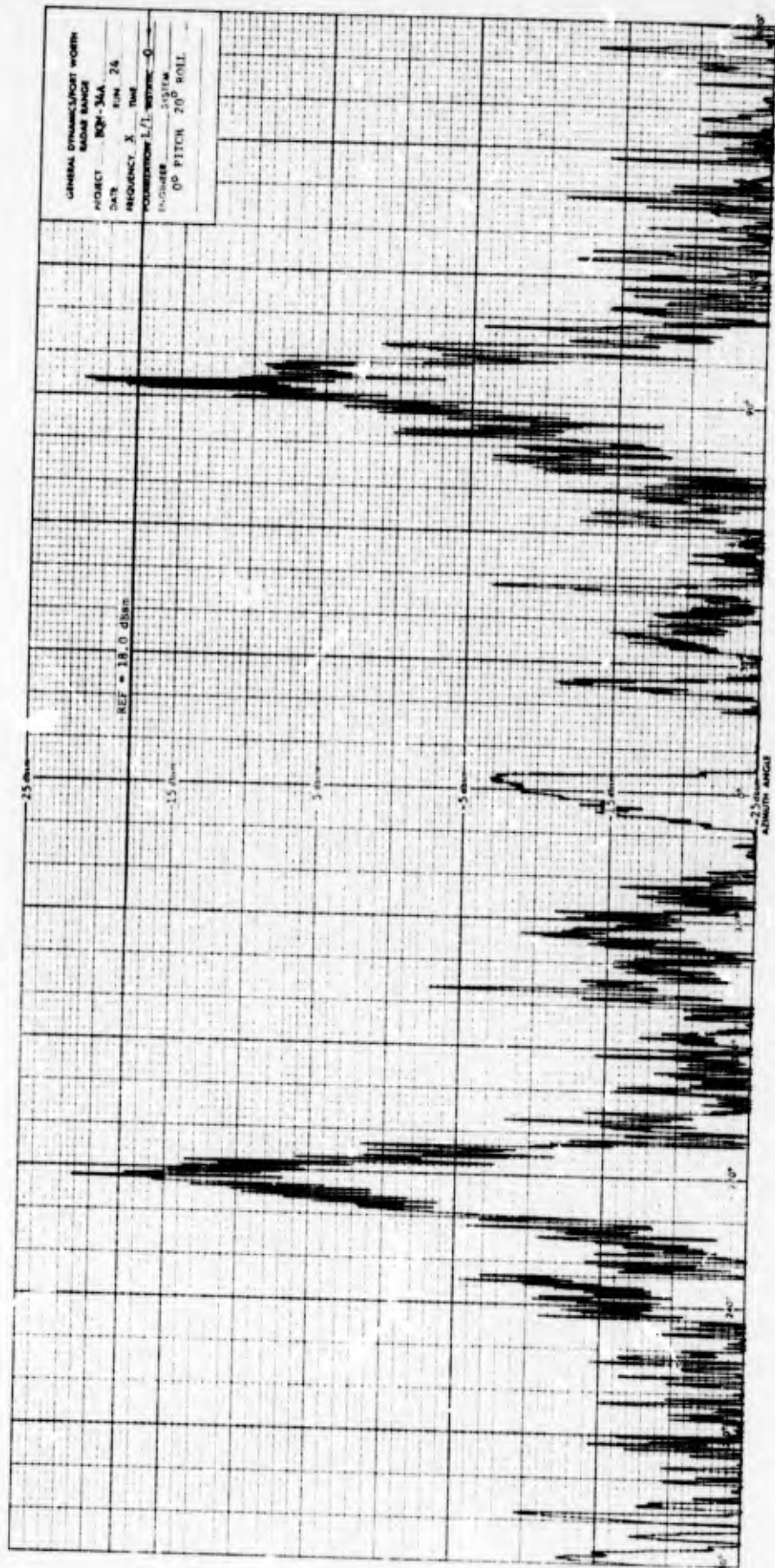


Fig. A-6 X-BAND RCS OF BQM-34A DRONE MODEL  
 (L/L POLARIZATION, 0° PITCH, 20° ROLL)

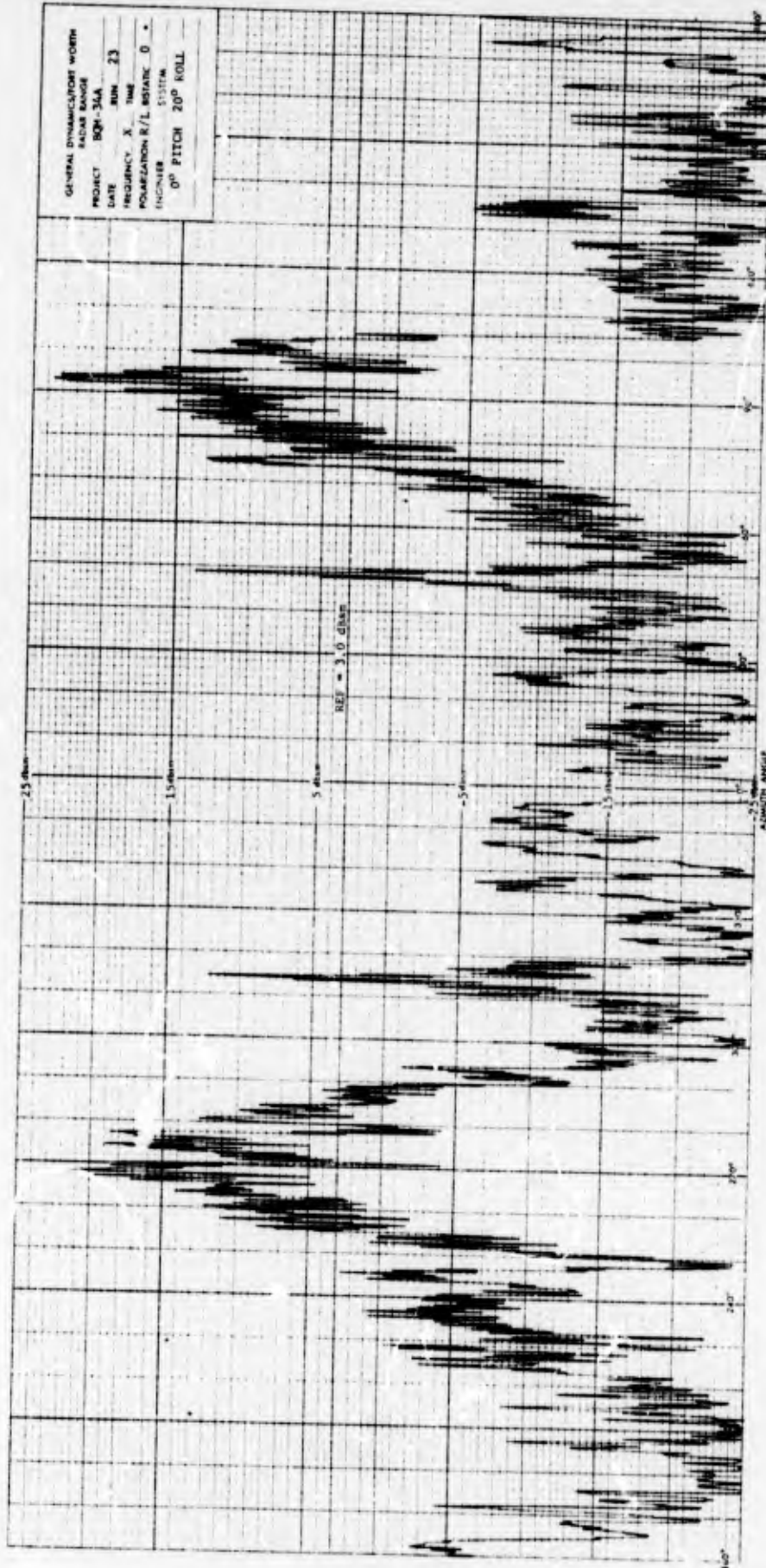


Fig. A-7 X-BAND RCS OF BQM-34A DRONE MODEL  
(R/L POLARIZATION, 0° PITCH, 20° ROLL)

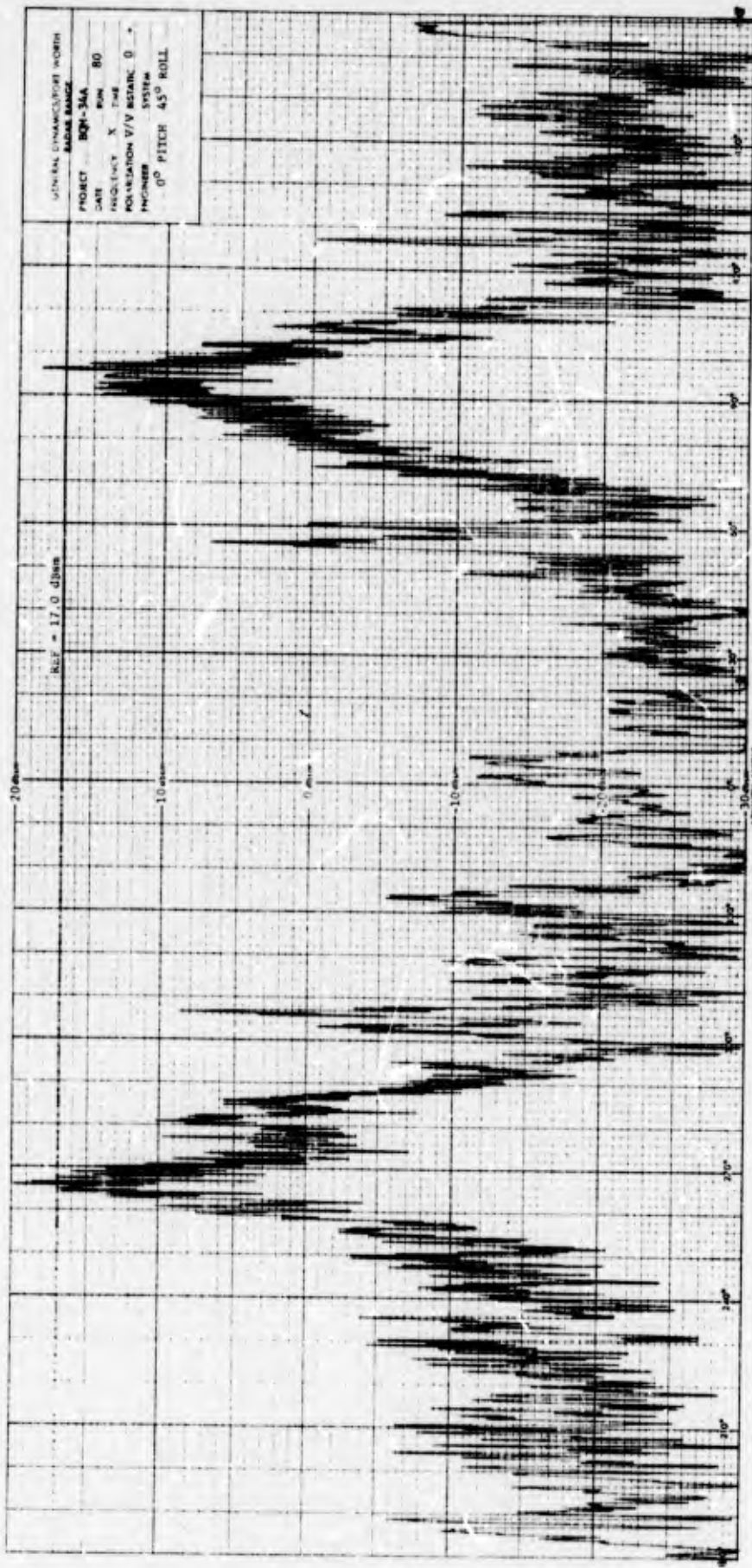


Fig. A-8 X-BAND RCS OF BQM-34A DRONE MODEL  
(V/V POLARIZATION, 0° PITCH, 45° ROLL)

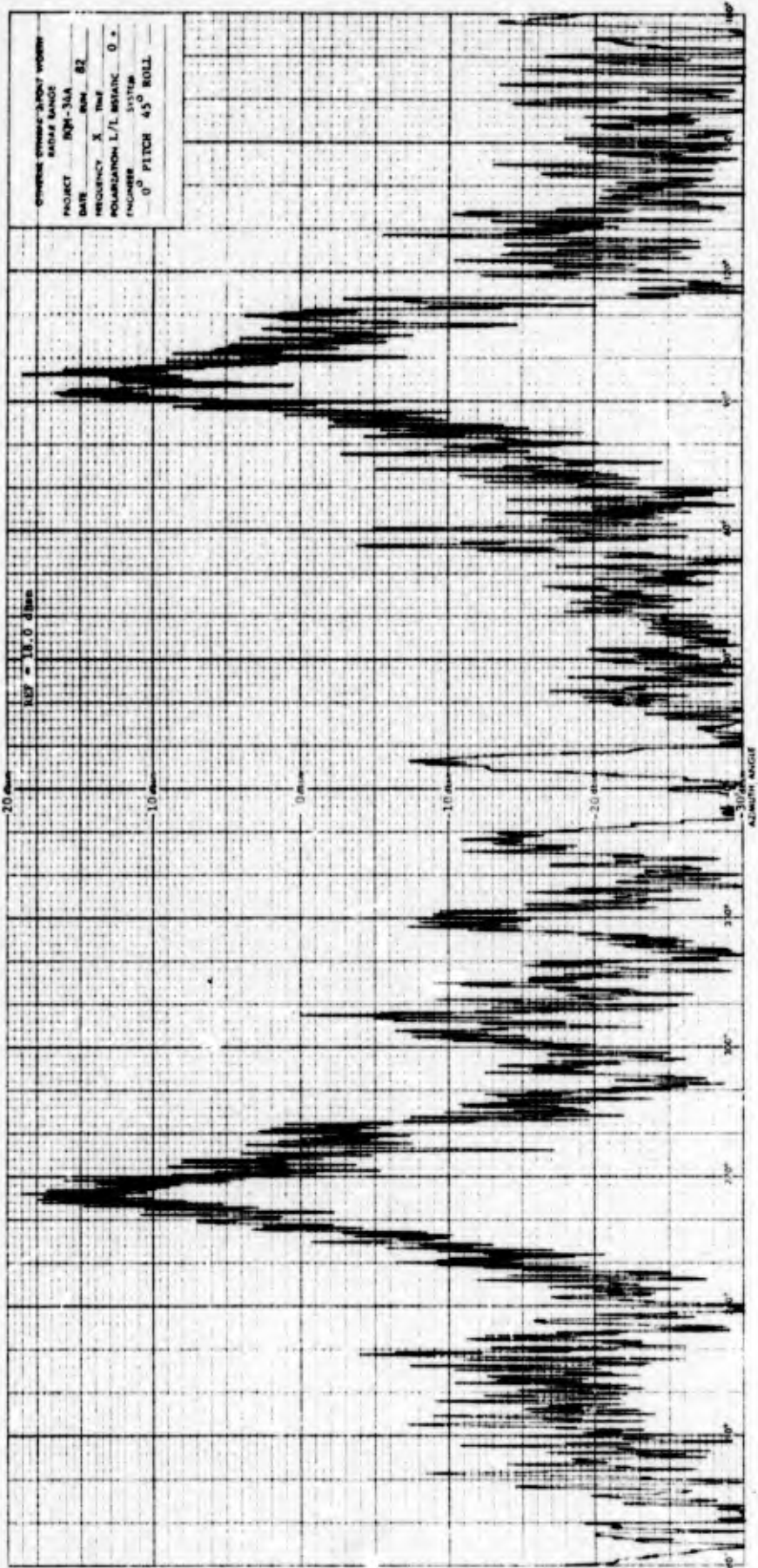


Fig. A-9 X-BAND RCS OF BQM-34A DRONE MODEL  
 (L/L POLARIZATION, 0° PITCH, 45° ROLL)

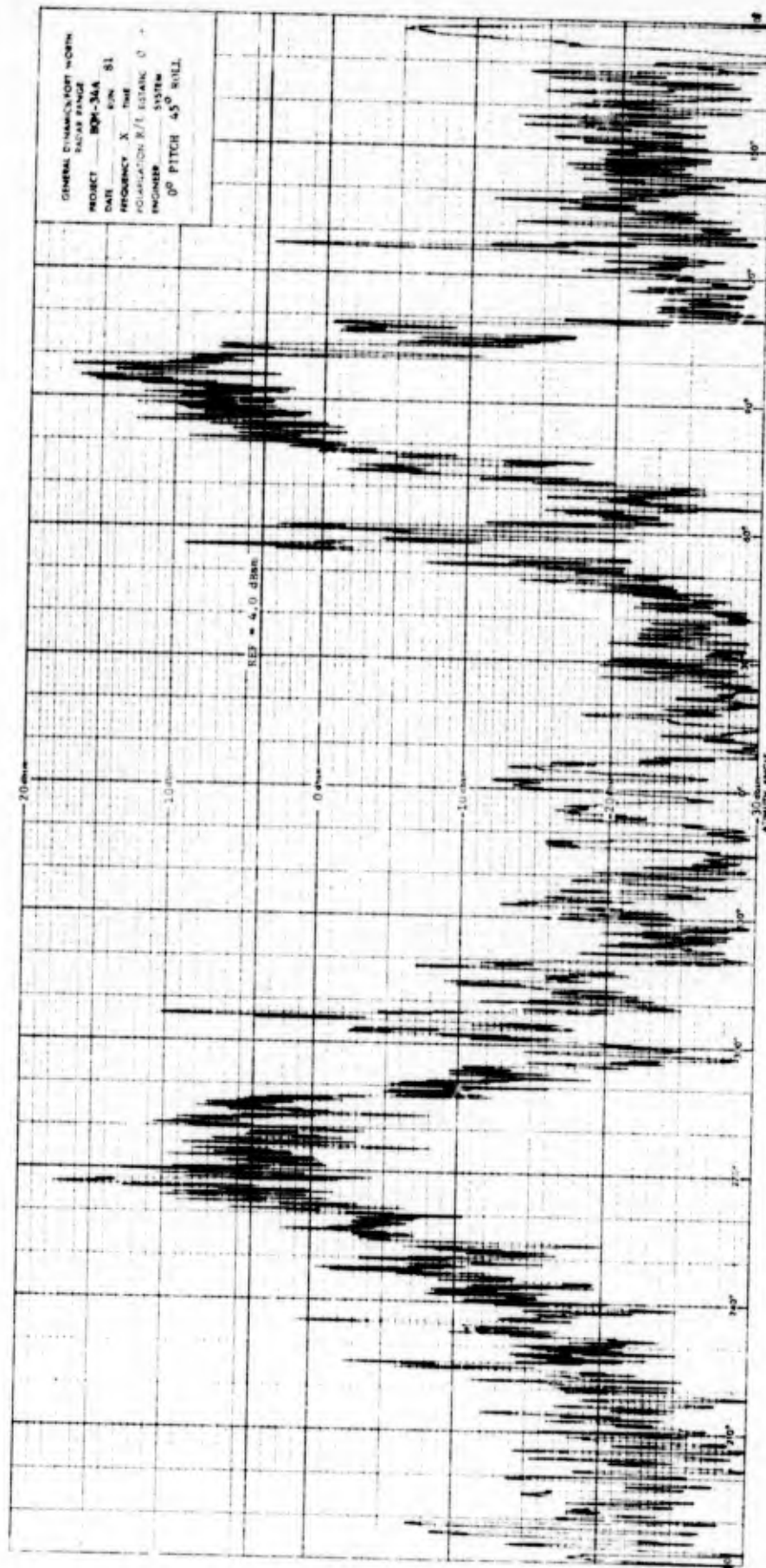


Fig. A-10 X-BAND RCS OF BQM-34A DRONE MODEL  
 (R/L POLARIZATION, 0° PITCH, 45° ROLL)

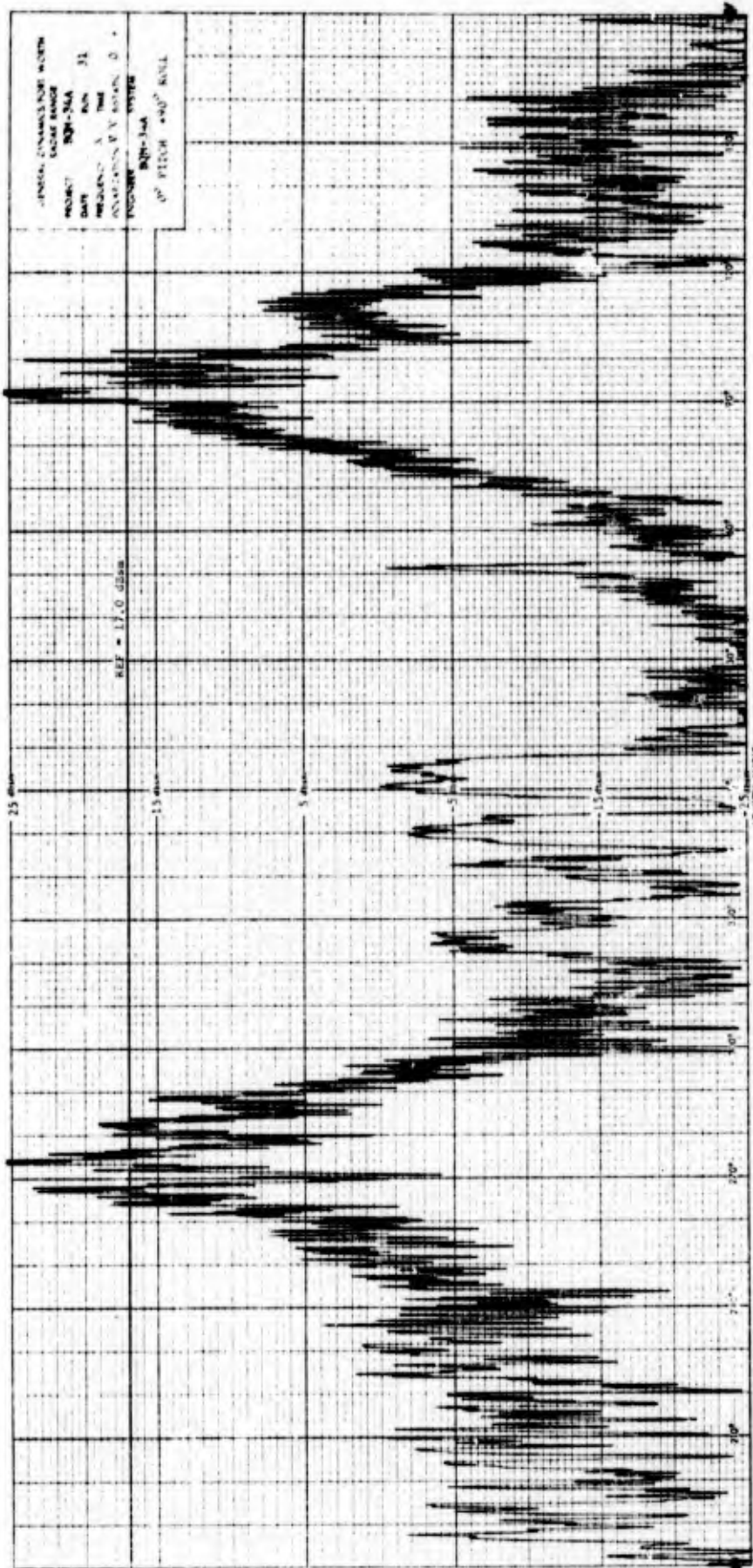


Fig. A-11 X-BAND RCS OF BQM-34A DRONE MODEL  
(V/V POLARIZATION, 0° PITCH, 90° ROLL)

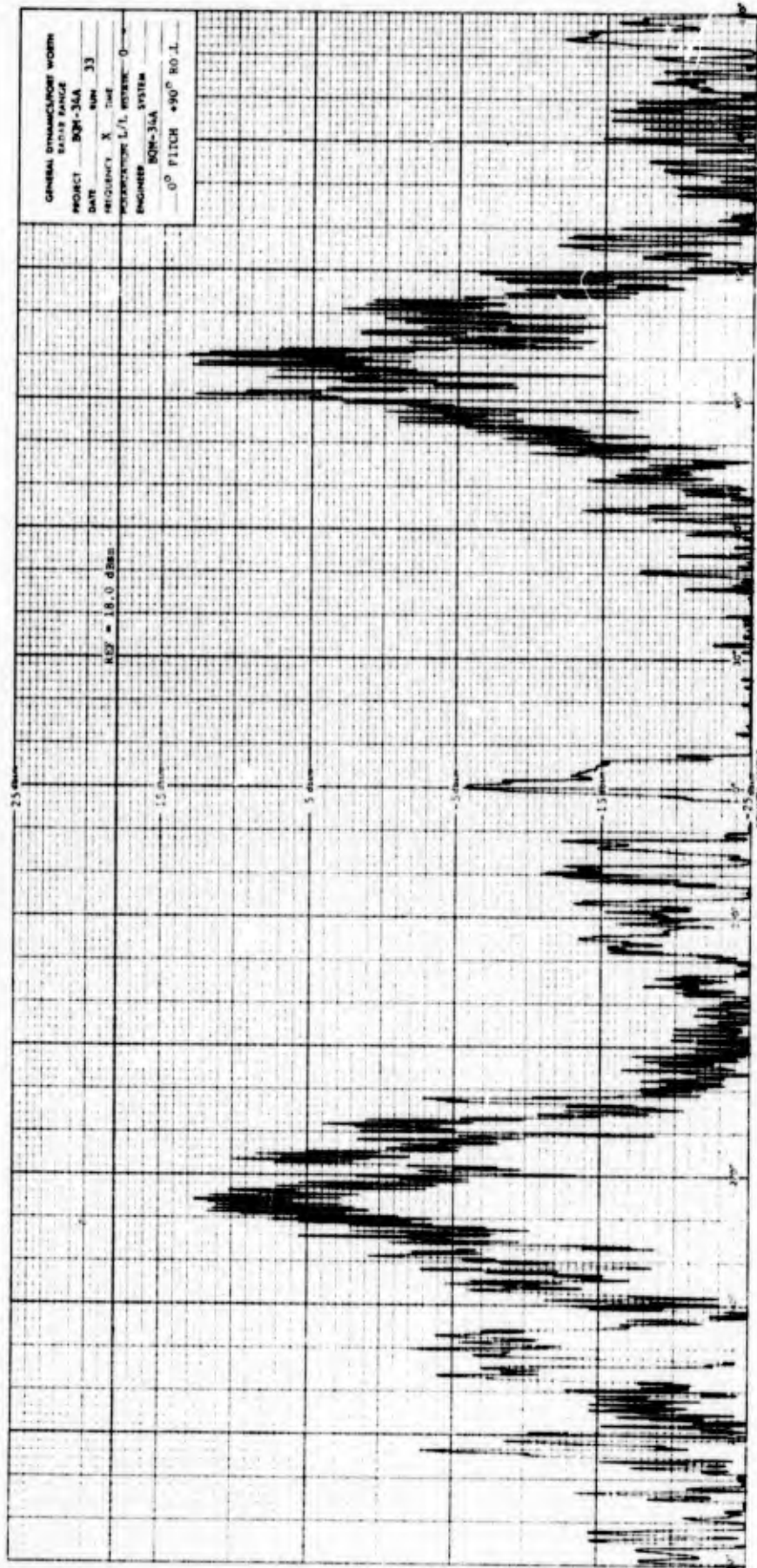


Fig. A-12 X-BAND RCS OF BQM-34A DRONE MODEL  
(L/L POLARIZATION, 0° PITCH, 90° ROLL)

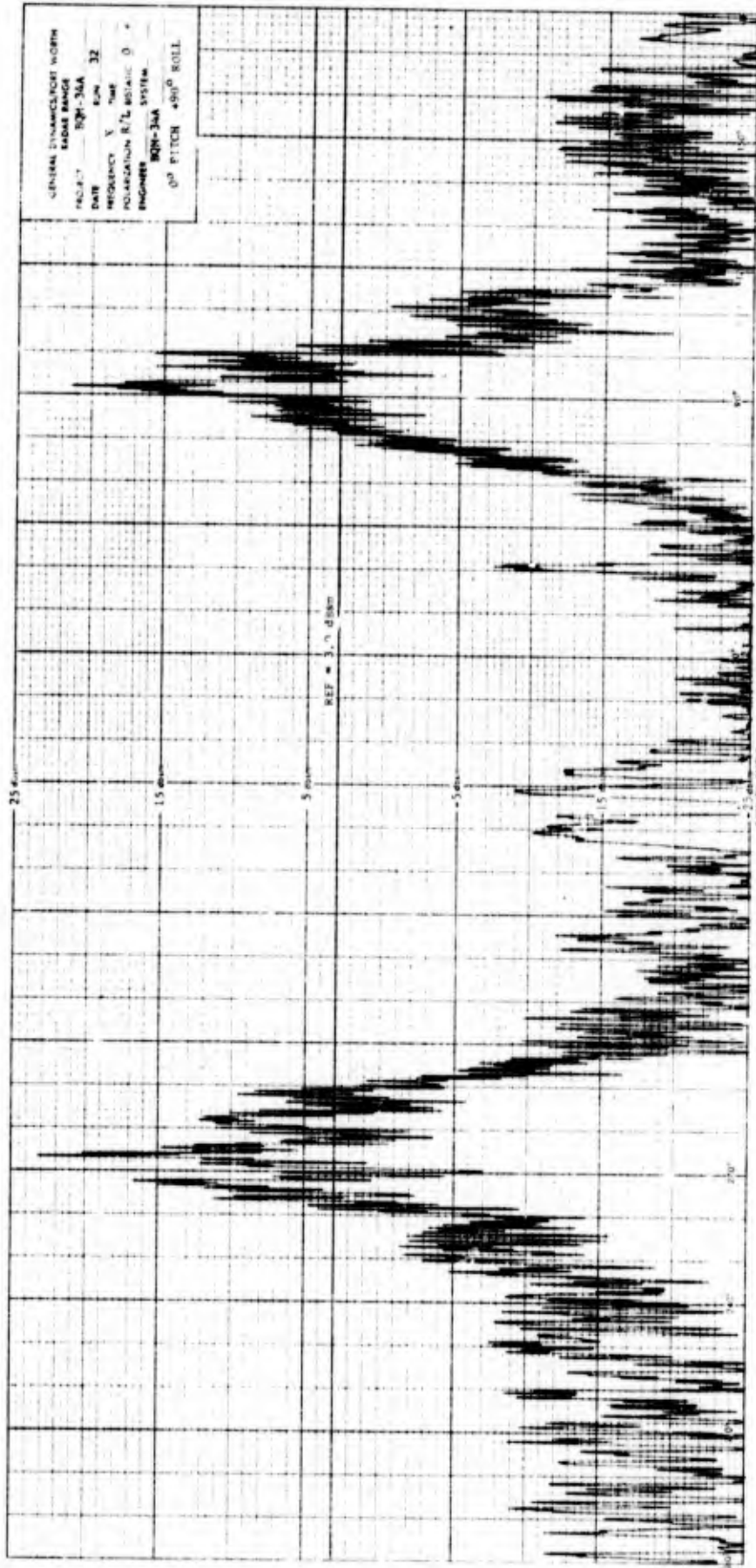


Fig. A-13 X-BAND RCS OF BQM-34A DRONE MODEL  
 (R/L POLARIZATION, 0° PITCH, 90° ROLL)

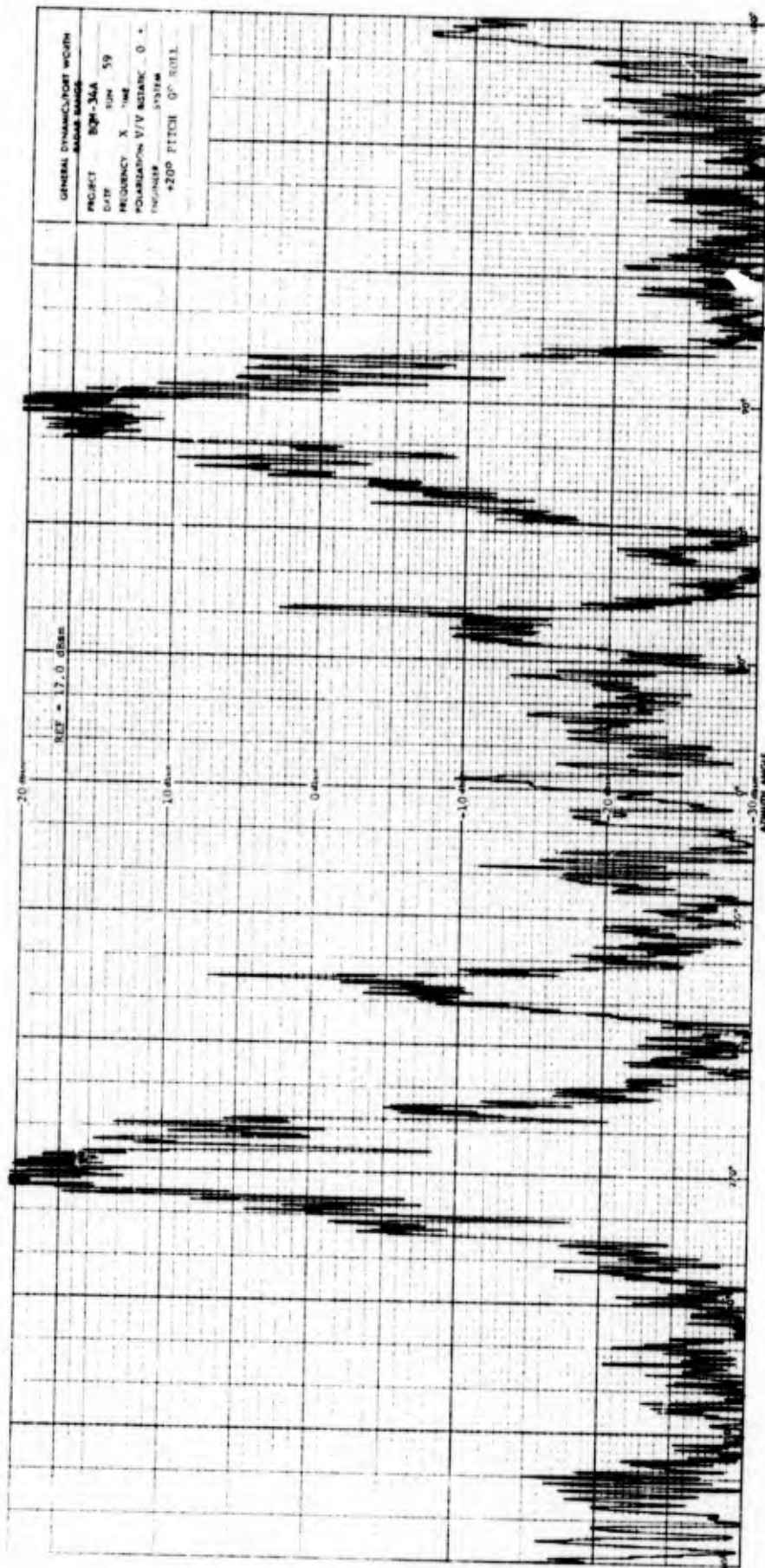


Fig. A-14 X-BAND RCS OF BQM-34A DRONE MODEL  
(V/V POLARIZATION, 20° PITCH, 0° ROLL)

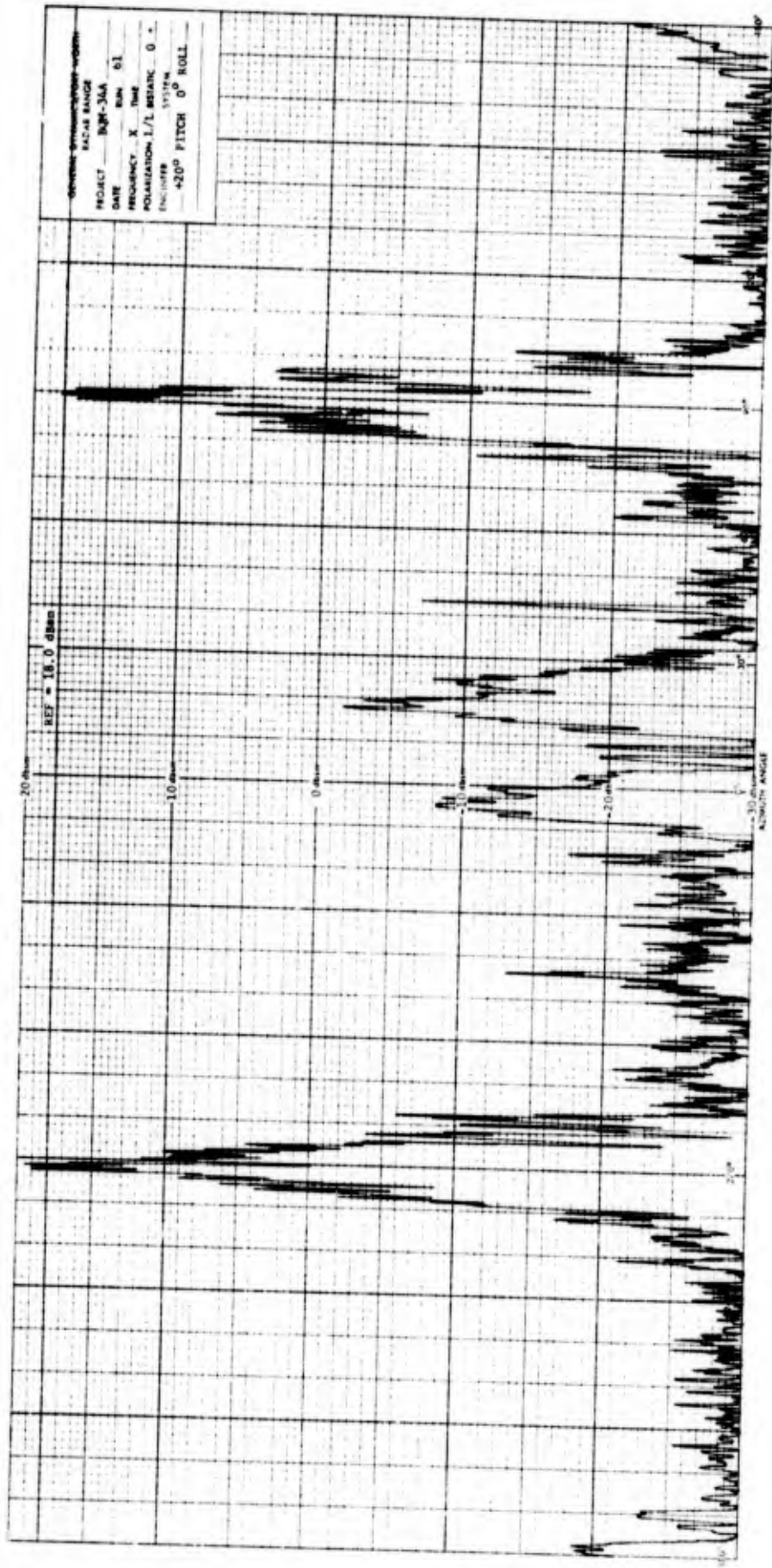


Fig. A-15 X-BAND RCS OF BQM-34A DRONE MODEL  
(L/L POLARIZATION, 20° PITCH, 0° ROLL)

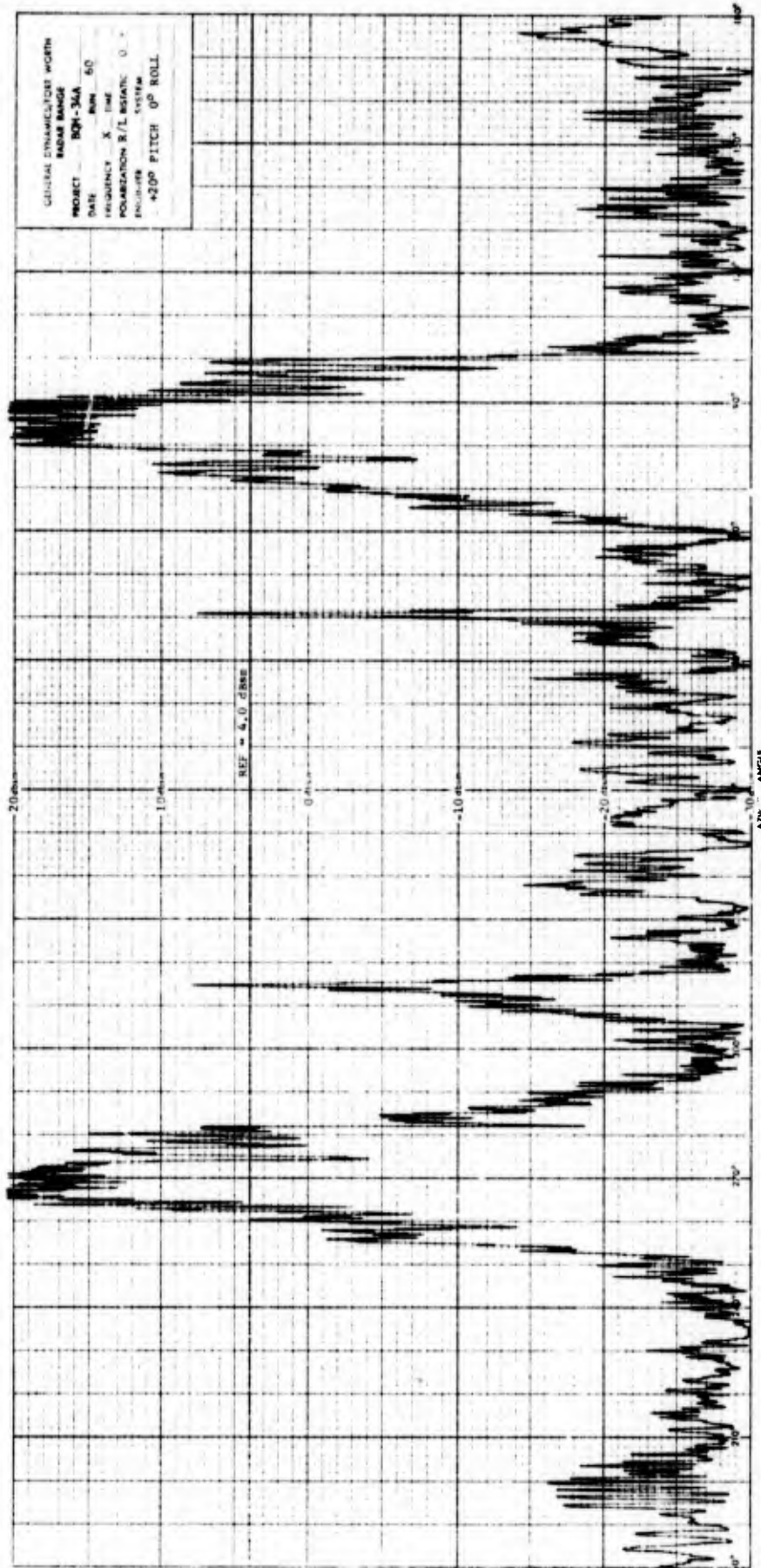


Fig. A-16 X-BAND RCS OF BQM-34A DRONE MODEL  
 (R/L POLARIZATION, 20° PITCH, 0° ROLL)

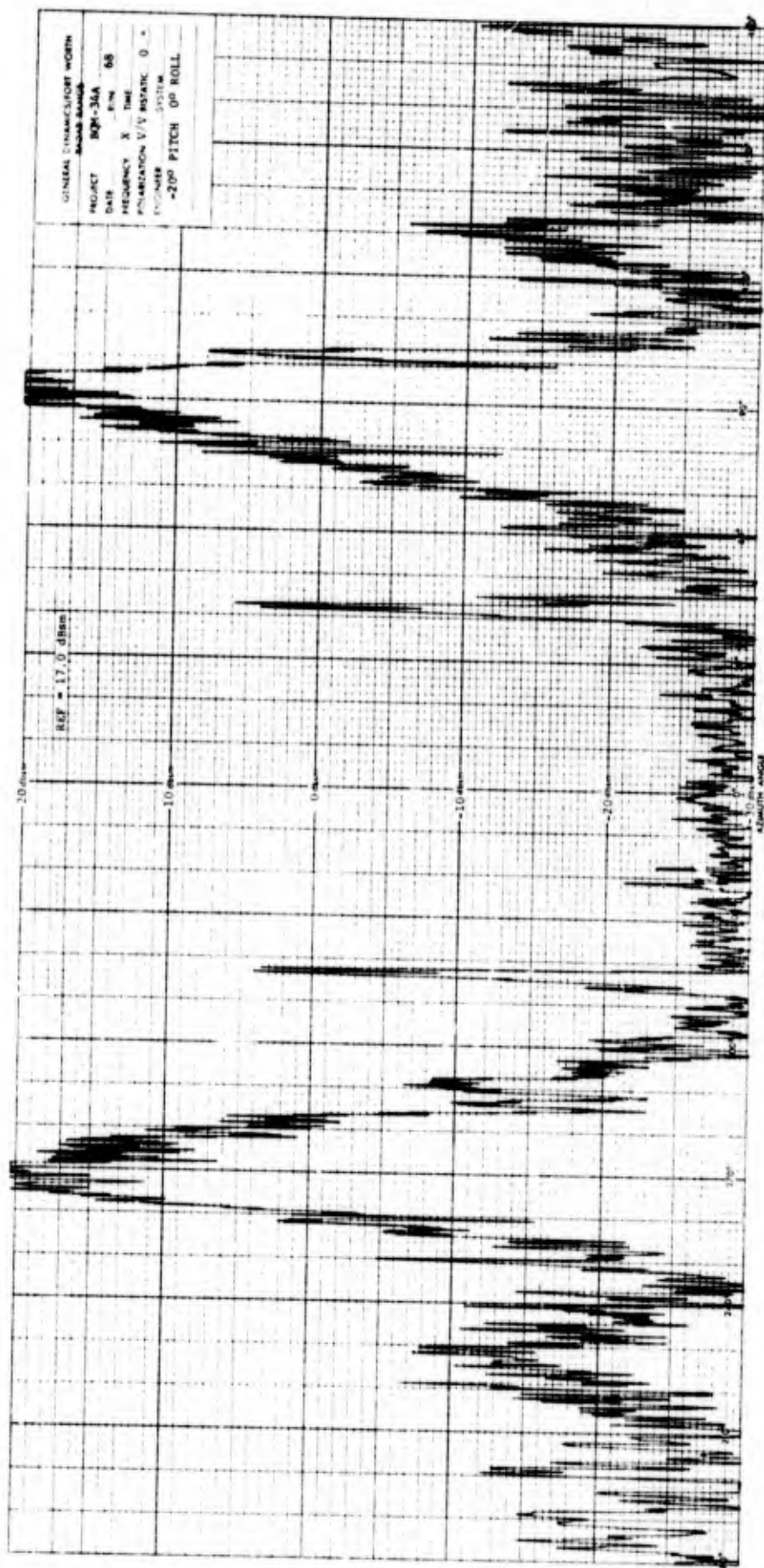


Fig. A-17 X-BAND RCS OF BQM-34A DRONE MODEL  
(V/V POLARIZATION, -20° PITCH, 0° ROLL)

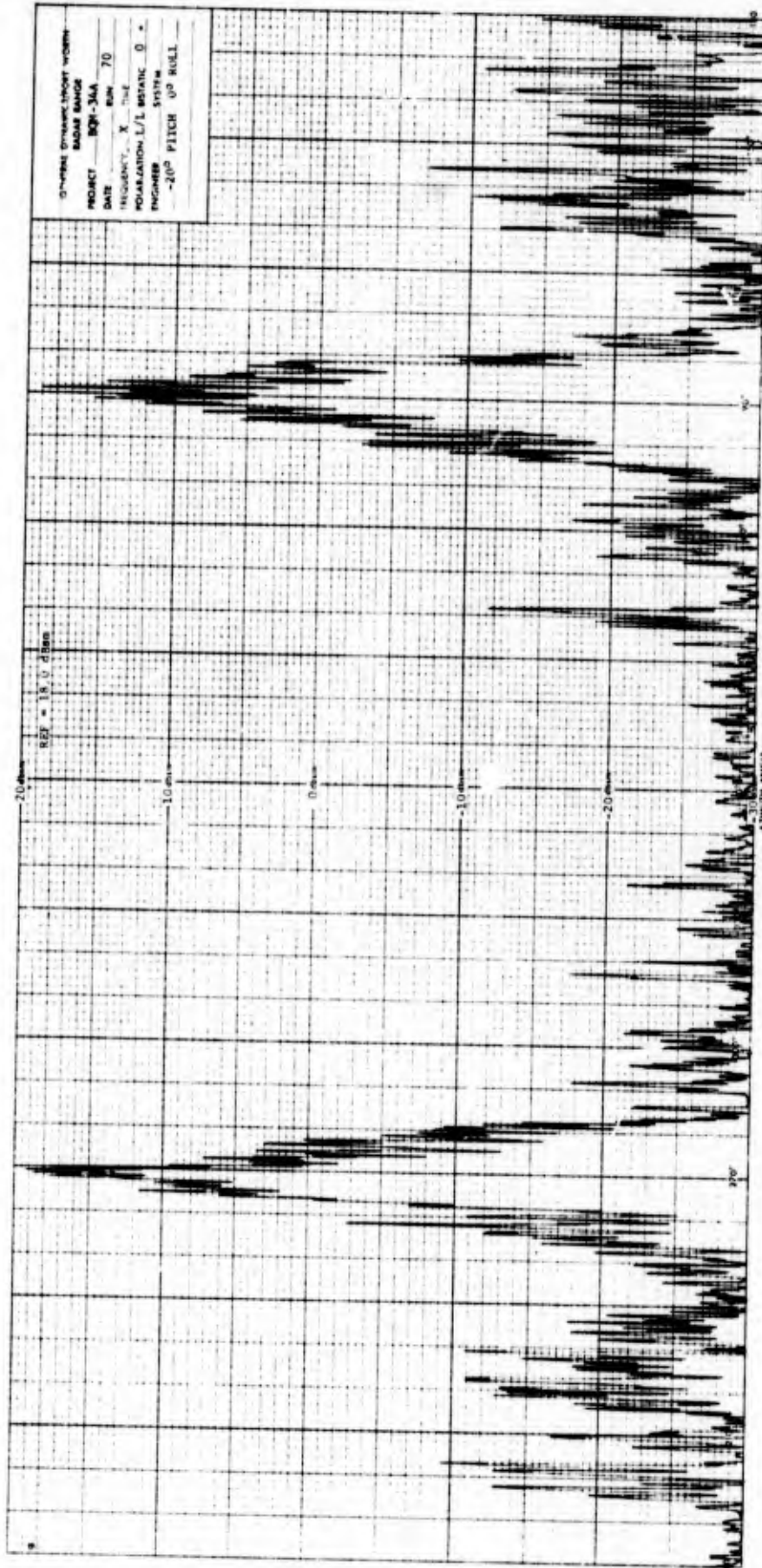


Fig. A-18 X-BAND RCS OF BQM-34A DRONE MODEL  
 (L/L POLARIZATION, -20° PITCH, 0° ROLL)

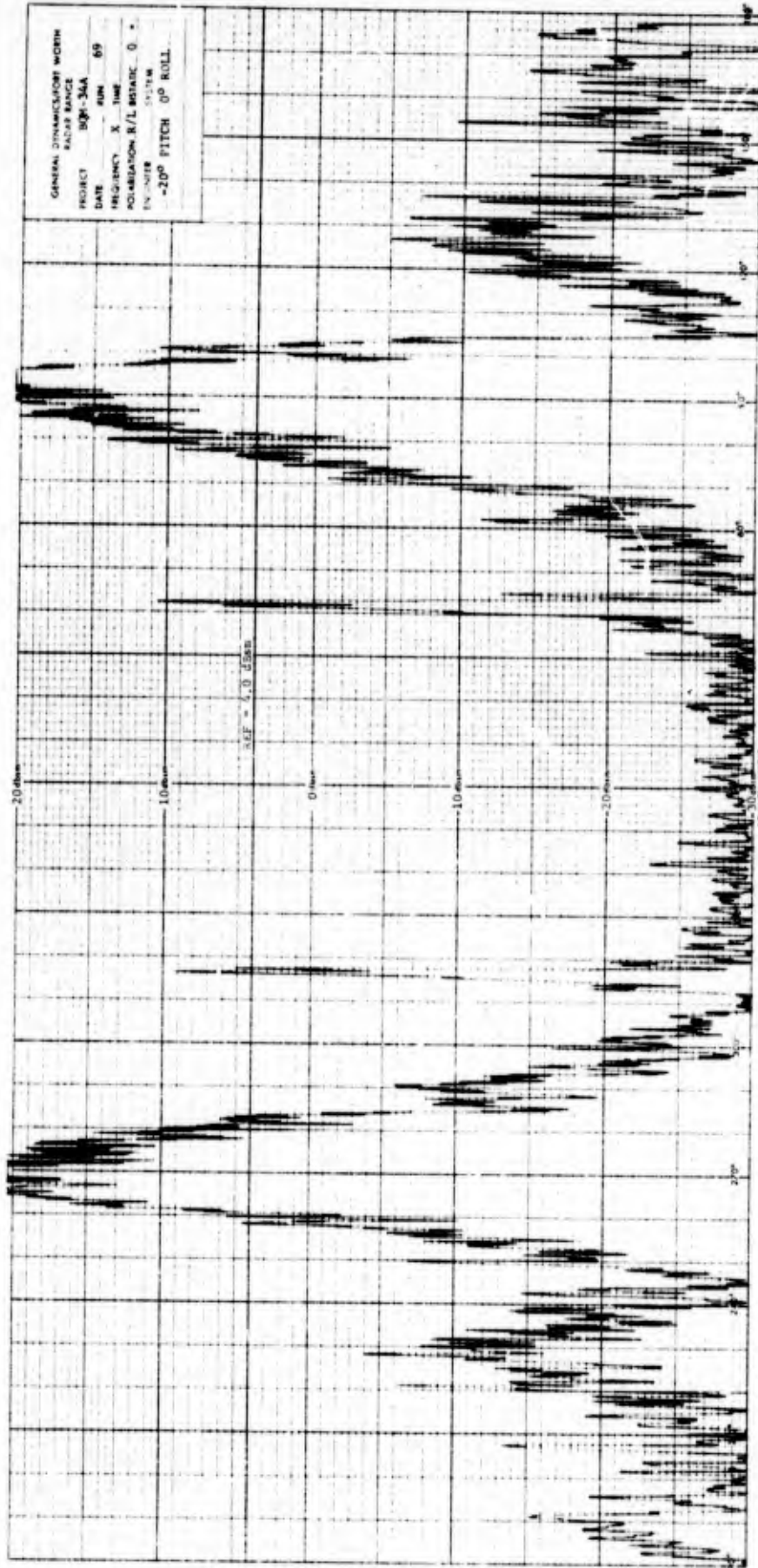


Fig. A-19 X-BAND RCS OF BQM-34A DRONE MODEL  
(R/L POLARIZATION, -20° PITCH, 0° ROLL)

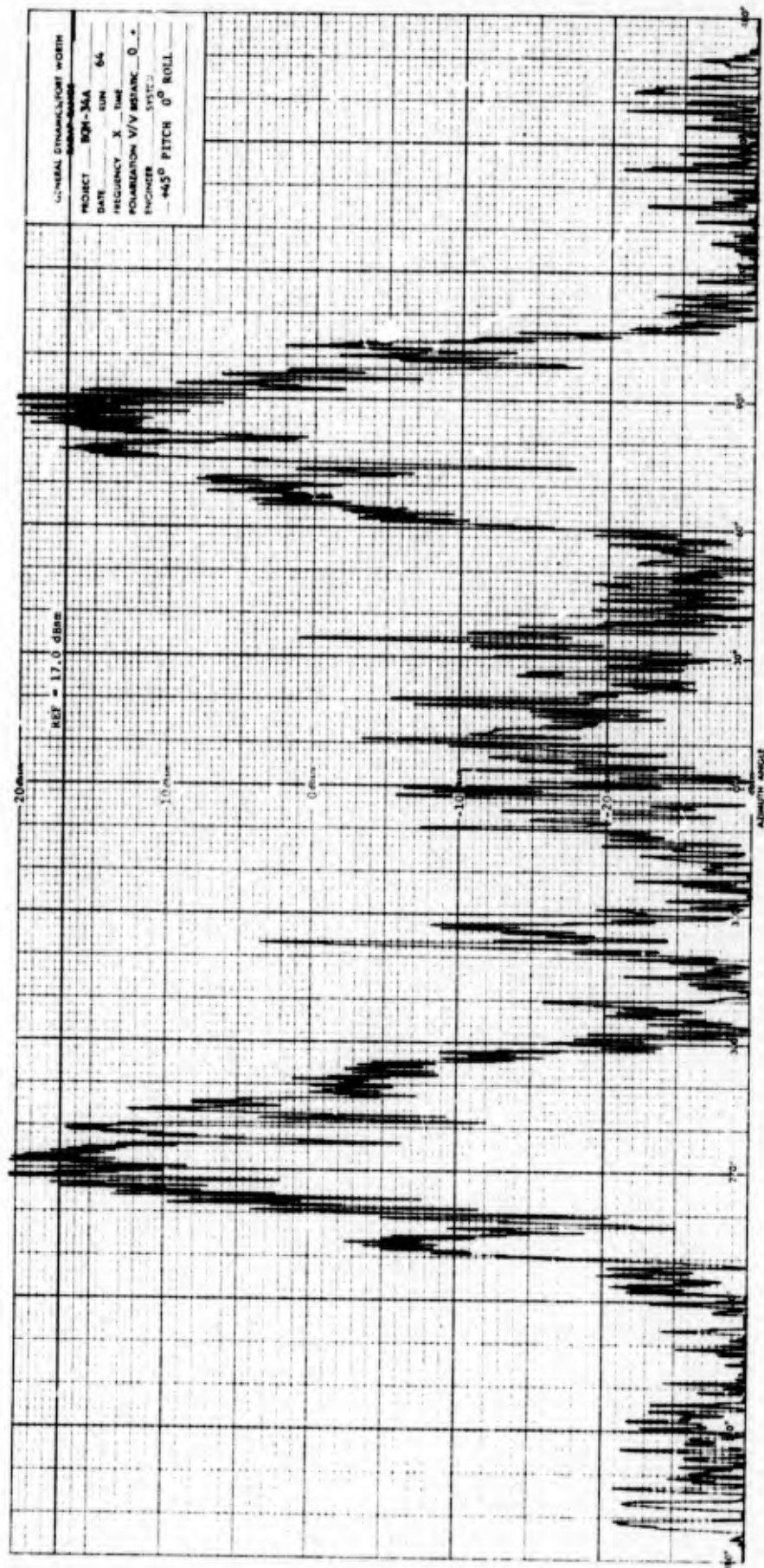


Fig. A-20 X-BAND RCS OF BQM-34A DRONE MODEL  
(V/V POLARIZATION, 45° PITCH, 0° ROLL)

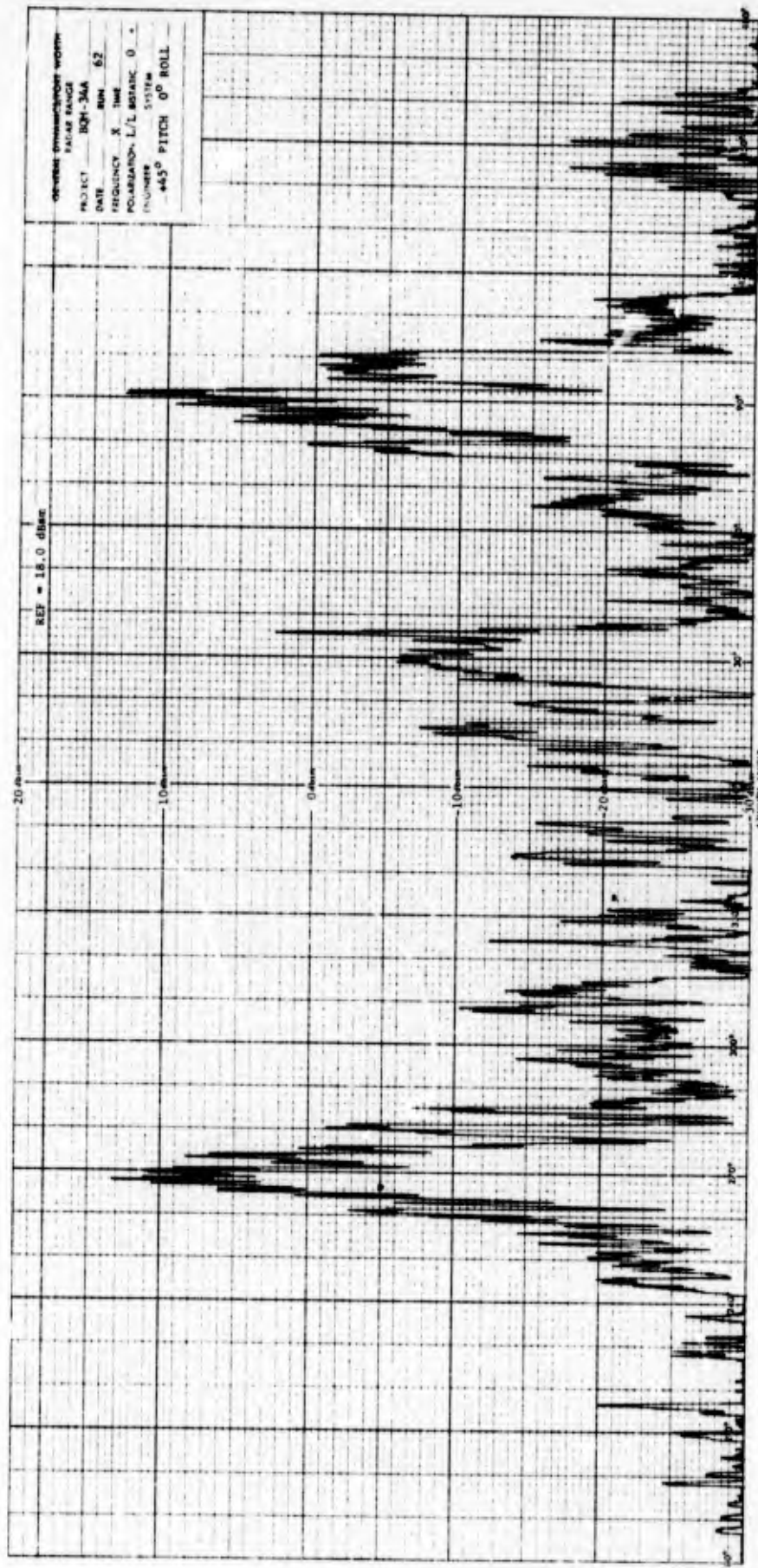


Fig. A-21 X-BAND RCS OF BQM-34A DRONE MODEL  
(L/L POLARIZATION, 45° PITCH, 0° ROLL)

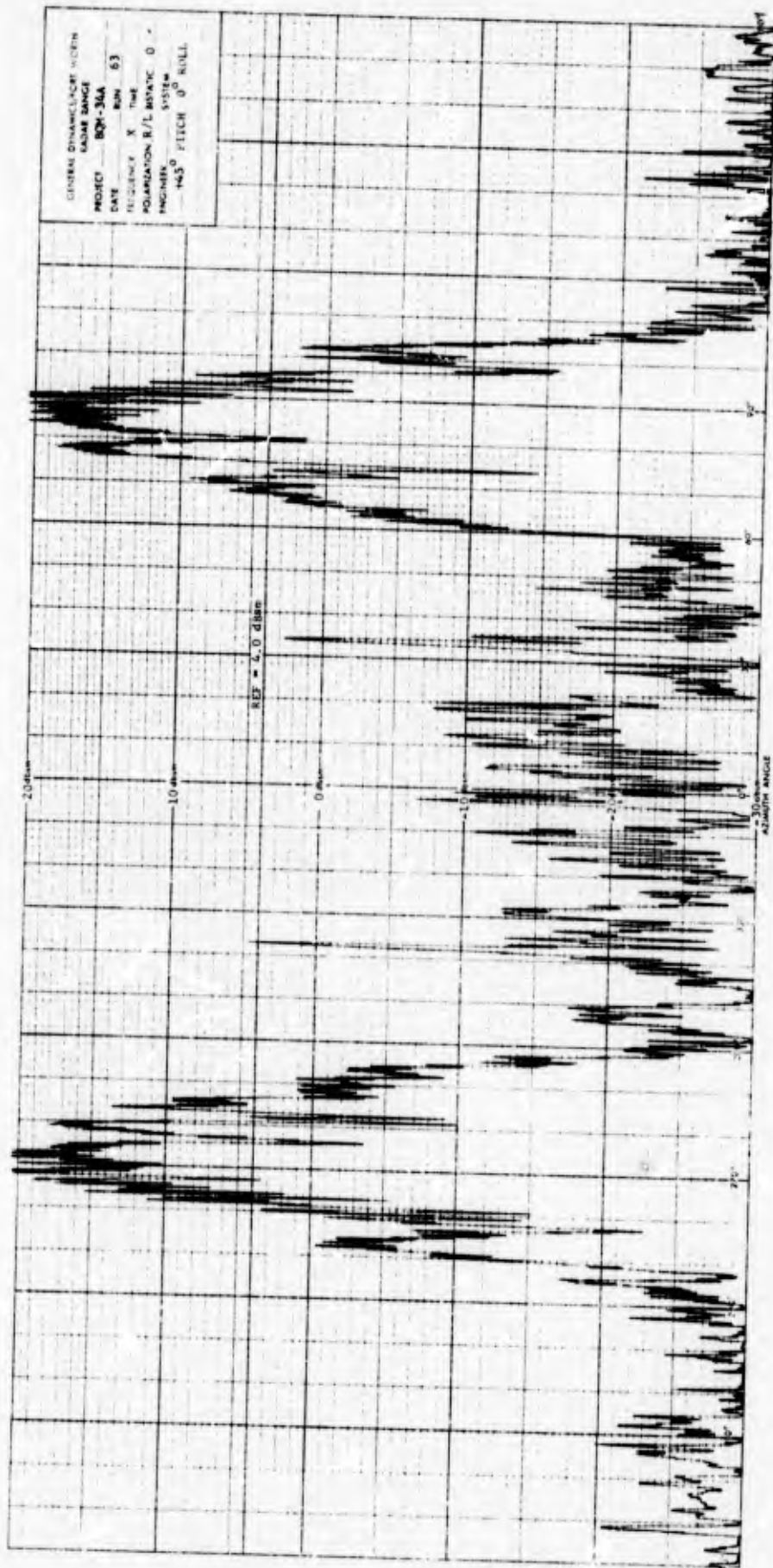


Fig. A-22 X-BAND RCS OF BQM-34A DRONE MODEL  
 (R/L POLARIZATION, 45° PITCH, 0° ROLL)

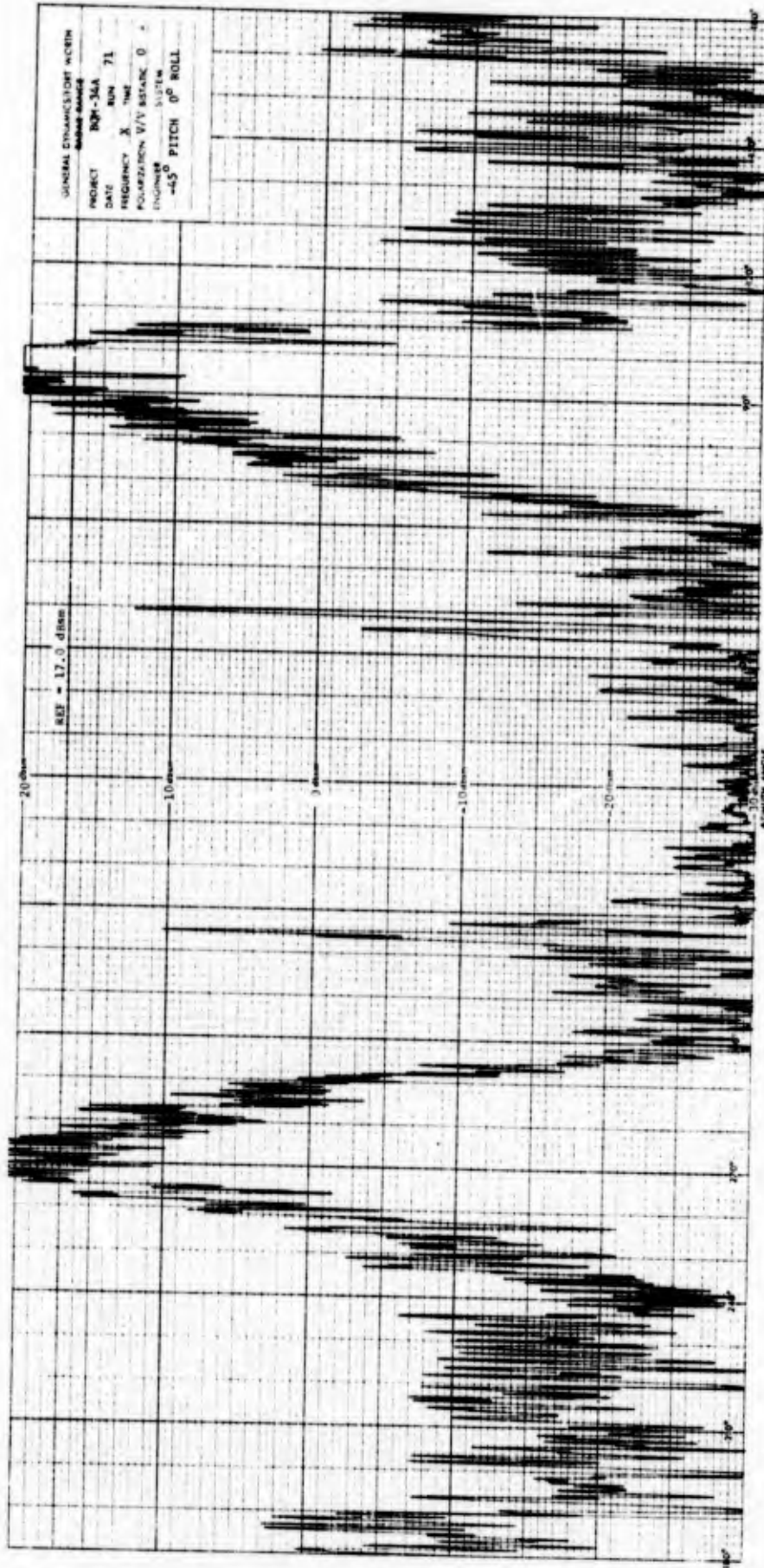


Fig. A-23 X-BAND RCS OF EQM-34A DRONE MODEL  
(V/V POLARIZATION, -45° PITCH, 0° ROLL)

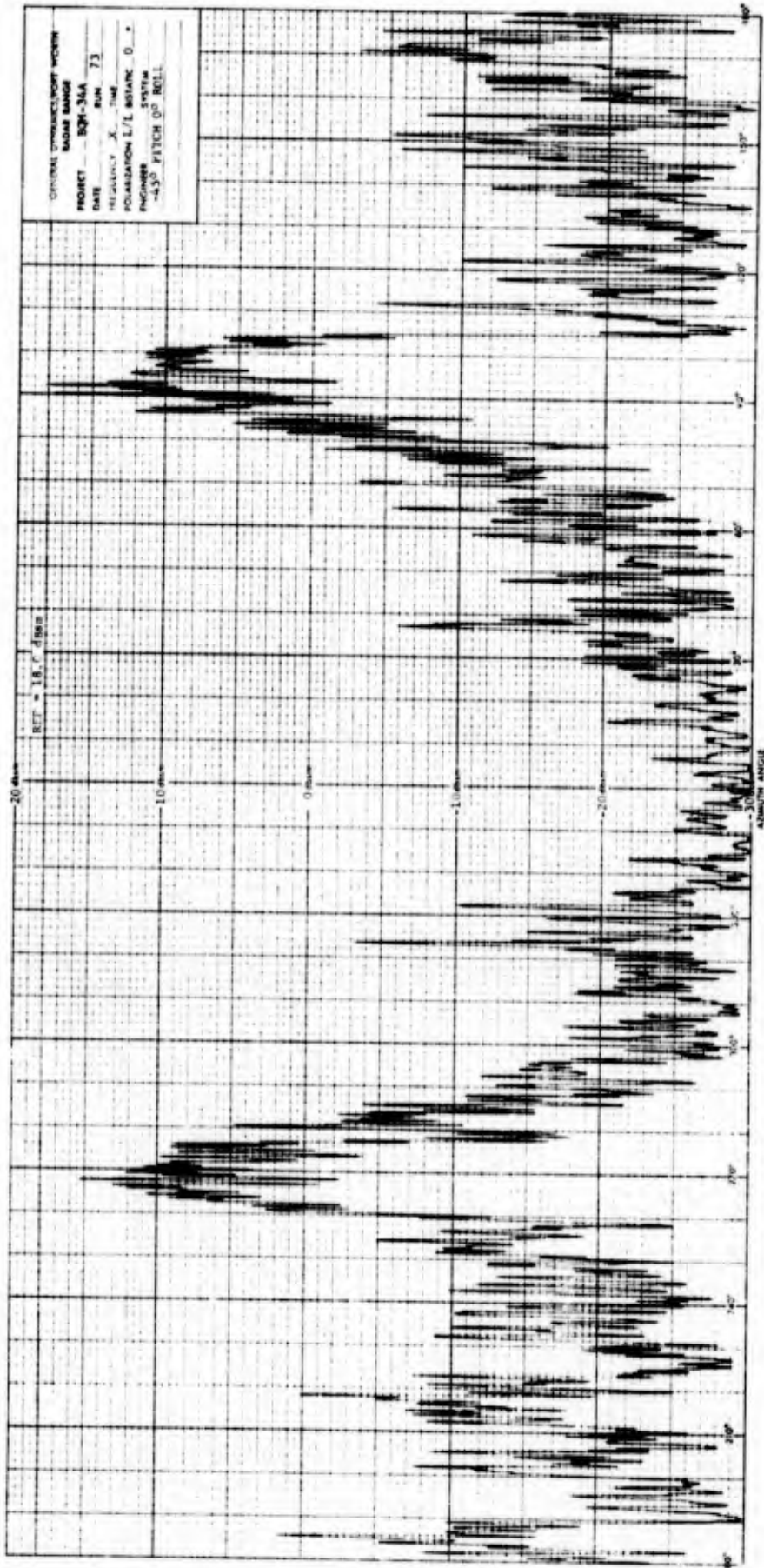


Fig. A-24 X-BAND RCS OF BQM-34A DRONE MODEL  
(L/L POLARIZATION, -45° PITCH, 0° ROLL)

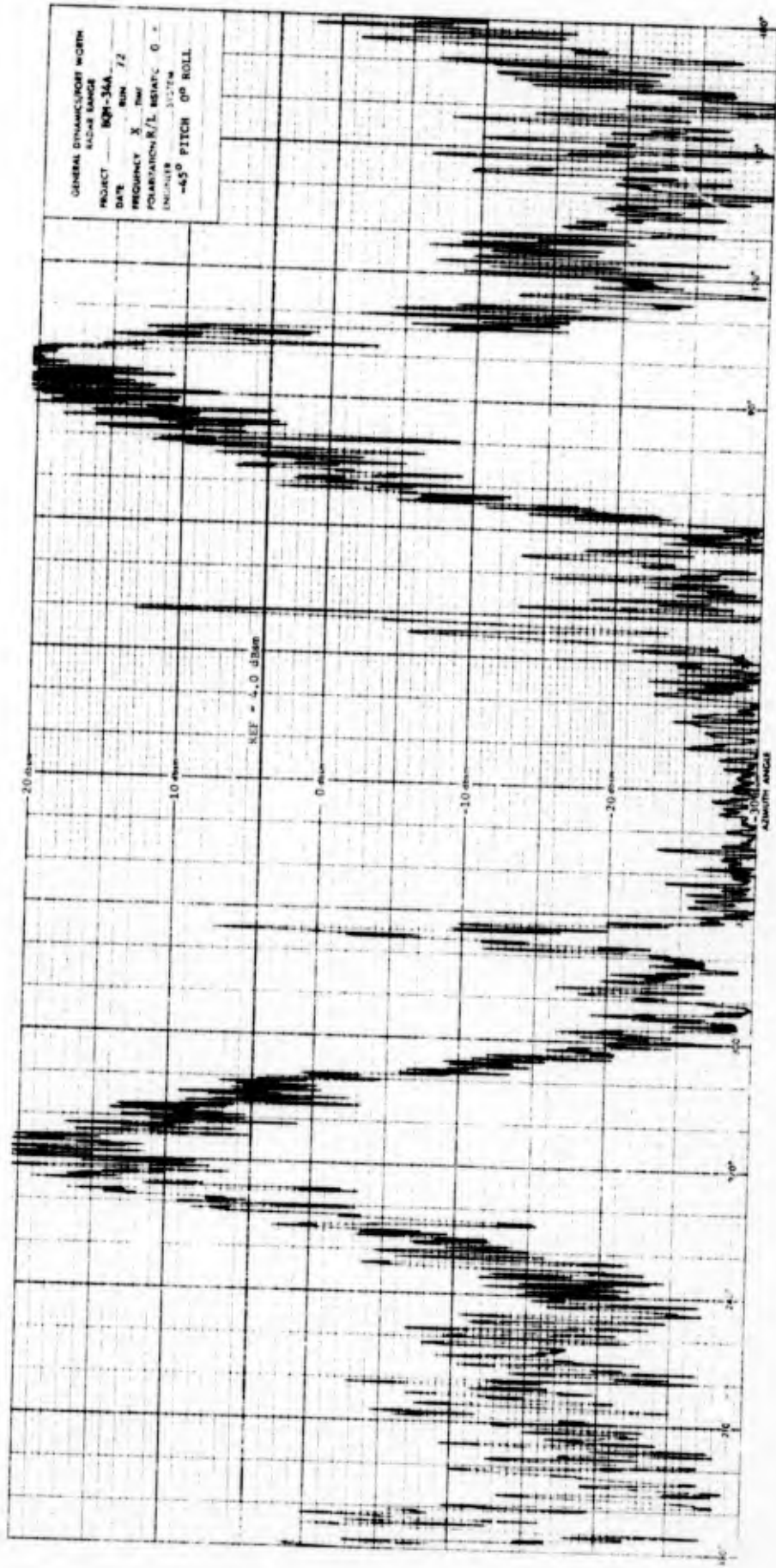


Fig. A-25 X-BAND RCS OF BQM-34A DRONE MODEL  
 (R/L POLARIZATION, -45° PITCH, 0° ROLL)

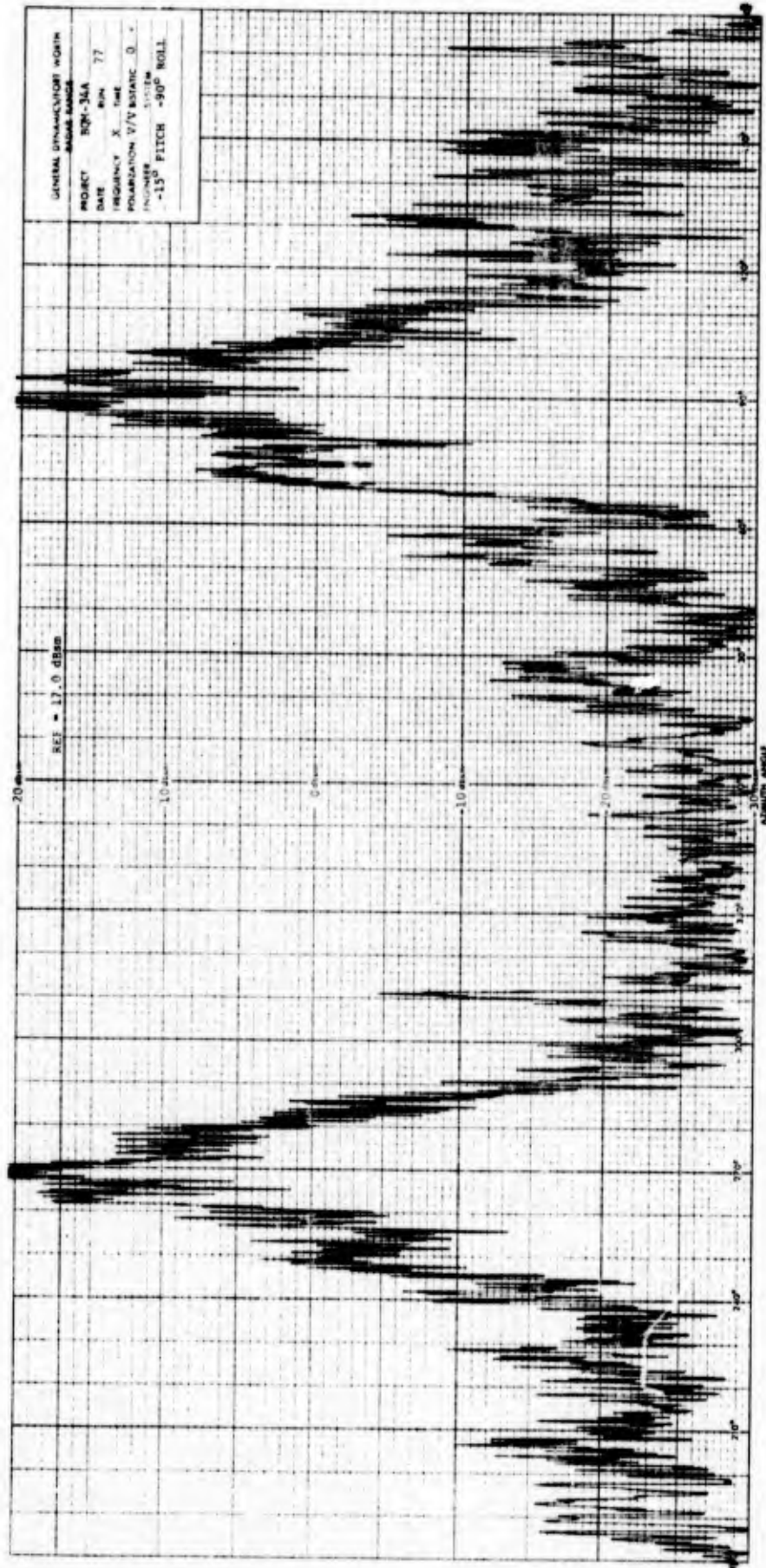


Fig. A-26 X-BAND RCS OF BQM-34A DRONE MODEL  
(V/V POLARIZATION, -15° PITCH, -90° ROLL)



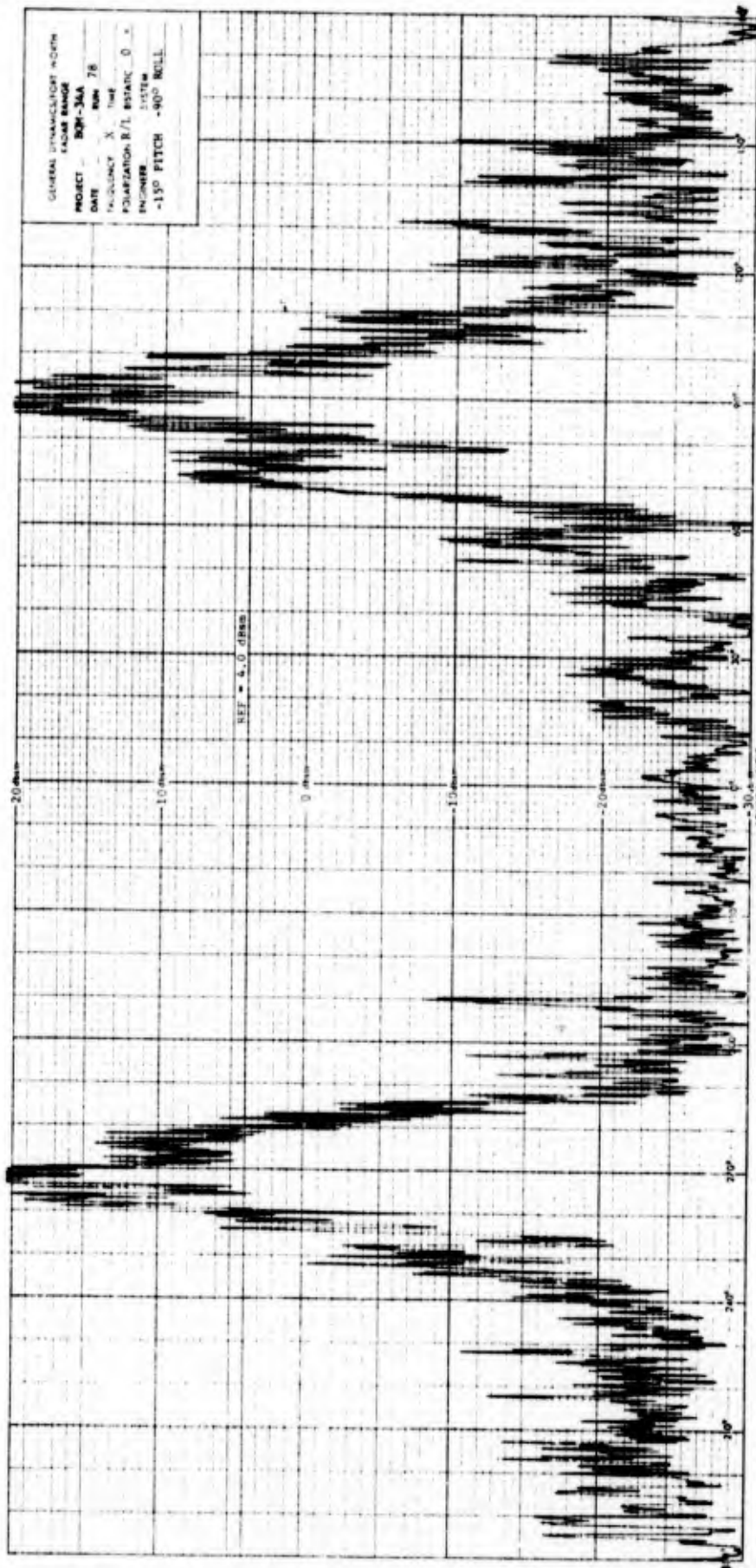


Fig. A-28 X-BAND RCS OF BQM-34A DRONE MODEL  
 (R/L POLARIZATION, -15° PITCH, -90° ROLL)

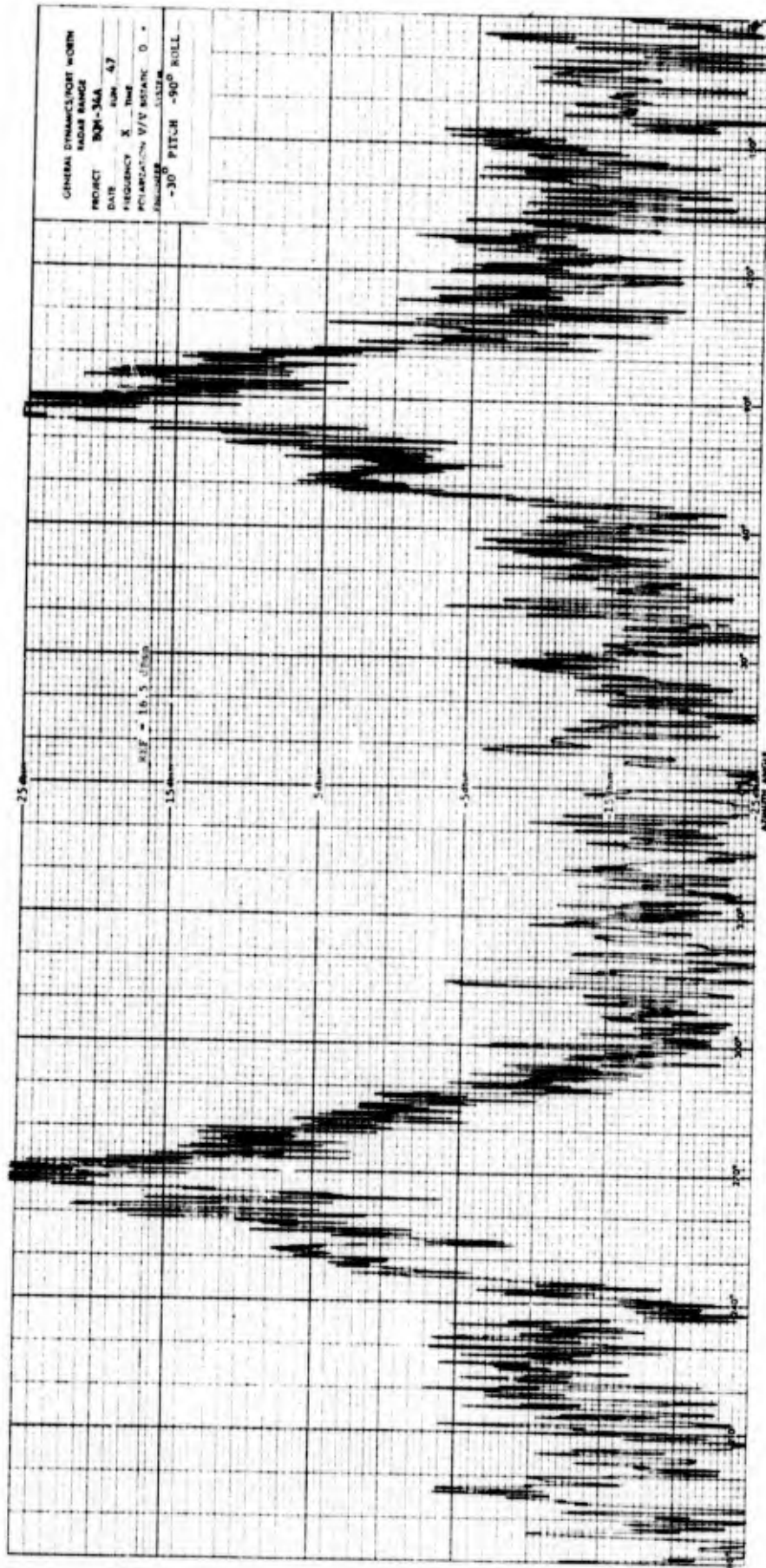


Fig. A-29 X-BAND RCS OF BQM-34A DRONE MODEL  
 (V/V POLARIZATION, -30° PITCH, -90° ROLL)

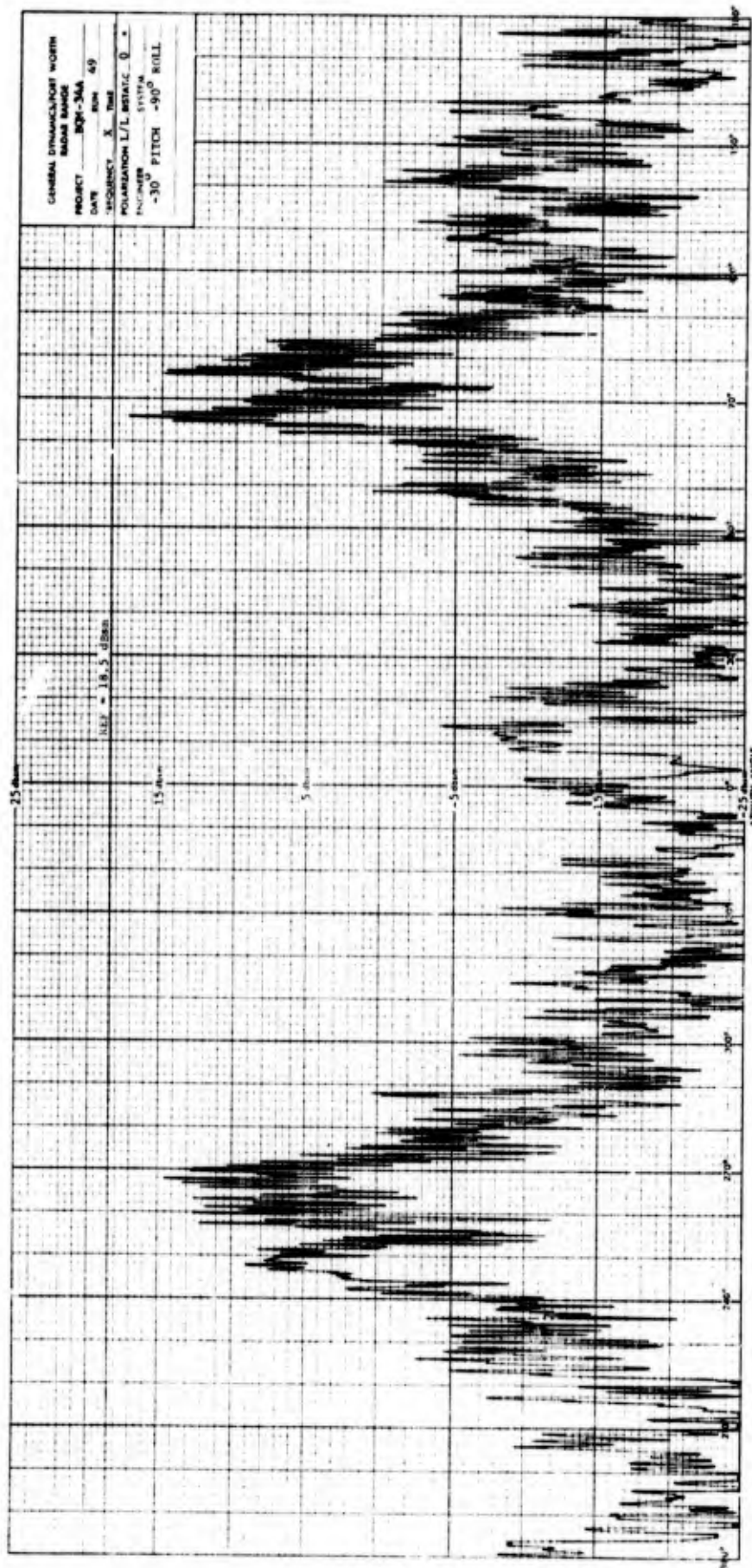


Fig. A-30 X-BAND RCS OF BQM-34A DRONE MODEL  
(L/L POLARIZATION, -30° PITCH, -90° ROLL)

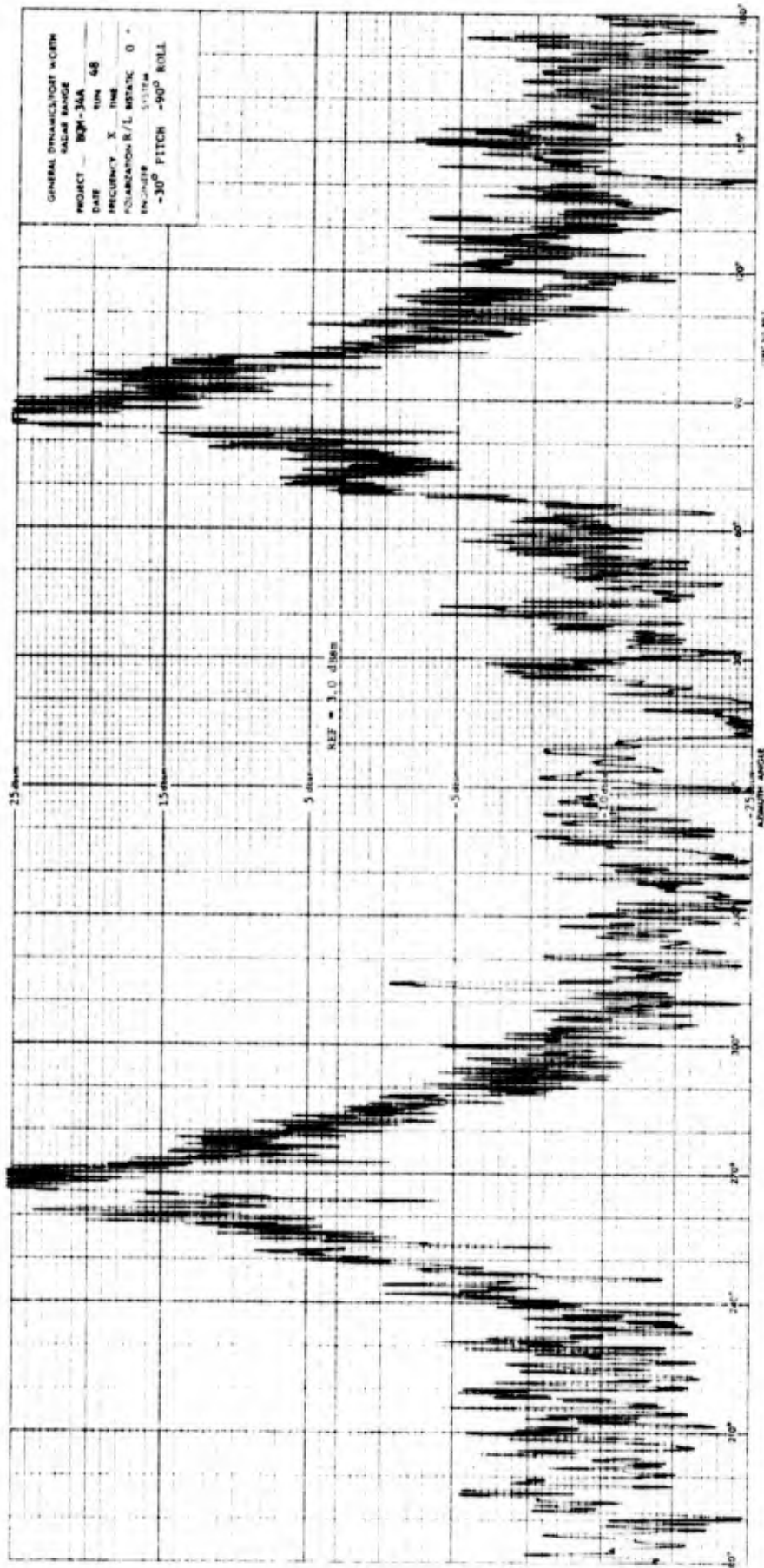


Fig. A-31 X-BAND RCS OF BQM-34A DRONE MODEL  
 (R/L POLARIZATION, -30° PITCH, -90° ROLL)

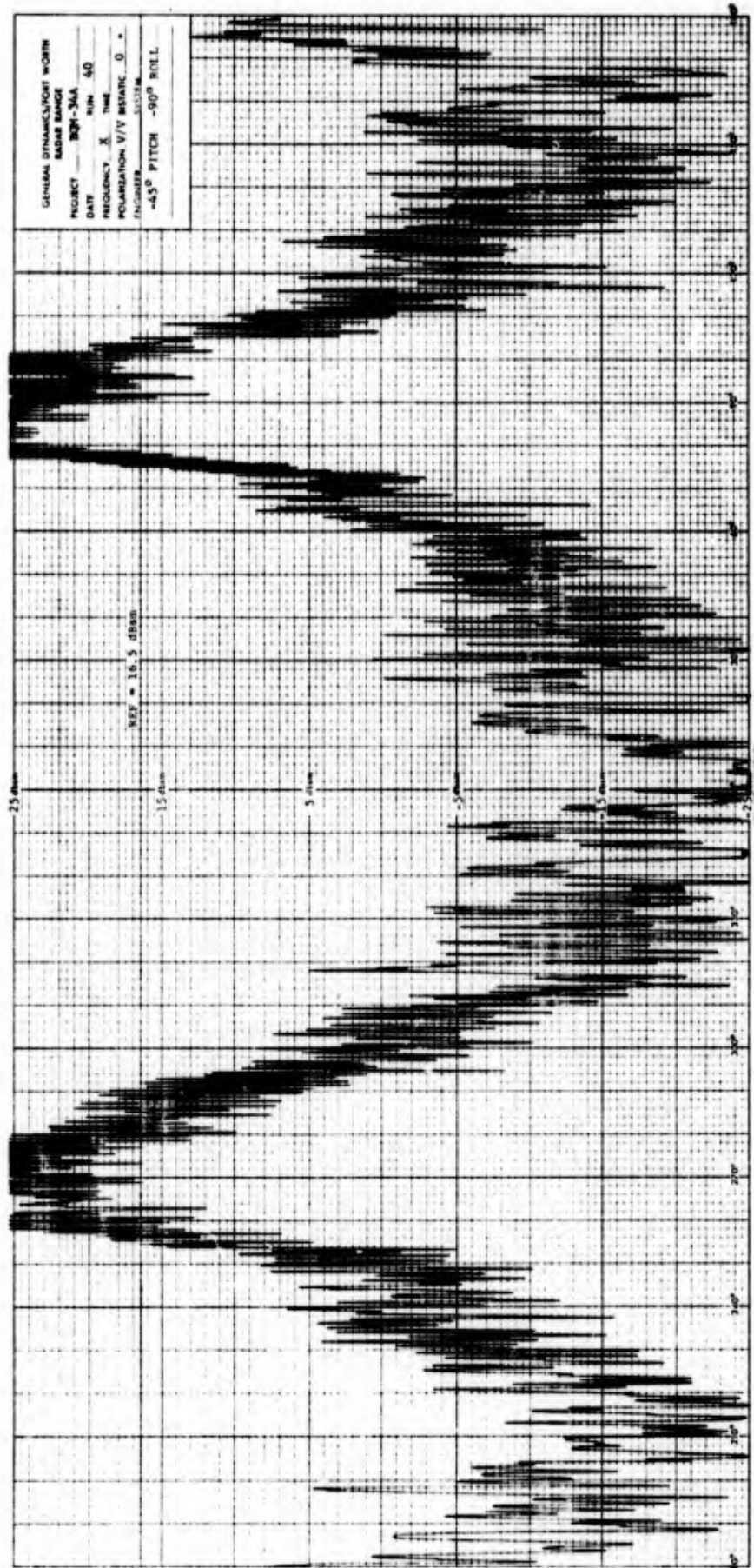


Fig. A-32 X-BAND RCS OF BQM-34A DRONE MODEL  
(V/V POLARIZATION, -45° PITCH, -90° ROLL)

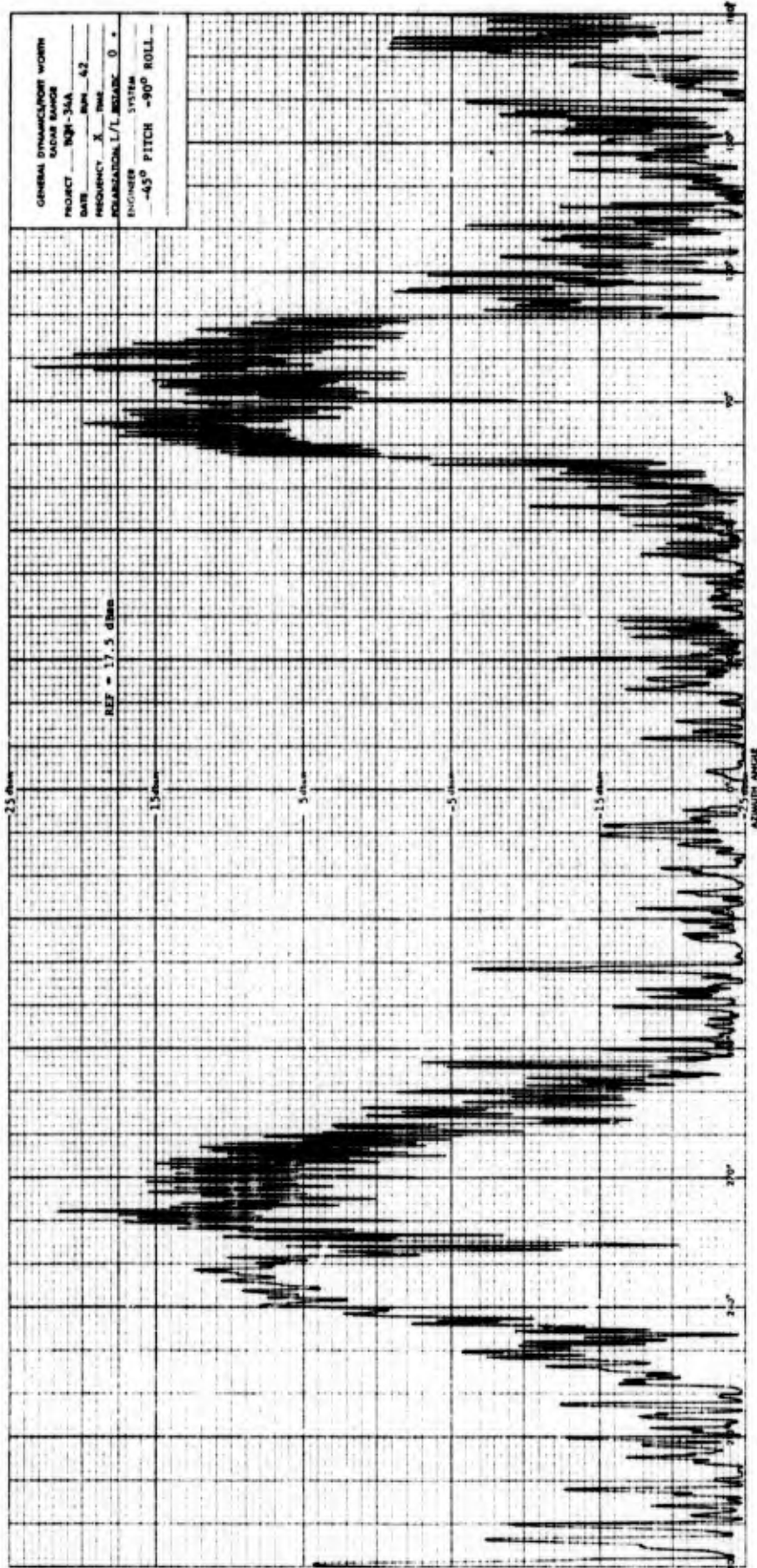


Fig. A-33 X-BAND RCS OF BQM-34A DRONE MODEL  
(L/L POLARIZATION, -45° PITCH, -90° ROLL)

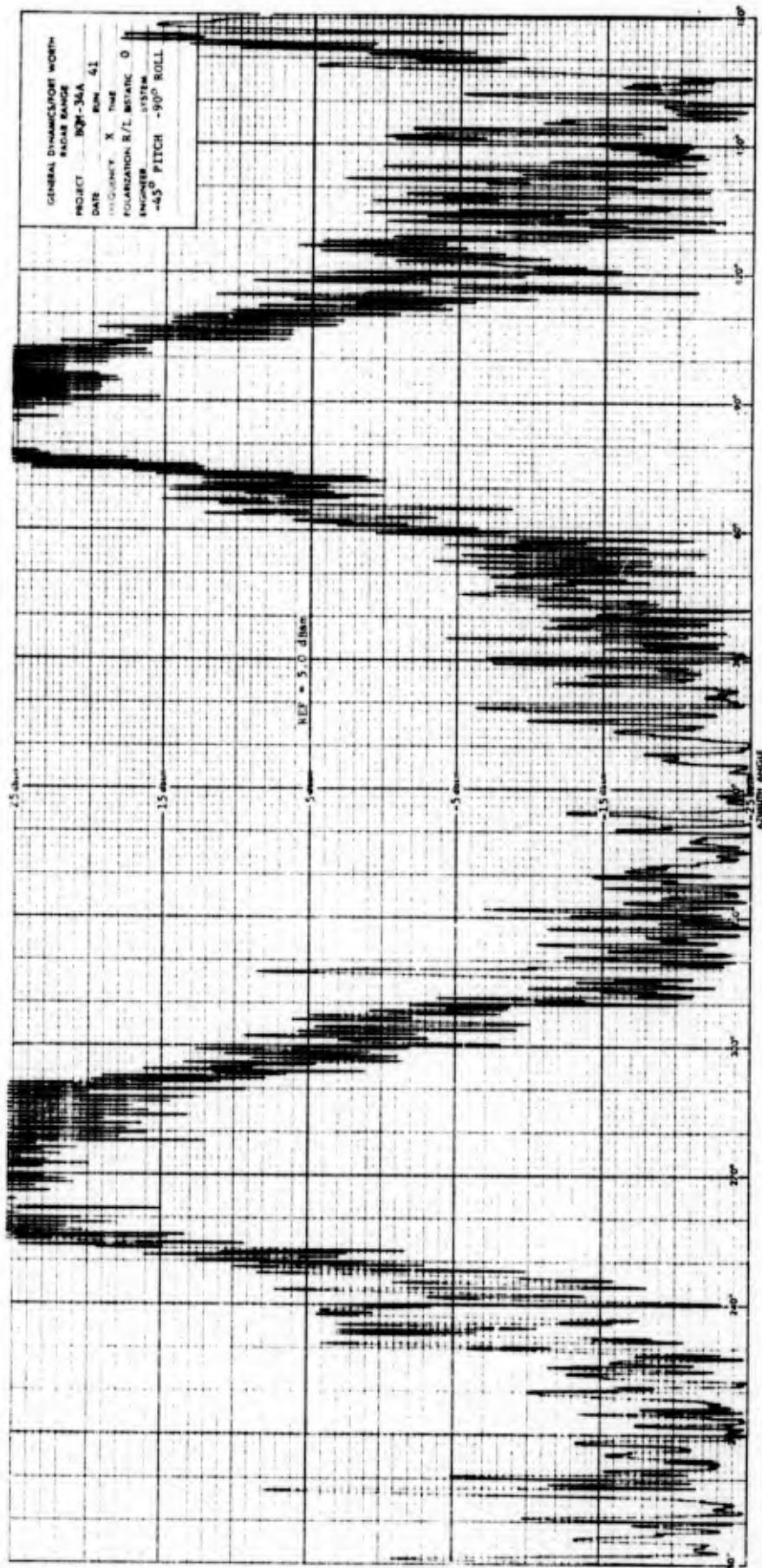


Fig. A-34 X-BAND RCS OF BQM-34A DRONE MODEL  
(R/L POLARIZATION, -45° PITCH, -90° ROLL)

Each of the analog cross section plots contains a heading at the top of the figure that identifies the measurement frequency, polarization, run number, target configuration, and target orientation. The return from the calibrated secondary reference is also shown as a horizontal line on each plot. The cross section values as determined from this reference are also shown on the vertical scale.